

CONTROL OF THE ATMOSPHERIC FLIGHT PHASE OF SMALL ROCKET LAUNCHERS

CONTROL OF THE ATMOSPHERIC FLIGHT PHASE OF SMALL ROCKET LAUNCHERS

by

Miguel DE FREITAS DIAS

to obtain the degree of Master of Science
at the Delft University of Technology,
to be defended publicly on the 11th of April, 2017 at 9:00.

Student number: 4401972

Project duration: February 15, 2016 – April 11, 2017

Thesis committee: Prof. José Fernando Alves da Silva, chairperson
Prof. Rita Maria Mendes de Almeida Correia da Cunha, IST, supervisor,
Dr. Paulo André Nobre Rosa, Deimos Engenharia, supervisor
Prof. Paulo Jorge Coelho Ramalho Oliveira, IST, member of the committee



ACKNOWLEDGEMENTS

Firstly, I take the opportunity to thank to my supervisors, Professor Rita Cunha and Dr. Paulo Rosa, for their invaluable guidance, help, and support since the beginning of this work. All the discussions we had during the project vastly contributed to expanding my knowledge not only in control systems, but also about conducting and documenting research.

To my family, especially my Parents and Sister, who have always been supportive of my projects, be it a year studying abroad, or summer internships in another continent. Your unconditional love, patience and encouragement is cherished and drives me forward. To my Father, who having been through Técnico knew the hardships of the first year and guided me through it. You are a true role model, to whom I look up to, both in Engineering and in Life. To my Mother for always having a kind word and helping me with big decisions. To my Sister who I always miss when she is not around. To my Grandmothers and Aunt, who raised me since I was a child.

I would also like to express my deeply gratitude to my friends and colleagues. To Miguel Santos, for sharing this journey with me since kindergarten, Miguel Mendes, always present and ready to help, Gonçalo Gomes, a true brother in arms, Marta Luís, for the countless dinners and sleepovers, Sofia Ribeiro and Marta Verdugo, who were effectively my family during my year in Delft, João Morna, my fencing buddy, Rita Escudeiro for the support during the difficult months at beginning of the research, João Souto, André Pereira, Eduardo Aguiar and João Paulo Silva for the constant presence. A special thank-you goes to David Cordeiro, who conducted his work at Deimos with me and helped to solve countless bugs on a daily basis.

This work was conducted with the support of Deimos Engenharia, to whom I would like to thank the opportunity and warm welcome at the company. Finally, I would like to thank to all members of the DSOR group for welcoming me in the lab and for always being kind and supportive.

CONTENTS

Acknowledgements	v
Summary	xi
Acronyms, Abbreviations and Definitions	xiii
1 Introduction	1
1.1 Review of launch vehicle GNC techniques	3
1.2 Objectives and Organization of the Dissertation	5
2 Six Degree-of-freedom Nonlinear Dynamical Modelling	7
2.1 The VEGA launch vehicle	7
2.2 Definition of reference frames	9
2.2.1 From Inertial planetocentric to Launch point reference frame	10
2.2.2 From Launch point to body reference frame	11
2.2.3 External forces acting on the body	12
2.3 Launcher equations of motion	14
2.4 Flexible modes	18
3 Trimming and Linearization	19
3.1 Trimming	19
3.2 Linearization	21
4 Linear Control	23
4.1 Analysis of poles of the linearized system	23
4.2 SISO control design	25
4.2.1 Redefinition of the input	26
4.2.2 Longitudinal Control	26
4.2.3 Lateral Control	34
4.2.4 Implementation of the PID controllers in the full linear system	35
4.2.5 Implementation of the PID controllers in the nonlinear model	36
4.2.6 Flexible modes	37
4.3 LQR Control	39
4.3.1 Choice of LQR weights	39
4.3.2 Actuator model	43
4.3.3 Application of the LQR controller to the full trajectory	45
4.3.4 Application of the controller to the nonlinear system	46
4.4 Robustness analysis of the Linear Controller	46
4.4.1 Analysis of the effect of I_{yy} in the performance of the system	47
4.4.2 Analysis of the effect of varying two parameters simultaneously, in the performance of the system	49

5	Nominal nonlinear control design	53
5.1	Overview of nonlinear systems theory	53
5.1.1	Lyapunov analysis	53
5.1.2	Nonlinear backstepping	55
5.2	Application of nonlinear backstepping to the launch vehicle	57
6	Robustness analysis of the nonlinear controller	63
6.1	Robustness to bounded roll-rate disturbances	63
6.2	Robustness to bounded disturbances in the aerodynamic torque	68
6.3	Robustness to disturbances on angular velocity measurement.	69
6.4	Robustness to disturbances on Euler Angle measurement	71
6.5	Robustness to disturbances in the inertia matrix.	71
6.5.1	Disturbances in the diagonal terms of the inertia matrix.	71
6.5.2	Disturbances in the non-diagonal terms of the inertia matrix	73
6.6	Effect of flexible modes	75
6.7	Robustness to perturbations on the position of the center of mass, \mathbf{P}_{CG}	78
6.7.1	Variation of \mathbf{P}_{CG} along the x_B -axis	79
6.7.2	Variation of \mathbf{P}_{CG} along the y_B -axis	79
6.7.3	Variation of \mathbf{P}_{CG} along the z_B -axis	80
6.8	Adaptive backstepping control.	80
7	Comparison of the linear and nonlinear controllers	85
8	Conclusions and future work	91
8.1	Directions for future work	92
	Bibliography	93
	References	93
A	VEGA launcher characteristics	97
B	Rotation Matrices	99
B.1	From ECI to Launch point reference frame	99
C	Implementation of the model	101
D	Evolution of the linearized system's poles with time	105
D.1	From $t=10$ s to $t=20$ s	105
D.2	From $t=20$ s to $t=30$ s	105
D.3	From $t=30$ s to $t=40$ s	106
D.4	From $t=40$ s to $t=50$ s	106
D.5	From $t=50$ s to $t=60$ s	107
E	Effect of varying parameters in LQR controller robustness	109
E.1	Mass	109
E.2	I_{xx}	109
E.3	x_{CG}	109
E.4	x_{CP}	110
E.5	C_a	110

E.6	C_n	110
E.7	S	111
F	Moments acting on the body for a perturbation of P_{CG} along the x_B-axis	113

SUMMARY

This dissertation addresses **Thrust Vector Control (TVC)** design techniques for small launch vehicles with bounded roll rate. The first contribution of this dissertation is the development of a 6 **Degree of Freedom (DoF)** nonlinear model that serves as a tool for flight control system design. The nonlinear model is then trimmed and linearized, for a series of operating points, yielding a set of linear models. Building upon this result, decoupled lateral and longitudinal **PID** controllers are designed, as well as a **Linear Quadratic Regulator (LQR)** controller. The impact of flexible modes on the linear controller is assessed as well as the robustness of the **LQR** controller to parameter variations. Using the nonlinear model a backstepping controller is developed and implemented. Lyapunov stability analysis is used to assess the robustness and performance of this controller to different types of exogenous disturbances and model perturbations. Specific inaccuracies in the position of the center of mass lead to significant performance deterioration. Therefore an estimator is developed. The estimator design is integrated with the controller, thus stability of the overall system is ensured. Finally, a comparison between the performance of the proposed linear and nonlinear controllers is performed. The applicability of the nonlinear controller to other launch vehicles is discussed. **Keywords**

Keywords: 6 Degree of Freedom modelling, Launch Vehicle, LQR, PID, Backstepping, Lyapunov Design

ACRONYMS, ABBREVIATIONS AND DEFINITIONS

AVUM	Attitude and Vernier Upper Module
DoF	Degree of Freedom
ECI	Earth Centered Inertial
ELV	Expendable Launch Vehicle
ESA	European Space Agency
FAA	Federal Aviation Administration
GNC	Guidance, Navigation & Control
GTO	Geostationary Transfer Orbit
IMU	Inertial Measurement Unit
IP	Inertial Planetocentric
IST	Instituto Superior Técnico
LEO	Low Earth Orbit
LFT	Linear Fractional Transformation
LHP	Left Half Plane
LPV	Linear Parameter Varying
LQR	Linear Quadratic Regulator
LTl	Linear Time Invariant
MEO	Medium Earth Orbit
MSc	Masters degree in the area of Science.
NASA	National Aeronautics and Space Administration
NGSO	Non Geosynchronous Orbit
PD	Proportional Derivative

PID Proportional Integral Derivative

PI Proportional Integral

RACS Roll and Attitude Control System

RHP Right Half Plane

RMS Root Mean Square, $\mathbf{X}_{RMS} = \sqrt{\frac{1}{N} \sum_{n=1}^N |X_n|^2}$

SISO Single-Input Single-Output

SLS Space Launch System

TVC Thrust Vector Control

V & V Verification and Validation

VEGA Vettore Europeo di Generazione Avanzata

1

INTRODUCTION

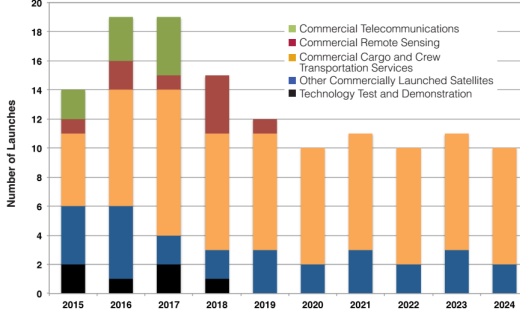
Recent studies show that there has been an increase in the total number of spacecraft launched into space over the past ten years, with potential growth over the next decade [1]. According to [Federal Aviation Administration \(FAA\)](#)'s 2015 commercial space transportation forecasts [2], the average number of [Non Geosynchronous Orbit \(NGSO\)](#) launches for 2014 through 2021 is 13.1 launches per year. [NGSO](#) launches project commercial launch demand for satellites, to [Low Earth Orbit \(LEO\)](#), [Medium Earth Orbit \(MEO\)](#) and [Geostationary Transfer Orbit \(GTO\)](#). Small satellites operating in [Low Earth Orbits](#) have attracted the interest of scientific research entities [3] and private commercial enterprises alike. First and foremost, low-mass platforms have a lower launch cost and a shorter development time [4]. Sandau [5] lists other important reasons for the interest in this type of satellites:

- Enabling frequent mission opportunities, which in turn allows faster return of scientific data;
- Diversification of mission envelopes, attracting more potential users;
- New trends in space systems: use of constellations of satellites flying in formation [6].

In addition the appearance of private companies capable of achieving orbital injection, as well as the increase in the number of space-fairing nations, further reduced launch costs for small satellites. The decrease in launch costs, allied with advances in miniaturization technology and a high need for Space observation missions led to growth in investment and technology in this class of satellites [5].

A major driver in this trend was the introduction of Cubesats. Cubesats are standardised platforms that represent a cost-effective solution for scientific testing and allowing universities and emerging nations to access space [7, 8]. Alongside the Cubesat platform, several other standardised small satellite platforms, such as Minisat, Proteus and PRIMA, are being developed. It is expected that the availability of such platforms will attract several applications, allowing overall cost reductions and new project starts [9]. With the advances of on-board processing capabilities of small satellites, missions that

were only possible with large satellites, have become possible using constellations of smaller satellites at a fraction of the conventional price [10]. Figure 1.1 shows FAA's projected NGSO launches until 2024. The spike in the number of launches in 2016-2018 is due to Iridium, ORBCOMM, Planet Labs, and Skybox, all deploying their small commercial satellites constellations [2]. For 2018-2024, it is expected that the NGSO launches are divided between commercial satellites and commercial launches to the ISS. The global interest in small missions implies the development of low-capacity launch vehicles.



Payload	
Small	0-2 t
Medium	2 - 20 t
Heavy	20 - 50 t
Super Heavy	>50 t

Figure 1.1: Projected NGSO launches until 2024 [2] Table 1.1: Classes of launch vehicles [11]

Small satellites ¹ like Cubesats are usually launched as secondary payload on a larger mission, which has obvious limitations in terms of the launch date and final orbit for the satellite, as the mission is developed for the primary cargo.

Alongside advances in large launch vehicles, there have been efforts to develop smaller launch vehicles, designed to take light payloads to LEO. Again, it is important to classify the types of launch vehicles. Table 1.1 shows National Aeronautics and Space Administration (NASA)'s classification for launch vehicles, based on the payload the vehicle can carry. This work focuses on the small payload class and specifically on rocket launch vehicles. There are several different launch vehicles operating today in this class, some of which are listed in Table 1.2.

From the data presented in Table 1.2, there are several options with different design parameters and mission requirements, manufactured both by government agencies or private companies. Except the Pegasus launcher (which is air-launched), all other listed launch systems are rocket launchers. Evidently, all these launch systems need GNC algorithms to steer its cargo into orbit. The starting point of this work is a study of control systems for the atmospheric flight phase of rocket launchers, using linear and nonlinear control techniques.

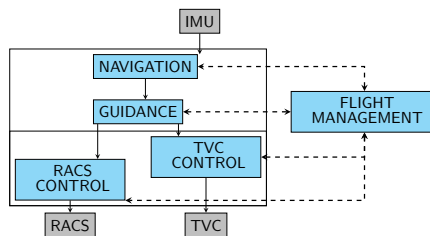
¹Although there are discrepancies in the definitions of small, medium and heavy satellites, Sweetings [12] defines small satellites as those whose mass is smaller than 1000 kg. These definitions vary depending on the orbit. For example, a 4000 kg satellite could be classified as medium for a LEO orbit, but heavy for a Geosynchronous orbit [1].

Vehicle name	Origin	Payload to LEO (Kg)	Last Launch	Successful Launches
VEGA	Europe	1500	2016	8
Pegasus	USA	443	2016	43
Rocket	Russia	1950	2016	27
Epsilon	Japan	700	2016	2
Shavit	Israel	500	2016	8
Minotaur IV	USA	1735	2013	5
Long March 6	China	1000	2015	1
Safir	Iran	50	2015	5

Table 1.2: List of some operational small launch vehicles

1.1. REVIEW OF LAUNCH VEHICLE GNC TECHNIQUES

The **Guidance, Navigation & Control (GNC)** system is of critical importance for a successful mission. Generally, the architecture of the **GNC** system for a launch vehicle can be summarized as in Figure 1.2 [13]. This module uses measurements from the **Inertial Measurement Unit (IMU)** and ultimately produces command signals for the **Roll and Attitude Control System (RACS)** and **Thrust Vector Control (TVC)**.

Figure 1.2: Generic **GNC** architecture, [13]

Intuitively the acronym **GNC** can be explained as follows:

- Guidance - produces position and attitude reference profiles;
- Navigation - determines the vehicle position and attitude with respect to a given reference frames;
- Control - given the reference provided by Guidance and the position from Navigation, computes the appropriate action to steer the launch vehicle, while satisfying a series of constraints.

A robust guidance scheme is essential to increase overall performance, as well as reduce costs and load indicators [14]. Typical ascent guidance schemes for launch vehicles employ two phases: an initial open-loop guidance, followed by a closed-loop segment [14]. The open-loop segment is usually a table of attitude commands, as a function of parameters relevant to the mission (usually time, altitude, or velocity). Depending on the mission, the exact parameters to be optimized may vary, as well as

the algorithm used to optimize said parameters. Open-loop atmospheric guidance has been employed in several launch vehicles, such as the Space Shuttle [15], the European VEGA launcher [13] and is being used in NASA's Space Launch System (SLS) concept studies [16]. The closed-loop guidance segment is usually employed after the occurrence of the maximum dynamic pressure or after the end of the atmospheric flight phase [14]. However, this topic is beyond the scope of the present work. For a treatment of ascent guidance schemes, the reader is referred to [17, 18].

Concerning the control subsystem, a complete and relevant body of work is available in the literature. For the atmospheric ascent phase, linear methods are usually preferred in the design of controllers [16, 19–21], due to years of experience and consolidation of the theory, as well as reliable and well-documented design and analysis procedures. In this phase, control systems are usually gain scheduled controllers, developed using classical linear Proportional Integral Derivative (PID) control, with linear optimal bending filters [13, 16, 20]. During ascent, thrust and aerodynamic properties of the launch vehicle are time-varying. Hence, control laws are usually developed under Verification and Validation (V & V) campaigns to analyse and validate the design [22, 23]. Typical controller synthesis hinges on the "time-slice" method, where the launch vehicle trajectory is divided into time intervals. In each time interval, the vehicle parameters are assumed constant and classical control techniques are used to control the Linear Time Invariant (LTI) model for the given interval. Finally, a global controller is obtained by scheduling/interpolation of local controllers between adjacent time slices [22]. To evaluate the robustness of local controllers, the stability margins for several points of the uncertain parameter space of the launch vehicles is evaluated, by producing several Nichols plots for different parameter combinations (for a given time slice). On the other hand, global controllers are cleared by exhaustive simulation of the transitions between controllers [22]. This is a time-consuming process, which is not scalable, due to the dependence on vehicle and mission specific parameters. The current state-of-the-art in robustness assessment of control law design entail probabilistic Monte Carlo approaches and worst-case scenario analysis (using predefined vertex cases), [24]. Recent work identified modern concepts that can be used to streamline this process [23], such as Linear Fractional Transformation (LFT), μ -analysis and Linear Parameter Varying (LPV) techniques [22, 24–26].

Nonlinear control techniques have also been proposed to control the attitude of launch vehicles [27–31], although typically used in later stages of the mission. These techniques are usually global, meaning that the evaluation of the robustness of the system does not involve as many variables, as is the case with gain-scheduled controllers.

1.2. OBJECTIVES AND ORGANIZATION OF THE DISSERTATION

Having a general view of the current trends in launch vehicles and GNC design, the key objectives of this dissertation can be defined as:

1. Assess the state-of-the-art of GNC design for launchers;
2. Develop a complete control design methodology for small size launchers with uncertain parameters and flexible modes;
3. Propose a systematic nonlinear controller tuning approach to extend the applicability of the methodology to a wide class of launchers;
4. Evaluate the performance in a high-fidelity simulator, compare it to a desired solution, and discuss the trade-off between performance and robustness.

The formulation of the dynamic model for control uses publicly available data related with the *Vettore Europeo di Generazione Avanzata* (VEGA) launcher [13, 24–26, 32–39], deemed to represent a generic small launcher.

In order to achieve the proposed goals, this dissertation is structured in 8 chapters, including this introduction, as follows:

Chapter 2 presents the dynamic model of a generic symmetric rocket launch vehicle, introducing the relevant reference frame and a 6 *Degree of Freedom* (DoF) model for the launcher, including the modelling of flexible modes. Furthermore, a brief description of the VEGA launcher is provided, since this is the reference vehicle considered in this dissertation.

Chapter 3 is devoted to trimming and linearization of the nonlinear model developed in Chapter 2. This is an important step for classical control design and the linear models developed in this chapter will be used to design linear controllers, in Chapter 4.

Chapter 4 is dedicated to linear control. A brief review of the classical control theory is presented at the beginning of the chapter, focusing on the tools used in this dissertation. Furthermore, the linear model developed in Chapter 3 is used to develop two PID controllers for the lateral and longitudinal modes as well as a Linear Quadratic Regulator (LQR) for the angular velocities and Euler angles. Both controllers are implemented in the nonlinear model developed in Chapter 2 and finally the robustness of LQR controller to parameter variation is evaluated.

Chapter 5 is one of the core chapters of this dissertation. An overview of nonlinear control techniques is presented at the beginning of the Chapter, followed by the development of a nonlinear backstepping controller for the nonlinear system (in nominal conditions). This controller enables reference tracking of a trajectory parametrized by Euler angles.

Chapter 6 presents the robustness analysis to parameter variations and several types of disturbances of the controller developed in Chapter 5. This analysis is performed using Lyapunov-based methods. As a consequence of the robustness analysis, it is identified that constant uncertainties in the position of the center of mass lead to significant performance deterioration. Therefore an estimator is developed, resulting in an adaptive backstepping controller.

Chapter 7 compares the linear and nonlinear controllers under several operating conditions, in line with the objectives of this dissertation.

Chapter 8 contains the conclusion, critical remarks and future work to support this dissertation.

2

SIX DEGREE-OF-FREEDOM NONLINEAR DYNAMICAL MODELLING

This chapter is devoted to the study of the system dynamics. Firstly, a general description of the VEGA launcher is presented, as this is the reference vehicle for the modelling developed in this chapter.

Secondly, the relevant reference frames are introduced, as well as the kinematic relationships between them. Then, a 6 Degree of Freedom (DoF) rigid body model is developed. Finally the flexible modes are introduced.

2.1. THE VEGA LAUNCH VEHICLE

VEGA (Vettore Europeo di Generazione Avanzata) is an European small launch vehicle developed for a launch rate up to four launches per year. Its development started as a national Italian concept that was later proposed to the [European Space Agency \(ESA\)](#) as a joint European venture. It is produced by ELV S.p.A. [32].

VEGA is a single-body [Expendable Launch Vehicle \(ELV\)](#) composed of four stages: three solid-propellant stages (P80, Z23 and Z9) and the [Attitude and Vernier Upper Module \(AVUM\)](#), which steers the payload into its final orbit. The AVUM is a liquid propelled module for multiple firing propulsion and thrusters for [RACS](#). [40]

The design mission for [VEGA](#) is bringing a spacecraft of 1500 kg to a polar orbit at an altitude of 700 km. Payload masses range from 300 kg to 2500 kg, depending on the type and altitude of the orbit required by the customers. The [VEGA](#) launcher and a typical mission profile are shown in [Figure 2.1](#).

As referred earlier, this work focuses on the atmospheric flight phase, before the separation of the first stage, comprising approximately the first 100 seconds of the mission. Therefore, it will focus on the characteristics of the first stage. [Appendix A](#) shows [VEGA](#)'s principal characteristics for this stage. Control of the first stage is

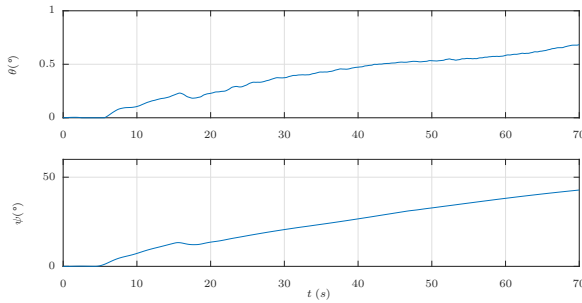


Figure 2.2: Reference VEGA trajectory, defined using the pitch (θ) and yaw (ψ) Euler angles

trajectory is used to evaluate performance, it will be introduced in the pertinent section. It is important to note that the control algorithms should be tested for a wide range of trajectories and injecting the worst-case disturbances on the system, in order to guarantee that the controller is robust.

Launch vehicles are essentially long slender beams. Hence they are structurally very flexible. The IMU is not located at the center of mass of the vehicle (it is located in the AVUM module), therefore it measures the rigid body motion as well as local elastic distortions caused by structural flexibility. These measurements will be fed back to the TVC system, which can excite the structural flexible modes and ultimately generate instability. When considering linear control, the first flexible mode frequency is usually close to the crossover regime of the controller. Hence the control system has the potential to excite the flexible modes and destabilize the system.[44]

Apart from flexible modes, other nonlinear phenomena affect the system, such as aeroelastic flutter or fuel sloshing. However, for the considered phase of the mission, the effect of the flexible modes is predominant. Fuel sloshing is more important when considering the AVUM stage control, as this is the only stage with liquid fuel. In the following sections, the derivation of a 6 DoF dynamical model for a rocket launcher is detailed.

2.2. DEFINITION OF REFERENCE FRAMES

In order to define the complete set of equations of motion, several reference frames are necessary. Figure 2.3 shows the relation between the Earth Centered Inertial (ECI) reference frame, and the launch point reference frame.

In the literature, the x-axis of the ECI reference frame is defined at the intersection of the equatorial plane and the ecliptic plane (pointing towards the Vernal Equinox) [41]. The ECI reference frame is inertial, meaning that it is fixed in space, hence it does not rotate with the Earth. This definition implies that in order to locate a point in ECI coordinates it is necessary to know its latitude, longitude, and the epoch of reference. For simplicity, the Inertial Planetocentric (IP) reference frame will be used as the inertial reference frame. The difference between the ECI and the IP reference frames is that, in the latter, the x-axis is defined by the zero-longitude meridian at zero time (time of the launch) [45]. Hence, only two parameters are needed to describe the location of a

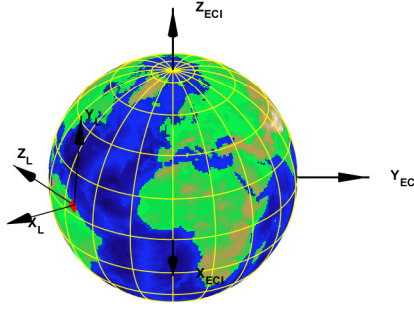


Figure 2.3: ECI and launch site reference frames

point relative to the surface of the Earth.

The launch point reference frame (also shown in Figure 2.3) is characterized as follows: the y_L - z_L plane is tangent to the surface of the Earth at the launch point, with y_L pointing towards the north and z_L pointing towards west. The x_L axis is perpendicular to the y_L and z_L axis and points towards the sky.

A body-fixed reference frame is also defined for the derivation of the equations of motion. The origin of the body-fixed reference frame is the center of mass of the launcher, with the x_B axis aligned along the longitudinal axis of the spacecraft. The body fixed reference frame is aligned with the launch reference frame at the time of the launch. The launch point is the European Spaceport, located at Kourou, in the French Guiana. The coordinates of the launch site are $\delta = 5^\circ 12' 03''$ N, $\tau = 52^\circ 45' 59''$ W (respectively for latitude and longitude) [32].

2.2.1. FROM INERTIAL PLANETOCENTRIC TO LAUNCH POINT REFERENCE FRAME

The transformation between the IP and the launch point reference frame is fully determined by the location of the launch point and the rotation matrix between the two reference frames.

The location of the launch point in IP coordinates is a function of the latitude (δ) and longitude (τ) of the point and radius of the Earth (R_T). For convenience of notation, the index associated with the IP reference frame is simply I instead of IP .

In IP coordinates, the location of the launch point is given by Eq. (2.1) .

$${}^{IP}\mathbf{P}_L = {}^I\mathbf{P}_L = \begin{cases} {}^I x_L = R_T \cos \delta \cos \tau = 3.9005 \times 10^6 \text{ m} \\ {}^I y_L = R_T \cos \delta \sin \tau = -5.0064 \times 10^6 \text{ m} \\ {}^I z_L = R_T \sin \delta = 5.5789 \times 10^5 \text{ m} \end{cases} \quad (2.1)$$

The rotation matrix between the two reference frames is given by Eq. (2.2).

$${}^I\mathbf{R} = \begin{bmatrix} \cos \delta \cos \tau & \cos \delta \sin \tau & \sin \delta \\ -\sin \delta \cos \tau & -\sin \delta \sin \tau & \cos \delta \\ \sin \tau & \cos \tau & 0 \end{bmatrix} \quad (2.2)$$

The derivation of this rotation matrix is carried out in Appendix B.1.

Given that the launch point is fixed on the surface of the Earth, it will move in time with respect to the **IP** reference frame, with a constant angular velocity. To express the position of the body with respect to the **IP** frame, it is necessary to take this into consideration. The position of the body can be written as the vectorial sum of the position of the body with respect to the launch point and the position of the launch point with respect to the **IP** frame, i.e. : ${}^I\mathbf{P}_B = {}^I\mathbf{P}_L + {}^I\mathbf{R}^L\mathbf{P}_B$.

The position of the launch point is constant in the launch reference frame: ${}^L\mathbf{P}_L = [R_T \ 0 \ 0]^T$. The coordinates of the launch point in the **IP** reference frame can also be expressed as a rotation of the position of this point from the launch reference frame to the **IP** frame: ${}^I\mathbf{P}_L(t) = {}^I\mathbf{R}(t){}^L\mathbf{P}_L(t)$. This rotation matrix is time-dependent, due to the constant angular velocity of the Earth.

To find the expression for this time-varying rotation matrix, one can decompose it into two parts: a constant part concerning the initial position of the launch point, and a time dependent part, due to the rotation of the Earth:

$${}^I\mathbf{R}(t) = \mathbf{R}(t) \cdot {}^I\mathbf{R}(t=0) \quad (2.3)$$

The constant part is simply the matrix described in eq. (2.2), depending on the latitude and longitude of the launch point in **IP** coordinates.

To find the time-varying part, consider the rotation of a generic point A, lying in the Equator, along the x-axis of **IP** reference frame. The coordinates of this point are ${}^I\mathbf{P}_A(0) = [R_T \ 0 \ 0]^T$. After a certain time interval, Δt , point A will move to ${}^I\mathbf{P}_A(t) = [R_T \cos(\Delta\theta) \ R_T \sin(\Delta\theta) \ 0]^T$, relative to the **IP** frame. In the previous expression, $\Delta\theta = \Omega_e \Delta t$ and $\Omega_e = 7.291 \times 10^{-5} \text{ rad/s}$ is the angular velocity of the Earth.

This change in position can be encoded into a rotation matrix depending on the constant angular velocity and time after launch:

$$\mathbf{R}(t) = \begin{bmatrix} \cos\Omega_e t & -\sin\Omega_e t & 0 \\ \sin\Omega_e t & \cos\Omega_e t & 0 \\ 0 & 0 & 1 \end{bmatrix} \quad (2.4)$$

Joining equations (2.2), (2.3), and (2.4), it is possible to define the time-varying position of the launch point with respect to the **IP** reference frame.

2.2.2. FROM LAUNCH POINT TO BODY REFERENCE FRAME

The transformation between the launch reference frame and the body-fixed reference frame is expressed through three consecutive rotations, defined by the Euler angle sequence commonly used in aeronautics. The sequence of rotation is: $\mathbf{R}_1(\phi) \leftarrow \mathbf{R}_2(\theta) \leftarrow \mathbf{R}_3(\psi)$. For an in-depth coverage of Euler angles, the reader is referred to [42] and [46]. This transformation is important to express the components of the gravity vector in the body-fixed reference frame and perform conversions between both reference frames. The rotation matrix that transforms a vector in the launch reference frame into its expression in the body-fixed reference frame is given by (2.5). Given the choice of having both reference frames aligned at the time of launch, the Euler angles have the conventional interpretation in terms of roll, pitch, and yaw and will be used to command the attitude of the launch vehicle.

$${}^B_L \mathbf{R} = \begin{bmatrix} c\theta c\psi & c\theta s\psi & -s\theta \\ s\phi s\theta c\psi - c\phi s\psi & s\phi s\theta s\psi + c\phi c\psi & s\phi c\theta \\ c\phi s\theta c\psi + s\phi s\psi & c\phi s\theta s\psi - s\phi c\psi & c\phi c\theta \end{bmatrix} \quad (2.5)$$

To implement the simulation of the equations of motion it is also necessary to know the kinematics of the Euler angles, and its relation with other states of the vehicle, specifically with its angular velocity.

The set of Euler angles is denoted by $\boldsymbol{\lambda}$ and its derivative, $\dot{\boldsymbol{\lambda}}$, is of the form $\dot{\boldsymbol{\lambda}} = f(\phi, \theta, \psi) \cdot {}^B \boldsymbol{\omega}_B$. The expression for these derivatives are readily available in the literature ([41], [42] or [45]):

$$\dot{\boldsymbol{\lambda}} = \begin{cases} \dot{\phi} = p + \sin\phi \tan\theta \cdot q + \cos\phi \tan\theta \cdot r \\ \dot{\theta} = \cos\phi \cdot q - \sin\phi \cdot r \\ \dot{\psi} = \frac{\sin\phi}{\cos\theta} \cdot q + \frac{\cos\phi}{\cos\theta} \cdot r \end{cases} \quad (2.6)$$

In matrix form, the previous equations become:

$$\dot{\boldsymbol{\lambda}} = \begin{bmatrix} \dot{\phi} \\ \dot{\theta} \\ \dot{\psi} \end{bmatrix} = \frac{1}{\cos\theta} \begin{bmatrix} \cos\theta & \sin\phi \sin\theta & \cos\phi \sin\theta \\ 0 & \cos\phi \cos\theta & -\sin\phi \cos\theta \\ 0 & \sin\phi & \cos\phi \end{bmatrix} \cdot \begin{bmatrix} p \\ q \\ r \end{bmatrix} \quad (2.7)$$

2.2.3. EXTERNAL FORCES ACTING ON THE BODY

The external forces acting on the vehicle are gravity, propulsion, and aerodynamic forces (lift and drag). In order to obtain the equations of motion, it is necessary to write these forces in the body-fixed reference frame.

The propulsion system can be swivelled around the pivot point in two different directions, generating pitch and yaw moments to control the trajectory. Hence, the transformation of the thrust force from the TVC reference frame to body axis needs to be defined. To do so, consider that the thrust vector lies along the x_B -axis. A negative rotation around the y_B -axis is performed, generating a pitching moment. The angle of rotation is δ_p . Next, perform a negative rotation around the z-axis, generating a yaw moment. The angle associated with this second rotation is δ_y . The rotation matrix from the body reference to the TVC reference frame is given by the multiplication of the two elementary rotations defined earlier, in the sequence $\mathbf{R}_1(-\delta_p) \leftarrow \mathbf{R}_2(-\delta_y)$, yielding

$${}^T_B \mathbf{R} = \begin{bmatrix} \cos\delta_y \cos\delta_p & -\sin\delta_y & -\cos\delta_y \sin\delta_p \\ \sin\delta_y \cos\delta_p & \cos\delta_y & -\sin\delta_y \sin\delta_p \\ \sin\delta_p & 0 & \cos\delta_p \end{bmatrix} \quad (2.8)$$

In rocket launchers, it is common to have the TVC system rotated from the principal axis of the vehicle. Therefore, a rotation of $\Delta\alpha = -45^\circ$ around the x_B -axis is applied, resulting in the following transformation matrix from the body to the thrust axis:

$${}^T_B \mathbf{R} = \mathbf{R}_x(-45^\circ) \cdot {}^T_B \mathbf{R} = \begin{bmatrix} c\delta_p c\delta_y & s\delta_y c\delta_p & s\delta_p \\ \frac{\sqrt{2}}{2} (s\delta_y + c\delta_y s\delta_p) & \frac{\sqrt{2}}{2} (s\delta_y s\delta_p - c\delta_y) & -\frac{\sqrt{2}}{2} c\delta_p \\ \frac{\sqrt{2}}{2} (c\delta_y s\delta_p - s\delta_y) & \frac{\sqrt{2}}{2} (s\delta_y s\delta_p + c\delta_y) & -\frac{\sqrt{2}}{2} c\delta_p \end{bmatrix} \quad (2.9)$$

Therefore, the thrust, when expressed in the body frame is given by ${}^B\mathbf{T} = {}^B_I\mathbf{R} \cdot [T \ 0 \ 0]^T$.

The magnitude of the thrust vector vs. time is modelled according to the profile presented in [25], [39], and shown in Figure 2.4.

Next, the aerodynamic forces need to be written in the body frame. The aerodynamic forces expressed in the aerodynamic reference frame are ${}^A\mathbf{F}_a = [-D \ L \ 0]$. This frame is related to the body-fixed frame by the two aerodynamic angles: the angle of attack, α , and the sideslip angle, β .

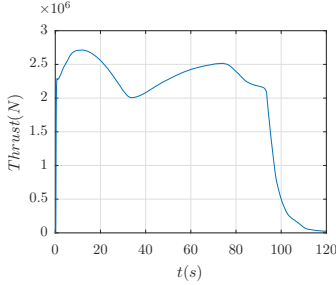


Figure 2.4: Thrust profile

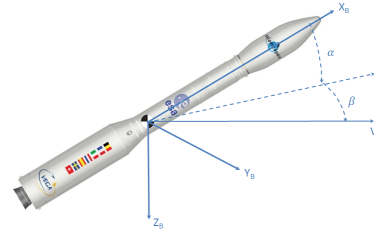


Figure 2.5: Aerodynamic reference frame [45]

To get to the aerodynamic reference frame, starting in the body-fixed reference frame, one has to perform a positive rotation, α , around the y_B -axis, followed by a rotation β around the z -axis. As before, the rotation matrix is given by the multiplication of the two basic rotations, in the sequence $\mathbf{R}_1(\alpha) \leftarrow \mathbf{R}_2(\beta)$, yielding

$${}^A_B\mathbf{R} = \begin{bmatrix} \cos \beta \cos \alpha & \sin \beta & \cos \beta \sin \alpha \\ -\sin \beta \cos \alpha & \cos \beta & -\sin \beta \sin \alpha \\ -\sin \alpha & 0 & \cos \alpha \end{bmatrix} \quad (2.10)$$

Hence, the aerodynamic forces in the body-fixed reference frame are given by ${}^B\mathbf{F}_a = {}^B_A\mathbf{R}[-D \ L \ 0]^T$. The aerodynamic drag and lift are modelled as $D = \frac{1}{2}\rho S V^2 C_a$ and $L = \frac{1}{2}\rho S V^2 C_n \alpha$, where C_a and C_n are, respectively, the axial and normal aerodynamic coefficients and α is the angle of attack. The modelling of these coefficients is described in section 2.2.3.

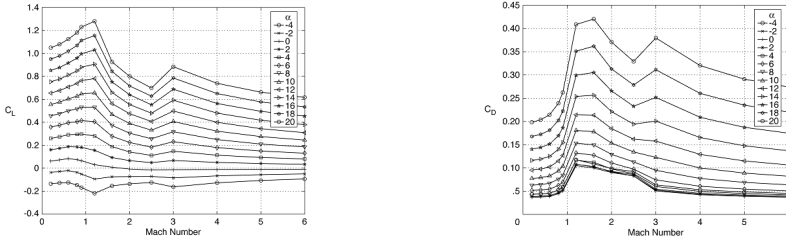
Finally, the gravity force expressed in the body axis is written as ${}^B\mathbf{F}_g = {}^B_I\mathbf{R}[-mg \ 0 \ 0]^T$, with ${}^B_I\mathbf{R} = {}^I_B\mathbf{R}^T$ being the rotation matrix identified in (2.5).

MODELLING OF THE NORMAL AND AXIAL AERODYNAMIC COEFFICIENTS

The model of the aerodynamic coefficients was derived from the work in [47], where the variation of the aerodynamic coefficients for a multi-stage vehicle with a space-shuttle like geometry is shown. The plots are reproduced here for clarity, in Figure 2.6.

The aerodynamic coefficients are a function of the angle of attack, α , and Mach number, M .

For small angles, the main contribution for the normal aerodynamic coefficient comes from the angle of attack. This can be seen in Figure 2.6a, as the characteristics of the curve stay roughly the same with the evolution of the Mach number. Hence, $C_n(\alpha, M) \approx f(\alpha)$. The variation of the normal coefficient with the angle of attack was interpolated



(a) Normal aerodynamic coefficient, $C_n = f(\alpha, M)$ (b) Axial aerodynamic coefficient, $C_a = f(\alpha, M)$

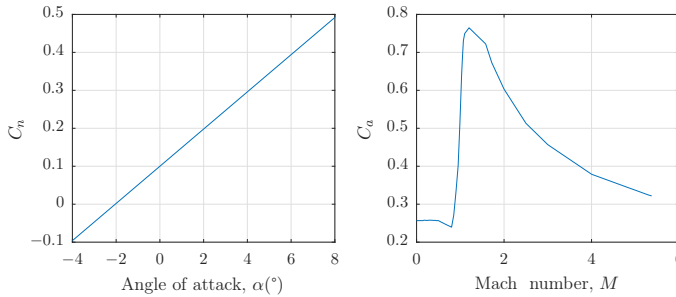
Figure 2.6: Aerodynamic coefficients for a multi-stage vehicle with a space-shuttle like geometry [47]

using data from the plot (in the range -4° to 8°), resulting in a variation $\Delta C_n = 0.0049/^\circ$. Finally, based on the data presented in Fig. 2.6a, the model of the normal aerodynamic coefficient is then defined as

$$C_n = 0.1 + \Delta C_n \cdot \alpha, \alpha \in [-4, 8]^\circ \quad (2.11)$$

The implemented model of the normal coefficient with the angle of attack is shown in Figure 2.7a .

Regarding the axial aerodynamic coefficient, for the small angle of attack region considered ($\alpha \in [-4, 8]^\circ$), it can be seen in figure 2.6b that in this region the main contribution for the variation of the axial aerodynamic coefficient is due to the variation of the Mach number: $C_a(\alpha, M) \approx f(M)$. Interpolating in this region, around $\alpha = 0$, results in the model shown in Figure 2.7b.



(a) Model of the normal aerodynamic coefficient, C_n (b) Model of the axial aerodynamic coefficient, C_a

Figure 2.7: Model of the aerodynamic coefficients implemented in the simulation

2.3. LAUNCHER EQUATIONS OF MOTION

To write the equations of motion of the launcher, a suitable inertial reference frame needs to be selected. Two choices are possible: either the **IP** reference frame or the launch point reference frame. The launch point reference frame moves with zero acceleration (but with velocity of constant magnitude) with respect to the **IP** reference frame. This

work aims to study the ascent phase of the launcher, comprising approximately the initial 120 seconds after launch. Over the course of the initial 120 s, the angular displacement of the origin of launch reference frame is approximately $\Delta\theta = \Omega_e \cdot \Delta t \approx 0.5^\circ$. Hence, given the time scale of the problem, the centripetal acceleration due to the angular velocity of the Earth is negligible and the launch point reference frame can be considered *quasi*-inertial for this application. Using the launch point reference frame as the inertial frame of reference has advantages in the description of the problem: the x-axis directly describes the altitude of the vehicle and the velocity relative to the surface is readily available (if wind is null). To express the position of the vehicle in IP coordinates, once simply has to use the transformation described in subsection 2.2.1. With the forces identified in the previous section and the definition of the inertial frame of reference, Newton's second law yields:

$$\dot{m}^L \mathbf{v} + m^L \dot{\mathbf{v}} = {}^L_B \mathbf{R} ({}^B \mathbf{T} + {}^B \mathbf{F}_A + {}^B \mathbf{F}_g) \quad (2.12)$$

The inertial velocity is defined as ${}^L \mathbf{v} = {}^L_B \mathbf{R} {}^B \mathbf{v}$. Differentiating:

$${}^L \dot{\mathbf{v}} = {}^L_B \dot{\mathbf{R}} {}^B \mathbf{v} + {}^L_B \mathbf{R} {}^B \dot{\mathbf{v}} = {}^L_B \mathbf{R} (\mathbf{S}(\boldsymbol{\omega}) {}^B \mathbf{v} + {}^B \dot{\mathbf{v}}), \quad (2.13)$$

where $\mathbf{S}(\boldsymbol{\omega})$ is a skew-symmetric matrix of the form

$$\mathbf{S}(\boldsymbol{\omega}) = \begin{bmatrix} 0 & -\omega_3 & \omega_2 \\ \omega_3 & 0 & -\omega_1 \\ -\omega_2 & \omega_1 & 0 \end{bmatrix}, \quad (2.14)$$

and ${}^B \mathbf{v} = [u \ v \ w]^T$ represents the velocity vector, expressed in the body-fixed reference frame. Hence, joining Eqs. (2.12) and (2.13),

$$\dot{m}^L {}^B \mathbf{R} {}^B \mathbf{v} + m^L {}^B \mathbf{R} (\mathbf{S}(\boldsymbol{\omega}) {}^B \mathbf{v} + {}^B \dot{\mathbf{v}}) = \underbrace{{}^B \mathbf{R} {}^L_B \mathbf{R}}_I ({}^B \mathbf{T} + {}^B \mathbf{F}_A + {}^B \mathbf{F}_g - \dot{m}^B \mathbf{v}). \quad (2.15)$$

Finally, the expression for the linear acceleration in the body axis is:

$${}^B \dot{\mathbf{v}} = \frac{1}{m} ({}^B \mathbf{T} + {}^B \mathbf{F}_A + {}^B \mathbf{F}_g) - \mathbf{S}(\boldsymbol{\omega}) {}^B \mathbf{v} - \frac{\dot{m}}{m} {}^B \mathbf{v}. \quad (2.16)$$

For rocket launchers, $\frac{\dot{m}}{m} \ll 1$ so the last term is dominated by the other two and it can be disregarded in Eq. 2.16. Separating Eq (2.16) into scalar components with this assumption yields

$$\begin{bmatrix} \dot{u} + qw - rv \\ \dot{v} + ru - pw \\ \dot{w} + pv - qu \end{bmatrix} = \frac{1}{m} \begin{bmatrix} Tc\delta_y c\delta_p - (Dc\beta c\alpha + Ls\beta c\alpha) - mgc\theta c\psi \\ \frac{T\sqrt{2}}{2} (s\delta_y + c\delta_y s\delta_p) + (Lc\beta - Ds\beta) - mg (s\phi s\theta c\psi - c\phi s\psi) \\ \frac{T\sqrt{2}}{2} (c\delta_y s\delta_p - s\delta_y) - (Ls\beta s\alpha + Dc\beta s\alpha) - mg (c\phi s\theta c\psi + s\phi s\psi) \end{bmatrix}, \quad (2.17)$$

where $\cos \alpha = c\alpha$ and $\sin \alpha = s\alpha$ are used for all angles. Solving w.r.t. the linear acceleration,

$$\begin{cases} \dot{u} = \frac{Tc\delta_y c\delta_p - (Dc\beta\alpha + Ls\beta\alpha)}{m} - g\theta c\psi + rv - qw \\ \dot{v} = \frac{T\sqrt{2}(s\delta_y + c\delta_y s\delta_p) + (Lc\beta - Ds\beta)}{m} - g(s\phi s\theta c\psi - c\phi s\psi) + pw - ru \\ \dot{w} = \frac{T\sqrt{2}(c\delta_y s\delta_p - s\delta_y) - (Ls\beta\alpha + Dc\beta\alpha)}{m} - g(c\phi s\theta c\psi + s\phi s\psi) + qu - pv \end{cases} \quad (2.18)$$

For rotational motion, the general equation for an arbitrary flexible body with variable mass is [41]:

$$M_{CM} = \int_m \mathbf{r} \times \left(\frac{d\boldsymbol{\omega}}{dt} \times \mathbf{r} \right) dm + \int_m \mathbf{r} \times [\boldsymbol{\omega} \times (\boldsymbol{\omega} \times \mathbf{r})] dm + 2 \int_m \mathbf{r} \times \left(\boldsymbol{\omega} \times \frac{\delta \mathbf{r}}{\delta t} \right) dm + \int_m \mathbf{r} \times \frac{\delta^2 \mathbf{r}}{\delta t^2} dm, \quad (2.19)$$

where \mathbf{M}_{CM} represents the sum of external moments around the center of mass, \mathbf{r} the position of a mass element with respect to the center of mass of the body and $\boldsymbol{\omega}$ the angular velocity of the body w.r.t the inertial frame. It is possible to modify Eq. (2.19) and explicit the terms of the flexibility of the vehicle and the terms if the vehicle was rigid:

$$\mathbf{M}_{CM} = \mathbf{I}\dot{\boldsymbol{\omega}} + \boldsymbol{\omega} \times \mathbf{I} + 2 \int_m \mathbf{r} \times \left(\boldsymbol{\omega} \times \frac{\delta \mathbf{r}}{\delta t} \right) dm + \int_m \mathbf{r} \times \frac{\delta^2 \mathbf{r}}{\delta t^2} dm. \quad (2.20)$$

The two last terms of Eq. (2.20) are a consequence of the fact that the center of mass of the vehicle varies in time. The two first terms represent Euler's equation for rigid body rotation. As explained earlier, the model of this vehicle is based on the VEGA launcher. The variation of the position of the center of mass for this vehicle is given in [25], where it is shown that it varies linearly. Therefore, $\frac{\delta^2 \mathbf{r}}{\delta t^2} = 0$, so the last term of Eq. (2.20) is zero. Furthermore, the variation of the position of the center of mass is slow ($\Delta \mathbf{X}_{CG} \approx 0.0447$ m/s), for the considered time scale, hence the term depending on $\frac{\delta \mathbf{r}}{\delta t}$ can be discarded. Hence, Euler's equation for rigid body rotation can be applied. The only forces that generate moments on the launcher are the thrust and aerodynamic forces. Given that gravity acts in the center of mass, it does not generate torque. The total moment acting on the body is given by

$$\begin{aligned} \sum \mathbf{M}_{CM} &= \begin{bmatrix} l_{GA} \\ 0 \\ 0 \end{bmatrix} \times {}^B_A \mathbf{R} \begin{bmatrix} -D \\ L \\ 0 \end{bmatrix} + \begin{bmatrix} -l_{CG} \\ 0 \\ 0 \end{bmatrix} \times {}^B_T \mathbf{R} \begin{bmatrix} T \\ 0 \\ 0 \end{bmatrix} \\ &= \begin{bmatrix} 0 \\ \frac{\sqrt{2}}{2} T l_{CG} (c\delta_y s\delta_p - s\delta_y) + (Dc\beta\alpha + Ls\beta\alpha) l_{GA} \\ -\frac{\sqrt{2}}{2} T l_{CG} (c\delta_y s\delta_p + s\delta_y) + (Lc\beta - Ds\beta) l_{GA} \end{bmatrix}, \end{aligned} \quad (2.21)$$

where $\mathbf{l}_{GA} = (\mathbf{X}_{CP} - \mathbf{X}_g)$ represents the lever arm between the center of pressure and the center of gravity and $\mathbf{l}_{CG} = (\mathbf{X}_g - \mathbf{X}_{PVP_T})$ represent the lever arm between the center of gravity and the pivot point of the thrust vector. Noting that the body-axes are principal

¹This equation can be obtained through algebraic manipulation of Eq. (2.19) and using $I = \int_m -S(\mathbf{r})^2 dm$

axes of inertia and that the launch vehicle is symmetric, then $I_{xy} = I_{xz} = 0$ and the inertia tensor is simply given by

$$\mathbf{I} = \begin{bmatrix} I_{xx} & 0 & 0 \\ 0 & I_{yy} & 0 \\ 0 & 0 & I_{zz} \end{bmatrix}. \quad (2.22)$$

Furthermore, due to the geometry of the launch vehicle, it is known that $I_{yy} = I_{zz} \gg I_{xx}$. Substituting Eqs. (2.21) and (2.22) in Eq. (2.20) yields:

$$\begin{cases} I_{xx}\dot{p} + qr(I_{zz} - I_{yy}) = 0 \\ I_{yy}\dot{q} + pr(I_{xx} - I_{zz}) = \frac{\sqrt{2}}{2}Tl_{CG}(c\delta_y s\delta_p - s\delta_y)l_{CG} + (Dc\beta s\alpha + Ls\beta s\alpha)l_{GA} \\ I_{zz}\dot{r} + pq(I_{xx} - I_{yy}) = -\frac{\sqrt{2}}{2}Tl_{CG}(c\delta_y s\delta_p + s\delta_y)l_{CG} + (Lc\beta - Ds\beta)l_{GA}. \end{cases} \quad (2.23)$$

Solving to the angular acceleration, leads to:

$$\begin{cases} \dot{p} = 0 \\ \dot{q} = \frac{\frac{\sqrt{2}}{2}Tl_{CG}(c\delta_y s\delta_p - s\delta_y)l_{CG} + (Dc\beta s\alpha + Ls\beta s\alpha)l_{GA}}{I_{yy}} - \frac{I_{xx} - I_{zz}}{I_{yy}}pr \\ \dot{r} = -\frac{\frac{\sqrt{2}}{2}Tl_{CG}(c\delta_y s\delta_p + s\delta_y)l_{CG} + (Lc\beta - Ds\beta)l_{GA}}{I_{zz}} - \frac{I_{xx} - I_{yy}}{I_{zz}}pq. \end{cases} \quad (2.24)$$

From Eq. (2.24), it is clear that the pitch and yaw dynamics are coupled in the presence of p , as discussed earlier. Finally, the full nonlinear set of equations that define the translational and rotational dynamics, in the body-fixed reference frame, is given by:

$$\begin{cases} \dot{u} = \frac{Tc\delta_y c\delta_p - (Dc\beta c\alpha + Ls\beta c\alpha)}{m} - g\cos\theta\cos\psi + rv - qw \\ \dot{v} = \frac{\frac{T\sqrt{2}}{2}(s\delta_y + c\delta_y s\delta_p) + (Lc\beta - Ds\beta)}{m} - g(s\phi s\theta\cos\psi - c\phi s\psi) + pw - ru \\ \dot{w} = \frac{\frac{T\sqrt{2}}{2}(c\delta_y s\delta_p - s\delta_y) - (Ls\beta s\alpha + Dc\beta s\alpha)}{m} - g(c\phi s\theta\cos\psi + s\phi s\psi) + qu - pv \\ \dot{p} = 0 \\ \dot{q} = \frac{\frac{\sqrt{2}}{2}Tl_{CG}(c\delta_y s\delta_p - s\delta_y)l_{CG} + (Dc\beta s\alpha + Ls\beta s\alpha)l_{GA}}{I_{yy}} - \frac{I_{xx} - I_{zz}}{I_{yy}}pr \\ \dot{r} = -\frac{\frac{\sqrt{2}}{2}Tl_{CG}(c\delta_y s\delta_p + s\delta_y)l_{CG} + (Lc\beta - Ds\beta)l_{GA}}{I_{zz}} - \frac{I_{xx} - I_{yy}}{I_{zz}}pq. \end{cases} \quad (2.25)$$

Given that the mass is time-varying and its value impacts the other states at each time, its dynamics must be considered. The initial mass of the system is $m(0) = 137820$ kg. The propellant mass for the first stage is $M_{prop} = 88383$ kg [32]. The mass flow rate is constant and only due to the exhausted propellant. Hence $\dot{m} \approx \text{constant}$. The separation of the first stage of the vehicle occurs approximately 100 s after launch, so $\dot{m} \approx \frac{m_{prop}}{t_{sep}} \approx 900$ kg/s. Hence, the differential equation that regulates the exhaustion of mass with time is given by $\dot{m} = -900$, $m(0) = 137820$ kg. The assumption that $\frac{\dot{m}}{m} \ll 1$ can now be quantified:

$$\begin{cases} \frac{\dot{m}}{m_0} = \frac{900}{137820} = 0.0065 \text{ s}^{-1} \\ \frac{\dot{m}}{m_f} = \frac{900}{49437} = 0.0182 \text{ s}^{-1} \end{cases} \quad (2.26)$$

From Eq. 2.26 it can be seen that the ratio is indeed small, so the assumption is valid.

2.4. FLEXIBLE MODES

As discussed in 2.1, the flexible modes are very important for the design of the control system of a launch vehicle. Up to this point, the vehicle was considered to be a rigid body, while in fact it is elastic. Modelling the flexible modes is important for control design, because the controller can excite the natural frequencies of the flexible modes, which can lead to instabilities of the closed loop system.

The most straightforward way to include the contribution of the flexible modes in the model is to assume that, due to bending, extra force and moment are generated. It is also assumed that the lateral vibrations along the y_B -axis are the most important ones. These vibrations are caused by the component of the thrust force acting on the y_B -axis. Therefore, the additional force caused by the flexible modes shall be applied in this axis, while the additional moment appears in the z_B -axis. Flexible modes can be described by:

$$\left\{ \begin{array}{l} \ddot{q}_i = -\omega_i^2 q_i - 2\xi\omega_i \dot{q}_i - T_y t_{pi} \\ F_{\text{flex}_y} = T_y \cdot \sum_{i=1}^N r_{pi} q_i \quad , i = 1, 2 \\ M_{\text{flex}_z} = T_y \cdot \sum_{i=1}^N (r_{pi} \cdot l_{CG} + t_{pi}) q_i \quad , \\ \mathbf{F}_{\text{flex}} = \begin{bmatrix} 0 & F_{\text{flex}_y} & 0 \end{bmatrix}^T \\ \mathbf{M}_{\text{flex}} = \begin{bmatrix} 0 & 0 & M_{\text{flex}_z} \end{bmatrix}^T . \end{array} \right. \quad (2.27)$$

Details about the computational implementation of the model described in this chapter can be found in Appendix C.

3

TRIMMING AND LINEARIZATION

Linear control is employed to define a benchmark using very well established linear control and design analysis tools. This benchmark can then be used to assess the performance of the nonlinear controller proposed in chapter 5. Linear control methods require trimming and linearizing the nonlinear set of equations obtained in the previous chapter. Hence, the objective of the present chapter is to provide the necessary linear models to proceed with linear control design.

3.1. TRIMMING

Trimming the system in the atmospheric flight phase is a non-trivial task. A trim point is a point in the parameter space of a dynamic system at which it is in steady state, i.e. the derivatives of the state variables are zero [48, 49]. A trim point satisfies the condition $\dot{x} = 0$. However, given that this is a time-varying system, some of the state derivatives are not zero in nominal operation. Therefore, the choice of the initial condition for the trimming procedure, as well as restrictions for the states, are essential to obtain reliable results. The system will be trimmed along a reference trajectory in the $x_b y_b$ -plane, defined in Figure 2.1b of chapter 2. Finding an equilibrium point around the defined nominal trajectory is a sensitive procedure because the system has many degrees of freedom. This process is essentially an optimization that minimizes the absolute value of $|x - x(0)|$, subject to a number of constraints, returning the deflection of the TVC control system that meets the requirements. The system has three inputs, $\mathbf{u} = [\delta_p \ \delta_y \ T]^T$. However, given that the first stage engine is a solid rocket booster the thrust profile is known at all times. Hence the thrust input is fixed and only the deflection of the TVC system needs to be computed in the trimming procedure. To reduce the degrees of freedom of the system and to ensure that feasible trim points are obtained, some assumptions are made:

- Rigid body - flexible modes not considered;
- States related with inertial position not considered (they are not in steady state and can be derived from the other states);

- Movement occurs in the $x_b y_b$ -plane $\rightarrow w = 0$.

The model used for trimming has 10 states, $\mathbf{x} = [u \ v \ w \ p \ q \ r \ \phi \ \theta \ \psi \ m]^T$ and the initial guess for the states will be zero, except for the states that define the trajectory of the launch vehicle: u , v , ψ and m . It is important to note that considering the trajectory in the $x_b y_b$ -plane is a simplification: in fact the trajectory of the launch vehicle occurs in 3D space, but given that the magnitude of the velocity along the z_b -axis is small, it was considered zero to force the convergence of the trimming algorithm.

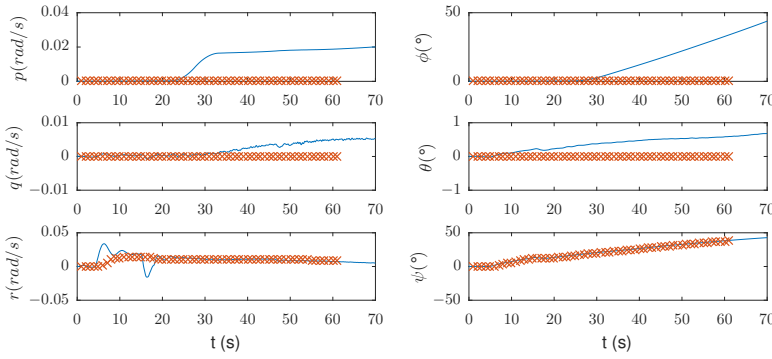
The algorithm used for trimming is the standard `trim` function [48], that comes with Matlab. This algorithm allows setting several options: the initial state, (x_0), initial input, (u_0), initial output, (y_0), state, input and output values that must be met exactly, (ix , iu , iy), initial derivative of the state, (dx_0) and derivative value that must be met exactly, (idx_0). All these options allow the user to specify the region around which the optimization process must start its search. The initial search parameters are detailed in table 3.1. The subscript t indicates that the value for that variable is the value of the state in the reference trajectory, at a given time, obtained from a reference simulation of the launch vehicle trajectory.

	State (x_0)	Known exactly? (ix)	State derivative (dx_0)	Known exactly? (idx_0)
u	u_t	Yes	No	No
v	v_t	Yes	No	Yes
w	0	Yes	No	No
p	0	No	No	No
q	0	No	No	No
r	0	No	No	No
ϕ	0	No	No	No
θ	0	No	No	No
ψ	ψ_t	No	No	No
m	m_t	No	No	No
	Input (u_0)	Known exactly? (iu)	State derivative (du_0)	Known exactly? (idu_0)
δ_p	0	No	No	No
δ_y	0	No	No	No
T	T_t	Yes	No	No

Table 3.1: State and state derivatives conditions for trimming

With the options defined earlier, the nonlinear model was trimmed from $t = 0$ s to $t = 60$ s, obtaining one trim point per second. Figure 3.1 shows the trim points found against the nominal trajectory of the launcher. It can be seen that ψ is followed and the trend of r follows the nominal trajectory, because ψ_t is different from zero. All other variables are zero in equilibrium.

The maximum deflection of the TVC system is $\pm 6.5^\circ$ in both directions (pitch and yaw), so the equilibrium point would only be accepted if the maximum deflection found for the TVC angles was within this bound. Note that the derivative \dot{v} is forced to be zero, for convergence purposes: if \dot{v} is left free, the requirements of the maximum deflection for the TVC are violated.



(a) Angular velocity trim points

(b) Euler angles trim points

Figure 3.1: Comparison of the launcher's nominal trajectory (blue) with the trim points (red crosses)

3.2. LINEARIZATION

With the trim points obtained in the previous section, it is possible to linearize the system around the nominal trajectory and control the deviation from the reference.

For small deviations around an equilibrium point $(\mathbf{x}^*, \mathbf{u}^*)$, a nonlinear function can be approximated by its Taylor series expansion under certain conditions [50, 51]:

$$f(\mathbf{x}, \mathbf{u}) = f(\mathbf{x}^*, \mathbf{u}^*) + \left. \frac{\partial f(\mathbf{x}, \mathbf{u})}{\partial \mathbf{x}} \right|_{\substack{\mathbf{x}=\mathbf{x}^* \\ \mathbf{u}=\mathbf{u}^*}} (\mathbf{x} - \mathbf{x}^*) + \left. \frac{\partial f(\mathbf{x}, \mathbf{u})}{\partial \mathbf{u}} \right|_{\substack{\mathbf{x}=\mathbf{x}^* \\ \mathbf{u}=\mathbf{u}^*}} (\mathbf{u} - \mathbf{u}^*) + \underbrace{\frac{1}{2!} \left. \frac{\partial^2 f(\mathbf{x}, \mathbf{u})}{\partial \mathbf{x}^2} \right|_{\substack{\mathbf{x}=\mathbf{x}^* \\ \mathbf{u}=\mathbf{u}^*}} (\mathbf{x} - \mathbf{x}^*)^2 + \dots}_{\text{H.O.T.}} \quad (3.1)$$

If the deviation is small, higher order terms (H.O.T.) can be neglected, in the neighbourhood of the operating point [50, 52].

Rewriting the equation as a function of the perturbed variables, $\tilde{\mathbf{x}} = \mathbf{x} - \mathbf{x}^*$ and $\tilde{\mathbf{u}} = \mathbf{u} - \mathbf{u}^*$, one can write a state space system that represents the system in the neighbourhood of the operating point. The output equation, $h(\tilde{\mathbf{x}}, \tilde{\mathbf{u}}, t)$ in this case coincides with the state vector, i.e., $h(\tilde{\mathbf{x}}, \tilde{\mathbf{u}}, t) = \tilde{\mathbf{x}}$. The state space system near the operating point is given by Eq. (3.2).

$$\begin{cases} \dot{\tilde{\mathbf{x}}} = \underbrace{\frac{\partial f(\mathbf{x}, \mathbf{u})}{\partial \mathbf{x}}}_A \tilde{\mathbf{x}} + \underbrace{\frac{\partial f(\mathbf{x}, \mathbf{u})}{\partial \mathbf{u}}}_B \tilde{\mathbf{u}} \\ y = \underbrace{\frac{\partial h(\mathbf{x}, \mathbf{u})}{\partial \mathbf{x}}}_C \tilde{\mathbf{x}} + \underbrace{\frac{\partial h(\mathbf{x}, \mathbf{u})}{\partial \mathbf{u}}}_D \tilde{\mathbf{u}} . \end{cases} \quad (3.2)$$

The matrices A , B , C , and D are the Jacobians of the nonlinear system with respect to the state and input variables. The output is the state vector, $\tilde{\mathbf{x}}$, hence $C = I_{10 \times 10}$. At this point, no disturbances are considered, i.e. $D = 0_{10 \times 3}$.

Taking the partial derivatives of the model with respect to the state yields the A matrix with the following structure:

$$A = \begin{array}{c|ccc|ccc|ccc|c} \hline 0 & r & -q & 0 & -w & v & 0 & gc\psi s\theta & gc\theta s\psi & & M_u \\ -r & 0 & p & w & 0 & -u & -g(s\phi s\psi + c\phi c\psi s\theta) & -gc\psi c\theta s\phi & g(c\phi c\psi + s\phi s\psi s\theta) & & M_v \\ q & -p & 0 & -v & u & 0 & -g(c\phi s\psi - c\psi s\phi s\theta) & -gc\phi c\psi c\theta & -g(c\psi s\phi - c\phi s\psi s\theta) & & M_w \\ \hline 0 & 0 & 0 & 0 & 0 & 0 & 0 & 0 & 0 & & 0 \\ 0 & 0 & 0 & I_{yy}r & 0 & I_{yy}p & 0 & 0 & 0 & & 0 \\ 0 & 0 & 0 & I_{zz}q & I_{zz}p & 0 & 0 & 0 & 0 & & 0 \\ \hline 0 & 0 & 0 & 1 & s\phi t\theta & t\theta & c\phi t\theta q & \frac{s\phi}{c^2\theta}q & \frac{r}{c^2\theta} & & 0 \\ 0 & 0 & 0 & 0 & c\phi & -s\phi & -s\phi q - c\phi r & 0 & 0 & & 0 \\ 0 & 0 & 0 & 0 & \frac{s\phi}{c\theta} & \frac{c\phi}{c\theta} & \frac{c\phi}{c\theta} - \frac{s\phi}{c\theta}r & -\frac{s\theta}{c^2\theta}(s\phi q + c\phi r) & 0 & & 0 \\ \hline 0 & 0 & 0 & 0 & 0 & 0 & 0 & 0 & 0 & & 0 \\ \hline \end{array} \quad (3.3)$$

where M_u , M_v and M_w are the partial derivatives of u , v and w with respect to the mass.

Likewise, taking the partial derivatives of the model with respect to the control variables yields the B matrix:

$$B = \begin{array}{c|ccc} \left[\begin{array}{ccc} -\frac{T}{m}c\delta_y s\delta_p & -\frac{T}{m}c\delta_p s\delta_y & \frac{1}{m}c\delta_p c\delta_y \\ -\frac{T\sqrt{2}/2}{m}c\delta_p c\delta_y & -\frac{T\sqrt{2}/2}{m}(s\delta_y s\delta_p + c\delta_y) & \frac{\sqrt{2}/2}{m}(s\delta_y - c\delta_y s\delta_p) \\ \frac{T\sqrt{2}/2}{m}c\delta_y c\delta_p & -\frac{T\sqrt{2}/2}{m}(c\delta_y - s\delta_y c\delta_p) & -\frac{\sqrt{2}/2}{m}(s\delta_y - c\delta_y s\delta_p) \\ 0 & 0 & 0 \\ \frac{l_{CG}T\sqrt{2}/2}{I_{yy}}c\delta_p c\delta_y & -\frac{l_{CG}T\sqrt{2}/2}{I_{yy}}(c\delta_y + s\delta_y s\delta_p) & -\frac{l_{CG}\sqrt{2}/2}{I_{yy}}(s\delta_y - c\delta_y s\delta_p) \\ 0 & 0 & 0 \\ 0 & 0 & 0 \\ 0 & 0 & 0 \\ 0 & 0 & 0 \end{array} \right] \cdot (3.4) \end{array}$$

It is important to note that matrices (3.3) and (3.4) are missing the contribution due to aerodynamic angles. Examining Eq. (2.25), there is a clear dependence on the aerodynamic angles, that in turn is a function of state variables. The aerodynamic angles and airspeed are defined as:

$$\begin{cases} \alpha = \arctan \frac{w}{u} \\ \beta = \arctan \frac{v}{V} \\ V = \sqrt{u^2 + v^2 + w^2} \end{cases} \quad (3.5)$$

Combining Eq. (3.5) with Eq. (2.25) it is possible to describe the dependence of the aerodynamic angles and include its derivatives in matrices A and B . However, due to the complexity of these partial derivatives, they are omitted in this document. Nevertheless, they were computed using Matlab's Symbolic Math toolbox, and the results were used to check the Jacobians obtained with `linmod`. By using the linear model, the stability of the system will be assessed and linear controllers will be designed in chapter 4.

4

LINEAR CONTROL

The linear model obtained in the previous chapter can be used to design classic linear controllers to stabilize the launch vehicle and enable reference tracking. This chapter is devoted to classic linear control design, using PID and LQR control. The objective of the controllers is to stabilize the system for all the different trim points.

Given that the system's mass is variable, the characteristics of the linearized system change with time, there is no guarantee that a controller designed for a given trim point can stabilize the system for all trim conditions (recall that linear control is developed to control the deviations around an equilibrium point, and these conditions change with time). Therefore, it is necessary to know the evolution of the poles of the system in order to design a controller that stabilizes the system for all the trim conditions. Hence, the starting point of this chapter is a detailed analysis of the poles of the linearized system, to gain insight about the evolution of the dynamics of the launch vehicle with time. After this step, the control of the nominal system will be considered. In the nominal system, there are no disturbances and it is assumed that all the variables are available for control. In fact, the launcher is assumed to only possess inertial sensors, meaning that only information available from onboard gyroscopes is available. Furthermore, in the presence of wind, there will be a difference between the groundspeed and the airspeed, meaning that the controller needs to be designed to account for this difference.

The goal of this chapter is to establish a benchmark with the classic control methods used for these systems. Hence all the referred problems will be considered in the nonlinear controller: for the remainder of this chapter nominal conditions are considered.

4.1. ANALYSIS OF POLES OF THE LINEARIZED SYSTEM

After trimming and linearization a 10 states state-space model is obtained, for each linearization point. Linearization was performed every second from $t=0$ to $t=60$, yielding 60 linear systems, that describe the evolution of the nonlinear system in time.

Recalling the assumptions of Section 3.1, the state vector after trimming and linearization is $\mathbf{x} = [u \ v \ w \ p \ q \ r \ \phi \ \theta \ \psi \ m]^T$. To simplify the analysis, the system will be decoupled into longitudinal and lateral models. Due to the axial symmetry of the launch vehicle, and provided that the roll angle is small, this assumption is valid [33]. Usually, launch vehicles have a [Roll and Attitude Control System \(RACS\)](#), that counteracts any

perturbation torques that cause the roll angle to increase over a safety threshold. Hence it is reasonable to assume that the roll angle is always small. Furthermore, at the trim points, the roll angle is always zero, as illustrated in Figure 3.1b.

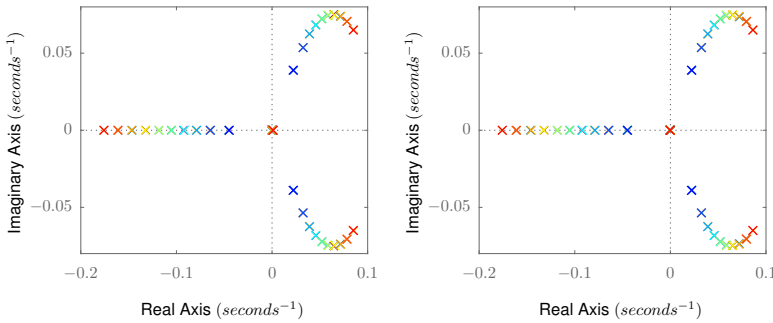
Defining $\mathbf{x}_{\text{long}} = [u \ v \ r \ \psi]^T$ as longitudinal variables and $\mathbf{x}_{\text{lat}} = [w \ p \ q \ \theta]^T$ as lateral variables, it is possible to separate the linearized system, while maintaining essential information about the dynamics. Note that the mass is not included in any of the models as it is considered a frozen parameter for each linearization point. Also, the roll angle is not a state variable in any of the models, as it is considered to be small and does not influence the dynamics of the lateral or longitudinal systems.

A first check of this assumptions can be performed by evaluating the eigenvalues of the full linearized model and comparing them with the eigenvalues of both reduced systems, shown in table 4.1, for $t = 10$ s. The eigenvalues of the separated systems are the same as the full system and the structure of the lateral and longitudinal models is similar, as expected, due to the axial symmetry of the vehicle.

Full system	Longitudinal system	Lateral system
$-0.1762 + 0.0000i$	$-0.1762 + 0.0000i$	$-0.1760 + 0.0000i$
$-0.1756 + 0.0000i$	$0.0856 - 0.0652i$	$0.0866 + 0.0651i$
$0.0856 + 0.0652i$	$0.0856 + 0.0652i$	$0.0866 - 0.0651i$
$0.0856 - 0.0652i$	$0.0006 + 0.0000i$	$0.0000 + 0.0000i$
$0.0864 + 0.0657i$		
$0.0864 - 0.0657i$		
$0.0006 + 0.0000i$		
$-0.0001 + 0.0000i$		
$0.0000 + 0.0000i$		
$0.0000 + 0.0000i$		

Table 4.1: Comparison of poles for $t=10$ s between the full model and lateral/longitudinal systems

This analysis is valid for every linearization point, meaning that the system can always be separated into a longitudinal and a lateral model. It is now necessary to check the evolution of the poles, as time increases, to gain insight on the evolution of the system. Figures 4.1a and 4.1b show the evolution of the poles of the longitudinal and lateral systems (respectively), from $t = 0$ s to $t = 10$ s. In the figures, the first ten linearized models are shown and the color of the poles vary from blue to red, from the first to the last models, respectively. Also, to improve the readability of the document, the images of the evolution of poles from $t = 20$ s to $t = 60$ s can be found in Appendix D.



(a) Longitudinal poles associated with state variables $[u \ v \ r \ \psi]$ (b) Lateral poles associated with state variables $[w \ p \ q \ \theta]$

Figure 4.1: Poles of the linearized longitudinal and lateral systems

Based on the previous images and those presented in Appendix D, some conclusions about the evolution of the system in time can be drawn:

- The system is inherently unstable, as there are always poles in the right-half plane;
- Up until $t=30$ s there are unstable complex poles;
- As times increases, the system becomes faster, since the magnitude of the poles increases.

Given the geometry of the launch vehicle, it was known beforehand that the system is inherently unstable. Launch vehicles typically are aerodynamically unstable due to the center of mass lying aft of the center of pressure. Feedback control can stabilize the system by sensing the vehicle attitude and attitude rate and issuing engine gimballed angle commands to generate corrective torques. Whereas the vehicle length contributes to the large negative static margin and the consequent aerodynamic instability, the large moment arm between the gimballed engines and the center of mass also provides ample control authority to stabilize the vehicle, reject disturbances, and satisfy performance requirements [44].

4.2. SISO CONTROL DESIGN

The inputs of the system are the deflection of the TVC system in the pitch and yaw planes, respectively δ_p and δ_y . Since separated systems for longitudinal and lateral motion are available, it is beneficial to redefine the inputs of the system to yield a Single-Input Single-Output (SISO) system for each model. With a SISO system, it is possible to use classical control design tools, such as root locus, Bode and Nichols plots to design a preliminary controller that stabilizes the system. From this baseline controller, it is then easier to design more advanced controllers, such as full state feedback techniques, like the linear quadratic regulator of section 4.3.

4.2.1. REDEFINITION OF THE INPUT

In line with the previous reasoning, it is aimed to find a linear transformation that maps the actual system inputs $\mathbf{u}_{\text{actual}} = [\delta_p \ \delta_y]^T$ to a single input for each of the longitudinal and lateral systems.

The structure of the B -matrix, for both systems (and all trim points) is found to be constant and of the form:

$$\mathbf{B}_{\text{long}} = \begin{bmatrix} | & | \\ b_{\text{long}} & b_{\text{long}} \\ | & | \end{bmatrix}, \mathbf{B}_{\text{lat}} = \begin{bmatrix} | & | \\ b_{\text{lat}} & -b_{\text{lat}} \\ | & | \end{bmatrix}, \quad (4.1)$$

Given that the actual input is the same to both systems:

$$\begin{cases} \mathbf{B}_{\text{long}} \mathbf{u}_{\text{actual}} = \mathbf{b}_{\text{long}} (\delta_p + \delta_y) = \tilde{\mathbf{b}} \tilde{\mathbf{u}} \\ \mathbf{B}_{\text{lat}} \mathbf{u}_{\text{actual}} = \mathbf{b}_{\text{lat}} (\delta_p - \delta_y) = \bar{\mathbf{b}} \bar{\mathbf{u}} \end{cases}, \quad (4.2)$$

Defining:

$$\begin{cases} \tilde{\mathbf{b}} = 2 \cdot \mathbf{b}_{\text{long}}, \quad \tilde{\mathbf{u}} = \frac{\delta_p + \delta_y}{2} \\ \bar{\mathbf{b}} = 2 \cdot \mathbf{b}_{\text{lat}}, \quad \bar{\mathbf{u}} = \frac{\delta_p - \delta_y}{2} \end{cases}, \quad (4.3)$$

the constraints in Eq. (4.2) are satisfied and there are two new definitions for the SISO input of the longitudinal and lateral system, respectively $\tilde{\mathbf{u}}$ and $\bar{\mathbf{u}}$. Having two independent SISO systems, the objective is to design two linear controllers, to stabilize the longitudinal and lateral motions and then test them in the full linearized system as well as in the nonlinear system. The transformation defined in (4.3) is linear and uniquely defined. Provided that the values of $\tilde{\mathbf{u}}$ and $\bar{\mathbf{u}}$ are known, the actual input is given by:

$$\begin{cases} \delta_p = \tilde{\mathbf{u}} + \bar{\mathbf{u}} \\ \delta_y = \tilde{\mathbf{u}} - \bar{\mathbf{u}} \end{cases}. \quad (4.4)$$

4.2.2. LONGITUDINAL CONTROL

Before designing a controller, the choice of the control variables needs to be carefully considered. This is also true for SISO systems, as some channels might exhibit effects such as non-minimum phase zeros that limit the performance of the controller [52]. These effects might be mitigated by the choice of appropriate control variables. Furthermore, given that the structure of the longitudinal and lateral models is similar, it is expected that the controller designed for one model can be applied to the other with minor adaptations. On the long run the goal is to track the reference attitude parametrized by Euler angles. Nevertheless, different control variables will be considered, to gain insight on the dynamics of the system and as such, the first considered control variable is the lateral velocity, v .

YAW ANGLE CONTROL

Given that the objective is to follow a reference profile in Euler angles, the yaw angle (ψ) is chosen as the control variable, yielding the following transfer function at $t=10$ s:

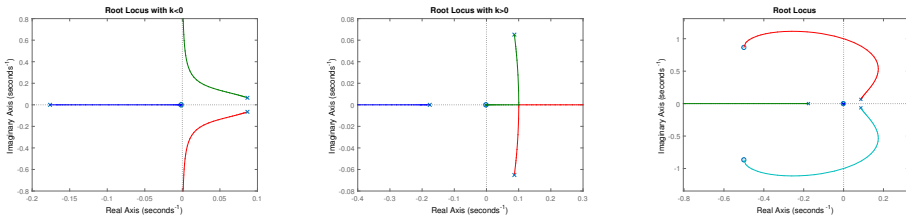
$$\frac{\Psi}{\bar{U}}(s) = \frac{-6.799s - 0.01167}{s^3 + 0.002823s^2 - 0.01878s + 0.002071} \tag{4.5}$$

Poles (rad/s)	Zeros (rad/s)
-0.1762	-0.0017
$0.0867 \pm 0.0652i$	

Table 4.2: Poles and zeros of the yaw angle plant

This transfer function does not have a non-minimum phase zero, so designing a controller to stabilize the plant should be significantly easier than it was for the lateral velocity [52].

The plant root loci, for positive and negative gains (respectively) are shown in Figure 4.2.



(a) Root Locus with positive feedback (b) Root Locus with negative feedback (c) Plant + PID root locus

Figure 4.2: Root locus with negative and positive feedback

Using only a proportional controller it is not possible to bring the poles to the **Left Half Plane (LHP)**. However, choosing positive gain, renders the system marginally stable, as $K \rightarrow \infty$, while closing the loop with negative gain always yields a pole in the **Right Half Plane (RHP)**. Including a **PID** controller stabilizes the system. The new root locus, assuming unitary gains for the **PID** controller, is shown in Figure 4.2c.

For $K_r > 0.149$, the poles of the closed-loop system move to the **LHP** and the system becomes stable. Next, the effect of varying the **PID** gains will be analysed.

ANALYSIS OF THE EFFECTS OF THE PID GAINS

The choice of the **PID** gains have direct influence on the location of the poles and thus on the performance of the closed-loop system. In general terms, the effects of the gains of a **PID** controller can be described as follows:

- The proportional gain alone makes the response faster, but may lead to overshoot and oscillations, and may not lead to zero static error. Furthermore, it may not be able to stabilize the system in the presence of large time delays;
- The integral action is effective for systems without integrators, allowing for zero static error. However, integral action on its own decreases stability and is often combined with proportional action;
- The derivative action is effective in stabilizing systems with large delays, as it allows some prediction about the evolution of the output. However, it is very sensitive to noise.

Combining the previous terms, it is possible to speed up the response and keep a low overshoot.

The structure of the closed-loop transfer function is given in Figure 4.3 and concretized in Eq. (4.6), considering negative feedback and a PID controller.

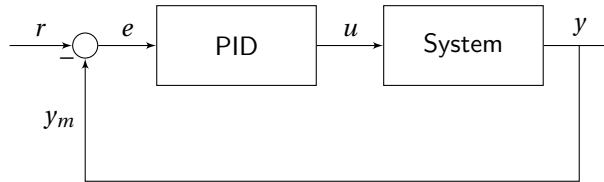


Figure 4.3: Block diagram of the closed-loop structure

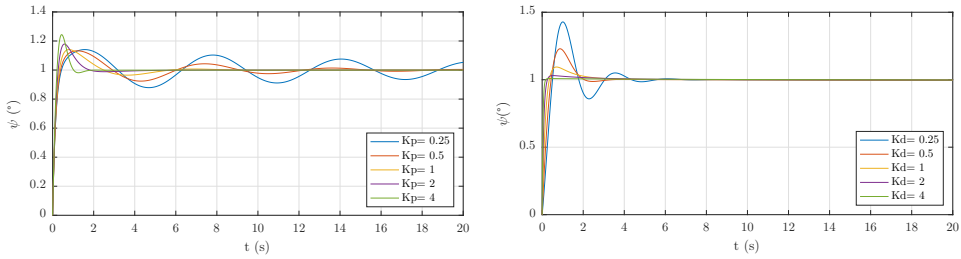
$$CL(s) = \frac{G(s)H(s)}{1 + G(s)H(s)} \quad (4.6)$$

The controller will introduce at most two zeros in the open loop, that will attract the poles, when the loop is closed. The design tool used to tune the PID controller at this stage was the Root Locus. It is noted that this tool is used here due to its simplicity and to find a basic controller to stabilize the system. However, this tool and manual tuning are not suitable for most industrial controller designs and are only used here as proof of concept.

To investigate the effect of each of the PID gains, each gain was changed at a time to check its effect on the overall result. Previously, it was seen that proportional control on its own is not sufficient to stabilize the system (see Figure 4.2a). Hence to evaluate the effect of the proportional gain, it is necessary to fix the other two gains. Fixing $K_i = K_d = 1$, and changing K_p in the range $[0.25, 4]$ yields the responses shown in Figure 4.4a. As expected, increasing the proportional gain increases the speed of the response but also leads to a growing overshoot. The zeros introduced by the PID controller are located at

$$z = \frac{-K_p \pm \sqrt{K_p^2 - 4K_iK_d}}{2K_d} \quad (4.7)$$

With the current settings, the location of the zeros as a function of K_p are given by:



(a) Step response for varying K_p and $K_i = K_d = 1$ (b) Step response for varying K_d and $K_i = 0, K_p = 1$

Figure 4.4: Step responses for varying PID gains

$$z(K_p) = -\frac{K_p}{2} \pm \frac{\sqrt{K_p^2 - 4}}{2} \quad (4.8)$$

Therefore, the zeros will be real for $K_p > 2$. For $K_p < 2$ the zeros get closer to the imaginary axis. With a feedback loop, if the root locus gain increases, the poles will approach these zeros, so for small K_p the response will be more oscillatory and for greater values of K_p the zeros move towards the left, yielding a more stable system. This analysis of the location of the zeros of the controller is in line with Figure 4.4a and gives insight on the behaviour of the closed loop system.

Next, the effect of the derivative gain is investigated, using a PID controller, with fixed proportional gain, very small integrative gain and varying derivative gain. The integrative gain is small to better evaluate the effect of the derivative gain. The results can be seen in Figure 4.4b.

Given the structure of the controller, the zero will be placed at

$$z(K_d) = -\frac{1}{K_d} \quad (4.9)$$

Therefore, as K_d increases, the zero will approach the origin. In fact, in Figure 4.4b it can be observed that for small derivative gains, the response is more oscillatory. As the gain increases, the overshoot is gradually reduced, showing the stabilizing effect of the derivative gain.

Finally, the analysis is carried out for the effect of the integral gain. The results are shown in Figure 4.5. It should be noted that the analysis is carried out for a PID controller and not simply a PI controller, as was the case for the analysis of the derivative gain, because the PI controller is not sufficient to stabilize the system.

Given the structure of the controller, the zeros will be located at

$$z(K_i) = -0.5 \pm \frac{\sqrt{1 - 4K_i}}{2} \quad (4.10)$$

Hence, for $K_i < 0.25$ the zeros will be real and for $K_i > 0.25$ they will be imaginary (but always with the same real part). Therefore, as the integral gain approaches infinity,

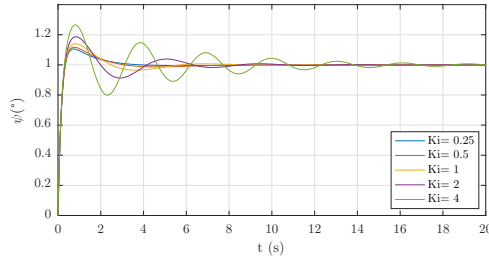


Figure 4.5: Step response for varying K_i and $K_p = K_d = 1$

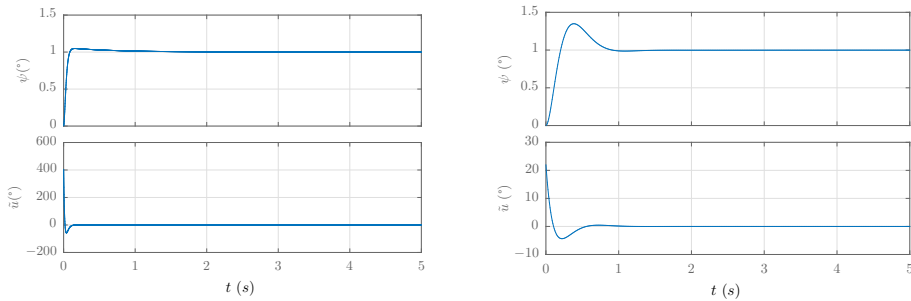
4

the imaginary part of the zeros will be greater than the real part and in the closed-loop system this will result in a more oscillatory response. This is visible in Figure 4.5. As mentioned before, the integral action is effective for systems without integrators. In this case, the control variable is the yaw angle, which already has integral action. Therefore, the system inherently has zero static error and the benefits of the integral action are not as clear as it was the case with proportional or derivative control. Using the insights about the effect of each one of the gains, the PID controller was optimized to yield a response with a low overshoot and fast settling time. Figure 4.6a shows the system response to a step change in the reference signal. The time-domain characteristics of the response are:

Rise Time (s)	0.07
Settling Time (s)	0.92
Overshoot (%)	4.59

Table 4.3: Time-domain response characteristics to a 1° step in ψ

Before proceeding with the application of this controller to the system, it is important to check if the control signal is within the bounds of the actuators. Given the applied transformation, \tilde{u} falls between the upper and lower bounds of the actual control commands, i.e., $\tilde{u} \in [-6.5, 6.5]^\circ$. Plotting the step response and the command signal, in Figure 4.6a, it can be seen that controller is demanding an impossible control signal. Even though the tuned response looked satisfactory, the command signal is not feasible. Therefore, it is necessary to loosen the performance requirements to obtain a feasible control signal.



(a) Yaw angle response for initial PID

(b) Yaw angle response for reduced control effort PID

Figure 4.6: Step responses for the longitudinal system

TUNING FOR REDUCED CONTROL EFFORT

To limit the high-frequency content of the command signal, one can design the PID with a filter in the derivative term. The structure of the controller is:

$$PID(s) = K_p + \frac{K_i}{s} + K_d \frac{N}{1 + N\frac{1}{s}} \tag{4.11}$$

The controller was optimized, yielding the following control response shown in Figure 4.6b. The overshoot increased significantly, but the control effort is within boundaries, as it does not violate the 6.5° boundary. The controller gains and time-domain characteristics of the response are:

K_p	3.64	Rise Time (s)	0.14
K_i	1.075	Settling Time (s)	0.84
K_d	0.942	Overshoot (%)	34.9
N	20		

Table 4.4: PID tuning and time-domain response to a 1° step in ψ , with reduced control effort

FREQUENCY DOMAIN ANALYSIS

Figure 4.7 shows the comparison of the plant open-loop Bode plot, along with the open-loop Bode plot of the controller and the plant together. It is clear that closing the loop without control results in an unstable system, since the plant has negative phase and gain margins.

With the inclusion of the PID controller, the closed-loop will be stable, since the phase margin is positive (45.1°) and the gain margin is negative (-26.5 dB).

The gain and phase margins are important metrics to evaluate the relative stability of the system. The phase margin is defined as $PM = \angle L(j\omega_c) + 180^\circ$

where ω_c is the gain crossover frequency, where $|L(j\omega)|$ first crosses 0 (dB) from above in a Bode diagram. The phase margin tells how much negative phase lag can be

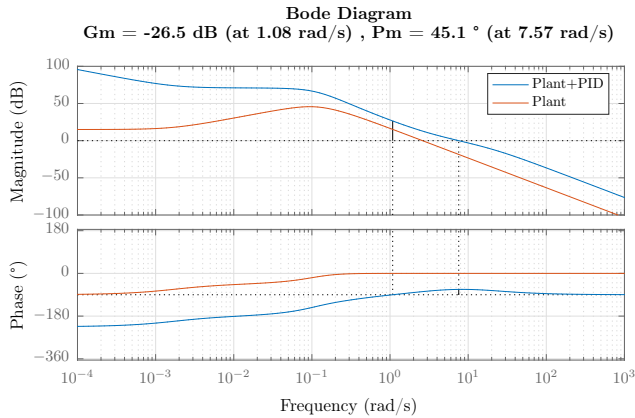
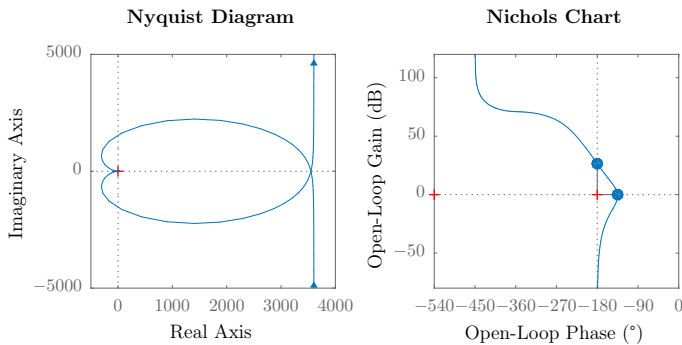


Figure 4.7: Plant vs Plant + PID Bode plot

added to the transfer function $L(s)$ at frequency ω_c before the phase at this frequency becomes -180° , which corresponds to closed-loop instability [52]. The gain margin is defined as $GM = 1/|L(j\omega_{180})|$, where the phase crossover frequency, ω_{180} , is where the phase of the Bode plot crosses -180° . The gain margin is the factor by which the loop gain $|L(j\omega)|$ may be increased before the closed-loop system becomes unstable. The open-loop system has a pair of complex poles in the right half plane and positive feedback was used, hence the negative gain margin has the same interpretation as in a stable system: the modulus of the gain cannot be decreased more than 26.5 dB in order not to generate instability. In other words, there is a lower bound for the gain to guarantee stability.



(a) Nyquist plot for the system at $t=10$ s (b) Nichols plot for the system at $t=10$ s

Figure 4.8: Nyquist and Nichols plot for the system at $t=10$ s

From the Nyquist plot shown in Figure 4.8a, it can be observed that there is no clockwise encirclement of the -1 point. In fact there are two anti-clockwise encirclements of -1, hence the system is stable. Figure 4.8b shows the Nichols plot at $t=10$ s. The

positive phase margin and negative gain margin already observed in Figure 4.7 are shown, confirming that the system is stable.

APPLICATION OF THE DESIGNED CONTROLLER TO THE OTHER TRIMMING POINTS

The designed controller is applied next to all the linearized models, to see if it is robust enough to guarantee stability for all models.

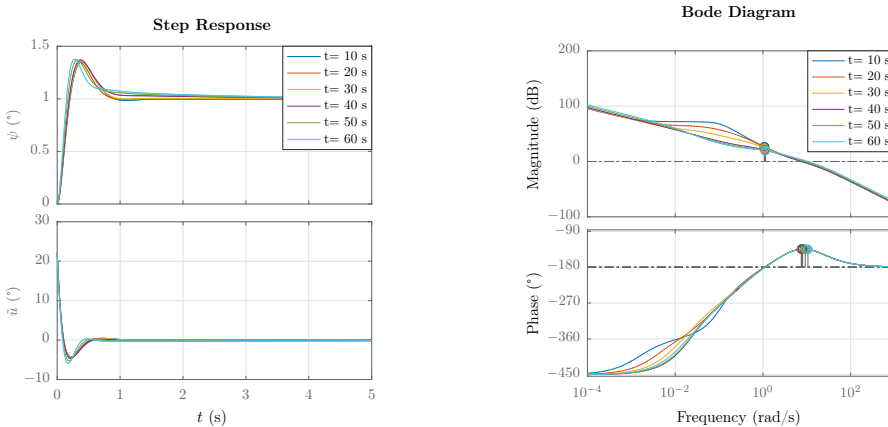
Figure 4.9a shows the step response of the different models, when the PID controller is connected to the models. It can be seen that the controller is able to stabilize all models, although the performance is slightly degraded for the models after $t=10$ s. More importantly, for all the systems, the control signal satisfies the bounds.

	t=10 s	t=20 s	t=30 s	t=40 s	t=50 s	t=60 s
Rise time (s)	0.14	0.13	0.14	0.13	0.11	0.1
Settling Time (s)	0.84	0.51	0.89	2.35	3.03	3.46
Overshoot (%)	34.9	34.7	35.7	36.9	37.1	37.7

Table 4.5: Step response characteristics of the different systems

Table 4.5 shows the step response characteristics of the controller connected to the different linearized systems. As discussed before, the settling time and the overshoot increase with the instant of the linearization.

Figure 4.9b shows the bode plots of the different models, with the PID controller. All systems remain stable: every system exhibits a positive phase margin and negative gain margin, albeit slightly different. Table 4.6 shows the stability margins for the different systems and supports these conclusions.

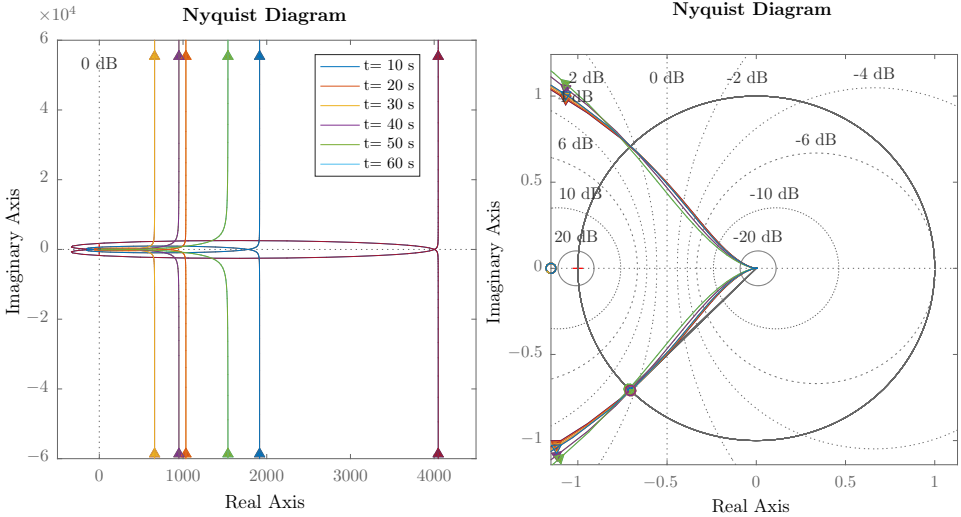


(a) Step responses, from $t=0$ s to $t=60$ s (b) Bode plots, from $t=0$ s to $t=60$ s

Figure 4.9: Step response and Bode plot for all systems from $t=10$ s to $t=60$ s

	t=10 s	t=20 s	t=30 s	t=40 s	t=50 s	t=60 s
Gain Margin (GM) (dB)	-26.54	-26.54	-24.15	-20.92	-20.23	-19.56
GM Frequency (rad/s)	1.082	1.084	1.09	1.112	1.124	1.134
Phase Margin(PM) (°)	45.1	45.2	45.12	45.3	45.16	44.42
PM Frequency (rad/s)	7.57	8.03	7.55	8.02	9.36	10.76

Table 4.6: Stability margins for the different systems



(a) Nyquist plots, from t=0 s to t=60 s

(b) Zoom-in of the Nichols plots, from t=0 s to t=60 s

Figure 4.10: Nyquist plots for the systems from t=10 s to t=60 s

The Nyquist plots are shown in Figure 4.10. In the Nyquist plot, from Figure 4.10a there are two anti-clockwise encirclements of the -1 point, indicating stability. Figure 4.10b shows a zoom-in of the Nyquist plots around the unit circle. It can be seen that the phase margin is positive, as the angle of the intersection between the Nyquist plots and the unit circle is approximately 45° , marked with colored dots in Figure 4.10b. The gain margin is negative, which is consistent with the fact that the plot is originally unstable. More relevant, is that the behaviour of all models is similar and the portion of the graph between the points where the phase and gain margins are evaluated does not get close to the point -1 , which indicates good relative stability margins.

4.2.3. LATERAL CONTROL

The analysis performed in the previous section for longitudinal control was also conducted for the lateral motion. Based on experience from the longitudinal control, the chosen control variable is the pitch angle, θ . Given that the structure of the two motions

was found to be similar in section 4.1, the PID controller designed for the longitudinal motion was applied to the lateral motion.

Using the root locus technique it was found that the system is stabilizable with negative feedback.

The transfer function of the SISO plant is:

$$\frac{\Theta}{\bar{U}} = \frac{6.799s^2 + 0.01165s - 4.376 \times 10^{-35}}{s^4 + 0.002825s^3 - 0.01875s^2 + 0.002068s} \quad (4.12)$$

The controller is able to stabilize all the considered models. Given that the conclusions from the longitudinal motion still hold in this case, only the step response is shown here, in Figure 4.11.

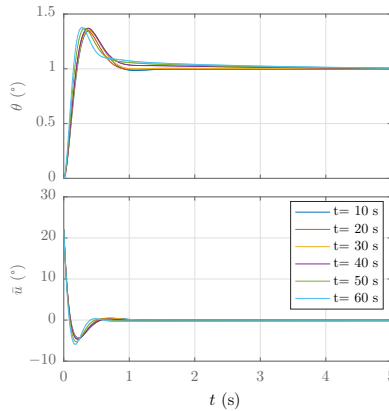


Figure 4.11: Pitch angle response to a step input in \bar{u} for different systems, from $t=0$ s to $t=60$ s

This controller does not exceed the boundaries of the control input. The following sections will detail the implementation of the controllers in the full linear system.

4.2.4. IMPLEMENTATION OF THE PID CONTROLLERS IN THE FULL LINEAR SYSTEM

Having designed separate controllers for the longitudinal and lateral motions, both controllers need to be implemented in the full linear system. With the designed controllers, it should be possible to follow the references in pitch and yaw angles, while maintaining the other states bounded. It is important to note that to obtain the actual control signal for the linear system, it is necessary to take the outputs from the two PID controllers and apply the transformation described in Eq. (4.4).

Figures 4.12a and 4.12b show the results of the simulation of the full linear system. In Figure 4.12b, it can be seen that the controller is able to track the reference, while keeping the remaining states bounded. The velocity u increases, but this state is hardly affected by the TVC deflection, as it depends almost exclusively on the thrust input, which is an external variable. It is interesting to note that the control deflections shown in Figure 4.12b is the same for both channels even though the reference signal is different.

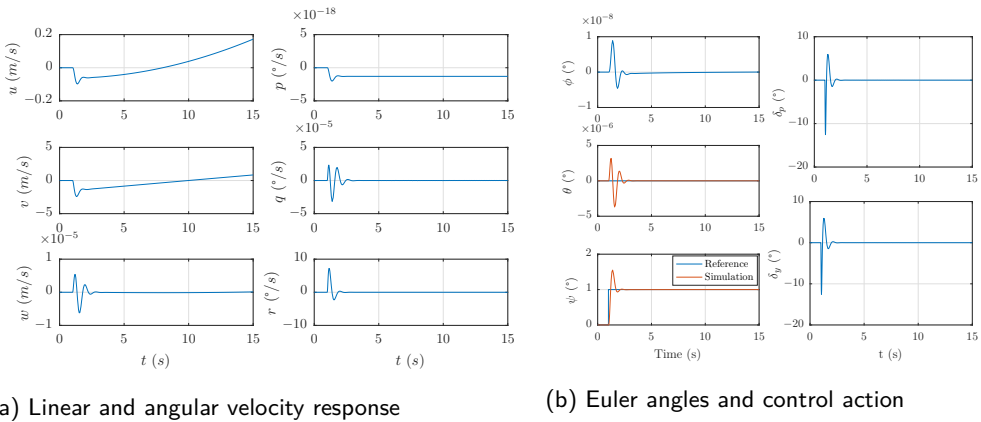


Figure 4.12: PID response to a 1° step input in ψ

This is due to the geometry of the system: the control system frame is placed at 45 degrees with the main structural frame, so to achieve a given reference angle in one of the channels a deflection in both control angles is usually necessary. Furthermore, the control deflections remain bounded. Due to the sudden change in the reference signal, an initial spike is observed in the response of the system. In the nonlinear system, when tracking the reference attitude this effect should not occur, because the reference is smooth and starts from zero.

4.2.5. IMPLEMENTATION OF THE PID CONTROLLERS IN THE NONLINEAR MODEL

In the previous section, it was seen that the designed controllers are able to stabilize the system and track a reference while maintaining the other states bounded. Now the behaviour of the control system in the nonlinear model will be studied. The implementation is similar to the full linear system and the results are shown in Figures 4.13a and 4.13b. The control system is able to follow the Euler angles profile (see Figure 4.13b), producing a control action within the actuator bounds (see Figure 4.13a). It is important to note that the reference trajectory changes slowly in time and starts from zero. Hence, the PID controllers are sufficient to stabilize the system and enable reference tracking. However, in the presence of disturbances, it is expected that the performance of the system is severely degraded. This will be discussed in Chapter 7.

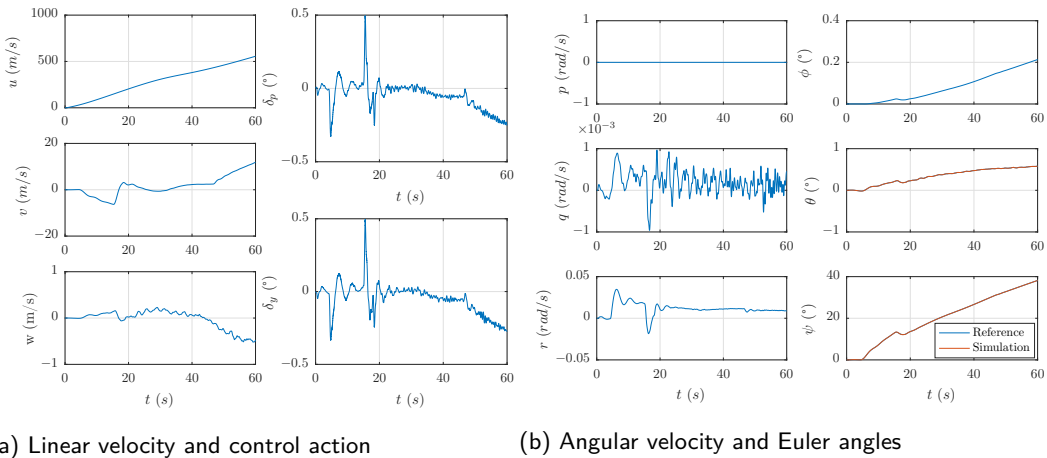


Figure 4.13: Simulation of the PID in the nonlinear system

4.2.6. FLEXIBLE MODES

Thus far the launch vehicle was considered a rigid body, but in fact it is elastic and affected by flexible modes. To get insight about the effect of flexible modes in the vehicle, their application in the linear system is considered in this section. The longitudinal SISO model obtained in Section 4.2 will be used, adding the flexible modes to it. As seen before the open-loop plant is unstable. Hence, the analysis is performed including the designed PID controller. A first approach to deal with flexible modes is to increase the loop gain. It is expected that the magnitude of the tracking error increases with the flexible modes, hence increasing the loop gain forces a stronger control action, reducing the tracking error. To check if this approach indeed enhances the performance of the system, the root locus of the open-loop plant in series with the PID controller is considered in Figure 4.14. Examining the Figure, it is clear that increasing the loop gain brings the poles of the closed loop system further into the LHP. However, as the gain increases, the poles of the flexible modes move to the RHP, indicating instability. Furthermore, a small increase of the loop gain ($K=1.43$) already places the poles in the RHP, which indicates that the system with the flexible modes is sensitive to changes in the gain. Further increasing the gain, the poles of the flexible modes return to the LHP, which could indicate that if the gain is sufficiently high the system can be stable. However, increase the gain indefinitely may excite unmodelled dynamics or request a control signal that the actuators cannot deliver (the root locus does not account for actuator modelling and saturation). To check if this is the case, some simulations will be performed with and without actuators and the results will be compared.

Figure 4.15a compares the response of the nominal system (in blue) with the response of the system with loop gain, $K_{rI} = 1.5$. It is evident that the performance of the nominal system is affected by the flexible modes, since the response is oscillatory and very poorly damped and the response oscillates around the equilibrium (at $\psi = 1^\circ$) for a long time. Nevertheless, these oscillations vanish after some time. Increasing the loop gain, the oscillations around the equilibrium are amplified, indicating that the controller is exciting

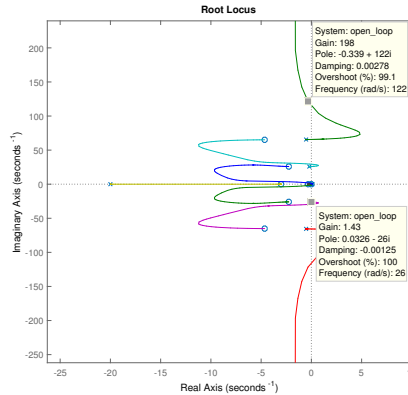
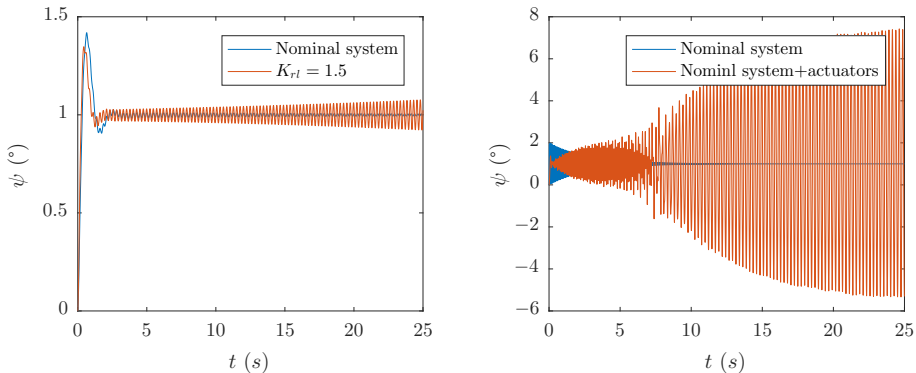


Figure 4.14: Root Locus for the longitudinal system with flexible modes and PID controller

the flexible modes, ultimately leading to instability.

Figure 4.15b shows the response of the system with and without actuators for $K_r l = 200$. From Figure 4.14, for $K_r l > 200$, the poles of the flexible modes are both in the LHP, which indicates stability. Indeed, looking at the response without the actuator (blue line), the system is able to track the reference, albeit with bad performance. However, including the saturation of the actuators in the model, (red line) the oscillations are not damped and in fact are amplified. This means that the actuator is saturated and although theoretically by increasing the loop gain the system could be stabilized, in practise this is not true because the actuator is saturated and cannot execute the control command.



(a) Step response of the nominal system with flexible modes, for increasing root-locus gain and (b) Step response of the nominal system with actuators, for $K_r l = 200$

Figure 4.15: Step response of the linear system to a 1° reference in ψ

Looking at the equations of the flexible modes, Eq. (2.27), the driving input of the modes is the thrust along y_B , which depends directly on the control signal. Hence, the flexible modes are excited by the control signal. Increasing the gain, the magnitude of the

control signal also increases, so the influence of the flexible mode will be greater. This unwanted feedback loop can lead to major problems if the controller is not dimensioned correctly.

4.3. LQR CONTROL

Linear Quadratic Regulator (LQR) control is a state feedback technique, meaning that all states are assumed to be fed to the controller.

Intuitively, from the model presented in Chapter 2, the roll angle (there is no dynamical description for this state) and the mass (the control variables have no influence in this state) are not controllable.

For a controllable system, the controllability matrix, $R = [B \ AB \ A^2B \ \dots \ A^{n-1}B]$ must be full rank [50, 51]. The number of uncontrollable states can be computed as $\#Unco_{states} = n - rank(R)$, where n is the number of states of the system. Computing the number of uncontrollable states for the linearized model described in section 3.2, yields two uncontrollable states, which is in line with the previous reasoning.

The goal of the LQR controller is to allow tracking of Euler angles reference and it was seen before that the effectiveness of controlling the linear velocity is low. Hence, the LQR controller is implemented using the model of the angular velocities and Euler angles, $[q \ r \ \theta \ \psi]$, which provides a description of the system which is controllable.

To facilitate the tuning of the controller, first-order high-pass filters are placed in the control variables, $[\delta_p \ \delta_y]$ and (first-order) low-pass filter are placed in the Euler angle states. The resulting system for the synthesis of the LQR controller has 8 states, $[\delta_{p_{effort}} \ \delta_{y_{effort}} \ q \ r \ \theta \ \psi \ lp_{\theta} \ lp_{\psi}]$, that will be fed to the controller. A block diagram of the synthesis model is presented in Figure 4.16a, while the block diagram of the LQR and filters applied to the model can be seen in Figure 4.16b. The effect of the filters in the control synthesis will be detailed in the following sections.

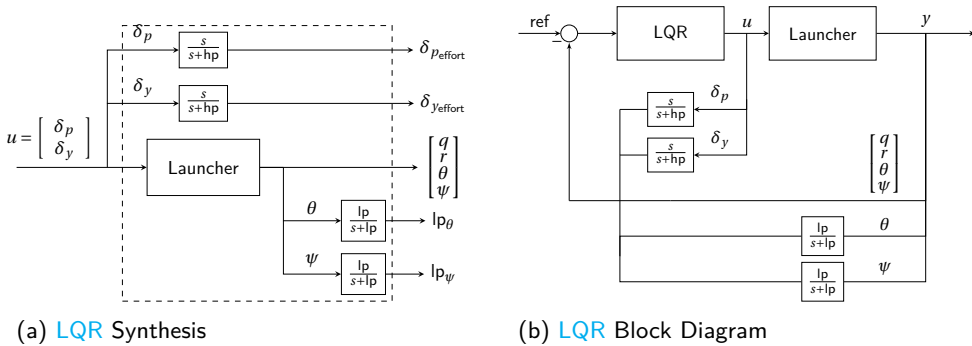


Figure 4.16: LQR synthesis and implementation block diagrams

4.3.1. CHOICE OF LQR WEIGHTS

The LQR control problem is that of finding the control input that minimizes the cost function

$$J_{LQR} = \int_0^{\infty} (\mathbf{x}^T \mathbf{Q} \mathbf{x} + \mathbf{u}^T \mathbf{R} \mathbf{u}) dt \quad (4.13)$$

where $\mathbf{Q} \in \mathbb{R}^{n \times n}$ and $\mathbf{R} \in \mathbb{R}^{m \times m}$ are symmetric positive-definite matrices that weight the relative importance of the state and control energies, in the cost functional expressed in Eq. (4.13). Minimizing both the state and control energy are antagonistic objectives, so the weights \mathbf{Q} and \mathbf{R} allow a trade-off between these two objectives. In a general manner, it is known that [50]:

- If $\mathbf{R} \gg \mathbf{Q}$, the cost function is dominated by the control action term, so the controller minimizes the control action;
- If $\mathbf{R} \ll \mathbf{Q}$, the cost function is dominated by the state energy term, so the controller strives to minimize the state variation, allowing a quicker and stronger control action.

As a starting point for the choice of the weighting matrices, Bryson's rule [50] was used, selecting \mathbf{Q} and \mathbf{R} as diagonal matrices with:

$$Q_{ii} = \frac{1}{\text{maximum acceptable value of } x_i^2}, \quad i = 1, \dots, n$$

$$R_{jj} = \frac{1}{\text{maximum acceptable value of } u_j^2}, \quad j = 1, \dots, m \quad (4.14)$$

Fixing the weight for the state $[q \ r \ \theta \ \psi]$ in \mathbf{Q} and the weights of $[\delta_p \ \delta_y]$ in \mathbf{R} , the weights of the high and low pass filters will be changed and its influence in the system's response will be analysed in the following sections.

EFFECT OF CONTROL EFFORT WEIGHT Q-MATRIX COEFFICIENTS IN THE SYSTEM'S RESPONSE

Figure 4.17 shows the system's response and control action to a step input in θ and zero reference in ψ , for varying high-pass filter coefficient in the Q-matrix (defined as K_{hp}). The high-pass filter prevents high-frequency content in the control signal. Hence, as K_{hp} increases, the importance of minimizing this content increases, so the control action decreases. This is clear from Figure 4.17a where one can see a decrease in the angular velocity as the gain increases and a decrease in the speed of the response to a step input in θ . In Figure 4.17b, one can see that as the gain increases, the control action decreases. Figure 4.18a shows the variation of the control action RMS and tracking error RMS, as a function of K_{hp} . In line with what was observed before, as the gain increases, the control action RMS decreases and the tracking error RMS increases, showing a trade-off between these two parameters.

As a consequence of decreasing the control action, the settling time and overshoot increases with the increase of the gain, as can be seen in Figure 4.18b.

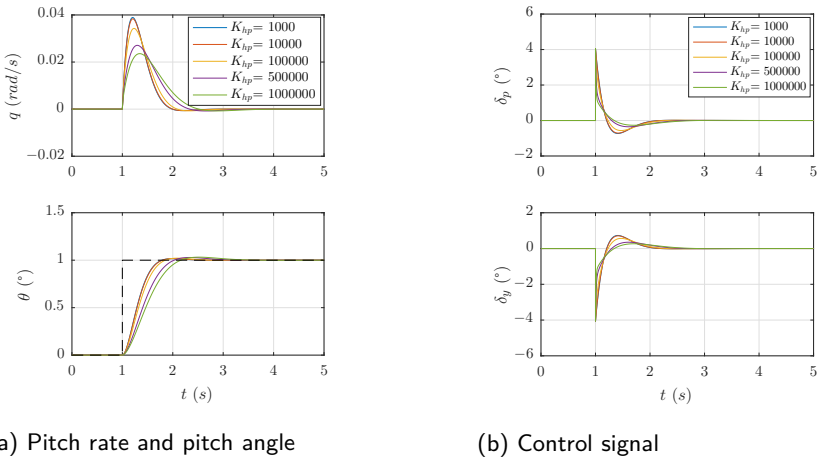
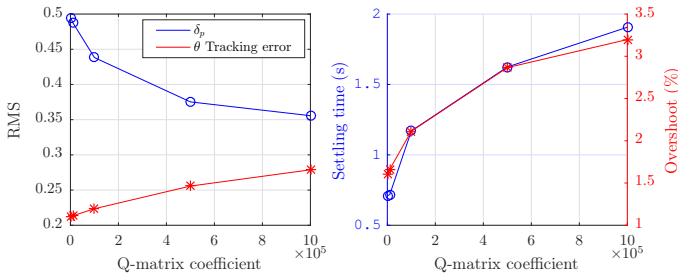


Figure 4.17: System response for varying control effort penalty



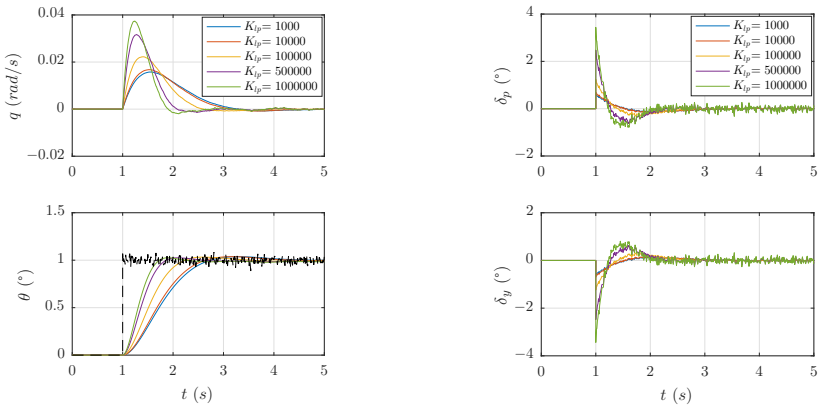
(a) δ_{pRMS} for varying control effort penalty (b) Settling time and OS for varying control effort penalty

Figure 4.18: Performance parameters for varying control effort penalty

EFFECT OF PERFORMANCE WEIGHT Q-MATRIX COEFFICIENTS IN THE SYSTEM’S RESPONSE

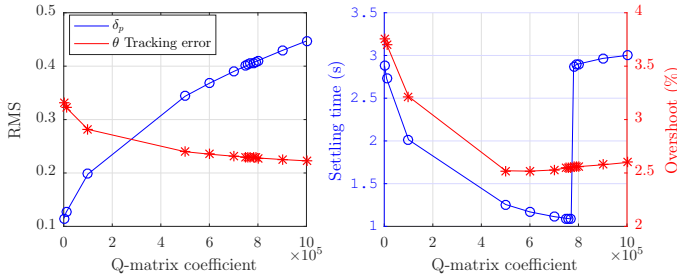
The low-pass filter placed in the control variables θ and ψ reduces the sensitivity of the controller to abrupt variations of the reference signal and to the presence of noise in the reference signal. To evaluate its impact on the design of the controller, a noisy step reference is given to θ and the response is analysed. Figure 4.19 shows the state response and control action for this case. One can see that, as the gain increases, the control action becomes stronger (Figure 4.19b) and the system responds faster (Figure 4.19a). By increasing the performance weight in the Q-matrix associated with the low-pass filters, more importance is given to following the reference signal. Hence, the control action becomes stronger.

Both the settling time and overshoot decrease as the gain increases (Figure 4.20), but after a threshold they increase again. The increase in the settling time is related with the increase in the overshoot: as the overshoot increases, the associated undershoot also increases, surpassing the 2% threshold defined for the settling time. The threshold



(a) Pitch rate and angle for varying performance weight (b) Control signal for varying performance weight

Figure 4.19: System response for varying for varying performance weight



(a) $\delta_{p_{RMS}}$ for varying performance weight (b) Settling time and overshoot for varying performance weight

Figure 4.20: Performance parameters for varying performance weight

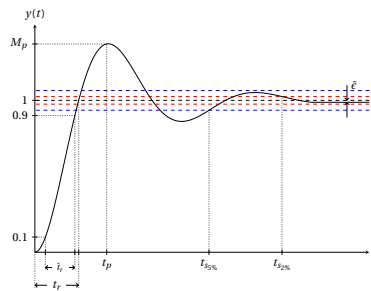


Figure 4.21: Illustration of the different definitions of the settling time

of the settling time can have different definitions, usually 2 % or 5% [50]. Figure 4.21 shows the difference in the settling time with the definition of the threshold at 5 %

and 2 %. In line with the previous reasoning, if the threshold is defined at 5 % it is expected that the settling time decreases as the low-pass performance weight increases. However, given the definition of 2 %, the trend seen in Figure 4.19 is reasonable, given the explanation using Figure 4.21.

After this analysis, it was concluded that the importance of the coefficients of the state ($[q \ r \ \theta \ \psi]$) in the Q-matrix is dominant, when compared to the control effort and low-pass performance weights. A small change in the state gains produced a greater change in the system's behaviour than an equivalent change in the filter Q-matrix coefficients. Using the insight gained on this section, the gains were tuned to obtain a controller that follows the reference signal as fast and smoothly as possible, without exceeding the maximum actuator deflection.

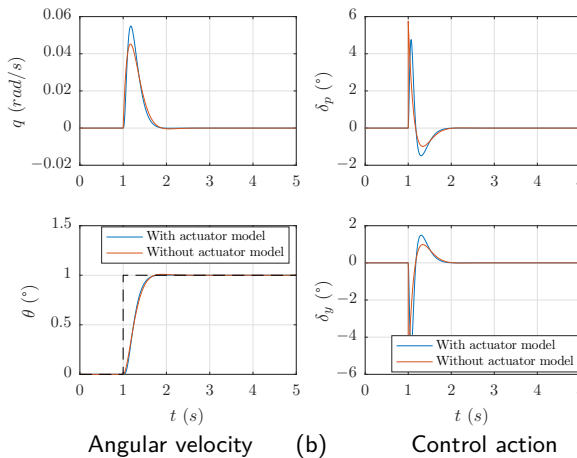
4.3.2. ACTUATOR MODEL

Thus far, the controllers were designed and the control bounds were checked so that the actuator does not reach saturation in the physical system. However, the actuators have dynamics and their response is not immediate. Intuitively, if the controllers designed so far are robust, the inclusion of the actuator model should not have a big impact on the closed-loop system.

The actuators are modelled as second order low-pass filter, with the following transfer function [53, 54]:

$$\frac{\delta_{\text{real}}}{\delta_{\text{commanded}}}(s) = \frac{\omega_{\text{act}}^2}{s^2 + 2\zeta_{\text{act}}\omega_{\text{act}}s + \omega_{\text{act}}^2} \quad (4.15)$$

Figure 4.22 shows the system and control action response with and without the actuator model. It can be seen that the overall system response to a step input does not change significantly, but there is a slight change in the control action response. The actuators are not capable of responding as sharply and quickly as requested in the first seconds of the simulation.



(a) Angular velocity (b) Control action
 Figure 4.22: System's response with and without the actuator model, for the LQR controller

COMPARISON OF THE BEHAVIOUR OF LQR AND PID CONTROLLERS WITH THE ACTUATOR'S MODEL

Figure 4.23 shows the comparison of the response of the PID controller and two different LQR controllers to a reference step input in θ . It is clear that the performance of the LQR controller is significantly better than that of the PID controller, both in terms of overshoot and control action. The PID controller exceeds the limits of the actuation while both LQR controllers stay within bounds. Two possible LQR controllers are shown, but, for implementation in the other systems the least aggressive controller was chosen.

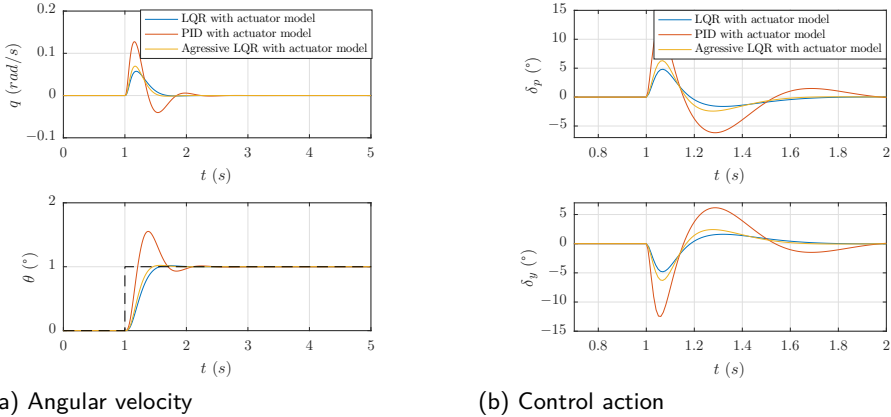


Figure 4.23: Comparison of the PID and LQR controllers, with and without the actuator model

Table 4.7 shows a comparison of the response characteristics with and without the actuator model for the considered controllers. Considering the smooth LQR with and without actuator, the rise time, settling time, and overshoot do not change significantly, but the RMS of the control action increases with the inclusion of the actuator model. Comparing the smooth and the aggressive LQR controllers, the main differences lie in the overshoot and rise time: overshoot is higher and rise time is smaller in the aggressive controller. Furthermore, the RMS of the control action is higher for the aggressive controller. Finally, comparing the response of the PID with LQR, the characteristics of the PID are considerably worse, so the baseline linear controller for the rest of the work will be the LQR controller.

	Smooth LQR without actuator	Smooth LQR with actuator	Aggressive LQR with actuator	PID with actuator
Rise Time (s)	0.4142	0.3604	0.2569	0.1228
Settling Time (s)	0.6423	0.6270	0.6148	2.0303
Overshoot (%)	0.9172	0.1409	2.1430	55.2670
δ_p_{RMS}	0.5944	0.6530	0.8762	1.8575

Table 4.7: Comparison of response characteristics with and without the inclusion of the actuator model

4.3.3. APPLICATION OF THE LQR CONTROLLER TO THE FULL TRAJECTORY

The controller is able to stabilize the system for all instants, as can be seen in Figure 4.24. The control action is within bounds for all models (Figure 4.24b). Hence, this controller may be applied to the nonlinear system, if the trajectory does not deviate much from the reference. The performance degrades for instants far from the design point but this deviation is acceptable considering the fast changes of the system's state between trim points.

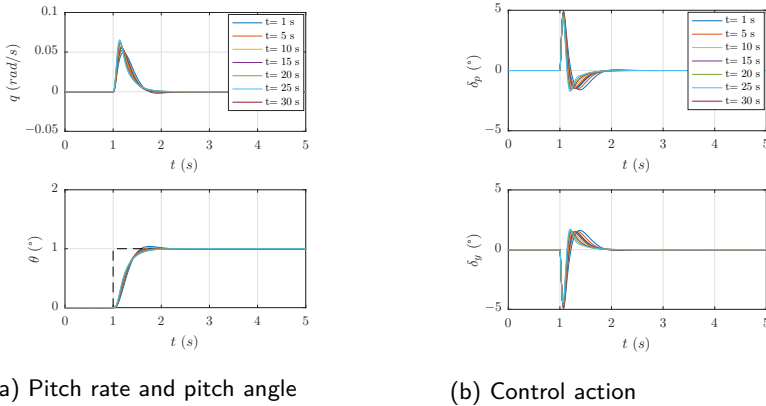


Figure 4.24: System response for all linearized systems with LQR control

As the linearization time increases, the system becomes faster and the settling time (Figure 4.25b) also increases. This is a consequence of applying a controller designed for one specific trim point to faster systems. In terms of overshoot (Figure 4.25a) and control action RMS (Figure 4.25c), as the linearization time increases, those values decrease. However, the tracking error is essentially constant (Figure 4.25c), as it only presents a 2% change.

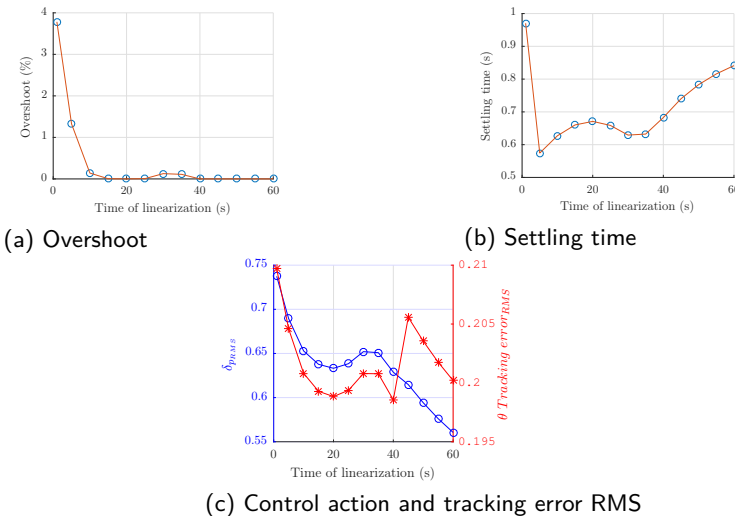
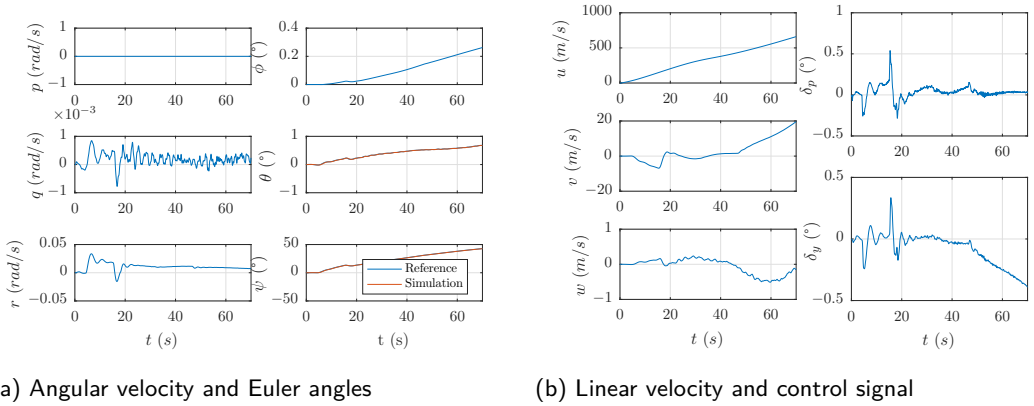


Figure 4.25: Performance parameters for all linearized systems with LQR control

4.3.4. APPLICATION OF THE CONTROLLER TO THE NONLINEAR SYSTEM

As was the case with the PID controller, the designed LQR controller is applied to the nonlinear system in nominal conditions. Figure 4.26 shows the response of the nominal system, with the LQR controller following the nominal pitch and yaw reference. Figure 4.26b shows that the controller is able to track the reference and the control action is within bounds (Figure 4.26b).

Next, the robustness of this controller to parameter variation will be studied. The analysis of the LQR performance in the nonlinear system will be addressed further in Chapter 7.



(a) Angular velocity and Euler angles

(b) Linear velocity and control signal

Figure 4.26: Nonlinear simulation results, with LQR control

4.4. ROBUSTNESS ANALYSIS OF THE LINEAR CONTROLLER

After exploring classical linear system design tools with PID and LQR control, it is necessary to verify the robustness of the controller to variations in the model's parameters. For this study, only the LQR controller will be considered, as it was chosen as the baseline linear controller in section 4.3.2. Nevertheless, the methodology described in this section can also be applied to the PID design.

A well designed controller must be robust to uncertainties in the system parameters. This is particularly applicable to launch vehicles, given its critical application. Thus far, for linear control design, it was considered that the parameters of the system were "frozen" at the time of linearization. Given that the system's parameters vary considerably in time, it is important to guarantee that the controller is able to cope with changes around the nominal values of said parameters.

At this point, it is important to clarify why many of the system's parameters are time-varying and its magnitude have a considerable variation. The system loses mass at a constant rate of $\dot{m} = 900$ kg/s. Henceforth all the parameters associated with mass distribution also change, namely, the position of the center of gravity (\mathbf{X}_{CG}), moments of inertia (I_{xx} , I_{yy} and I_{zz}), in addition to mass (m).

Variation of the aerodynamic coefficients (C_a , C_n) will also be considered, although they are not directly related with the loss of mass of the system.

Furthermore the effect of varying structural parameters such as the position of the nozzle pivot point (\mathbf{X}_{PVP}) and the reference aerodynamic surface of the rocket, S will also be considered.

Each of the aforementioned parameters is varied $\pm 20\%$ around its nominal value and the results are analysed in the following sections. The nominal value of the time-varying parameters is considered as the trim value at $t = 10$ s, to be consistent with previous sections.

The next section shows the analysis for I_{yy} , that was discovered to have an important influence in the behaviour of the system. This analysis was performed for all parameters of the model and the data can be seen in Appendix E. However, for brevity, only I_{yy} (that has a large impact on the system's response) is detailed here.

4.4.1. ANALYSIS OF THE EFFECT OF I_{yy} IN THE PERFORMANCE OF THE SYSTEM

(% I_{yy0})	Complex pole (rad/s)	Frequency (rad/s)
80 %	$-6.39 \pm 2.69i$	6.93
90 %	$-5.68 \pm 3.24i$	6.54
95 %	$-5.38 \pm 3.40i$	6.36
100 %	$-5.11 \pm 3.51i$	6.20
105 %	$-4.87 \pm 3.60i$	6.05
110 %	$-4.65 \pm 3.66i$	5.91
120 %	$-4.26 \pm 3.73i$	5.66

Table 4.8: Variation of the complex conjugate poles with I_{yy}

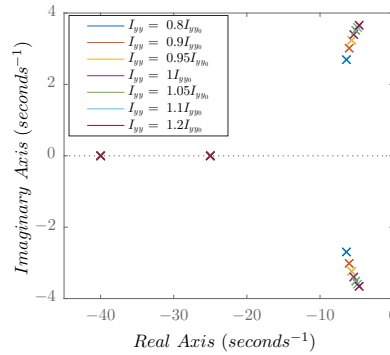
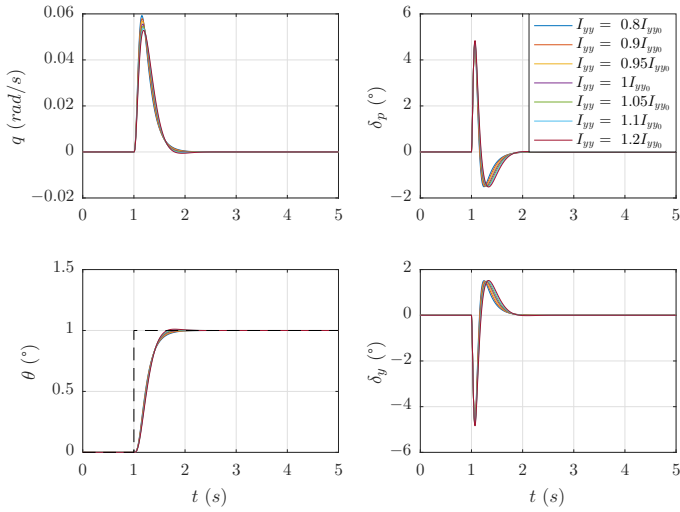


Figure 4.27: Variation of the location of the closed loop poles, with I_{yy}

Figure 4.27 shows the effect of varying $I_{yy} \pm 20\%$ around the nominal value. Increasing the parameter causes the system to be slower (Table 4.8), as the poles get closer to the origin (the magnitude decreases). Decreasing the parameter yields a faster response (see Table 4.8 and Figure 4.27). Physically, decreasing the moment of inertia around the y -axis, means that the body presents less resistance to changes in the rotational motion around this axis. Hence, with the same force intensity, it is possible to achieve a greater rotation.

However, simply looking at the variation of the position of the poles of the system does not guarantee that the controller can stabilize the system, so different metrics need to be used. Figures 4.28 and 4.29 show, respectively, the variation of the response of the system to a step input in θ and the associated performance metrics, when the I_{yy} parameter changes $\pm 20\%$ with respect to its nominal value. A decrease in I_{yy} leads to a decrease of the overshoot and the control action RMS, while the settling time and rise time increase.

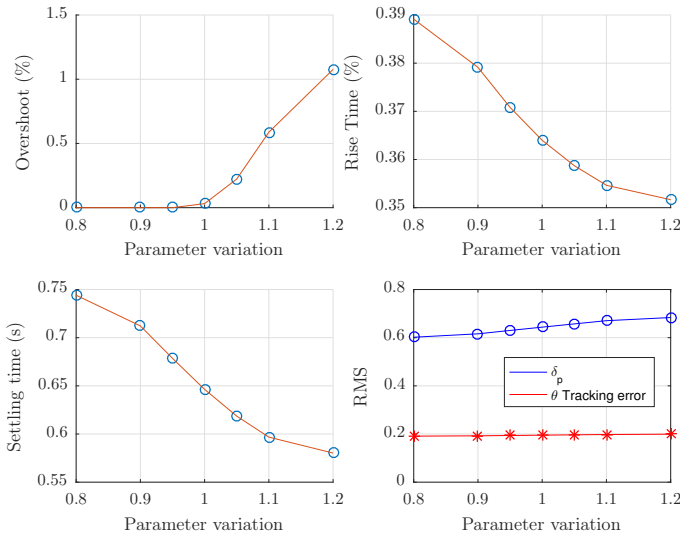
As seen before, decreasing I_{yy} makes the system faster. On the other hand, increasing I_{yy} shows the opposite trend: increase in overshoot and control action RMS and



(a) Pitch rate and angle response to a step input (b) Control signal response to a step input
 Figure 4.28: System responses to a step input, for varying I_{yy} parameter

decrease in rise time and settling time.

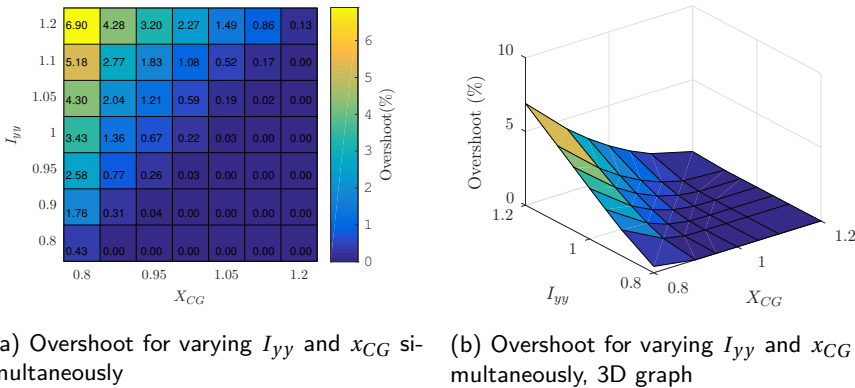
With the previous analysis, the conclusion is that even with a 20% change in the nominal parameter, the controller is able to stabilize the system and the control signal does not exceed the saturation limit.



(a) Overshoot and settling time (b) Rise time and control RMS
 Figure 4.29: Performance indicators for the response for a step input, with varying I_{yy} parameter

4.4.2. ANALYSIS OF THE EFFECT OF VARYING TWO PARAMETERS SIMULTANEOUSLY, IN THE PERFORMANCE OF THE SYSTEM

The analysis performed for I_{yy} in the previous section was extended to all the parameters and it was found that the most influential parameters are I_{yy} , \mathbf{X}_{CG} , and \mathbf{X}_{PVP} . Among the latter three, the two parameters that yield greater variations in the system performance are I_{yy} and \mathbf{X}_{CG} . Therefore, these parameters will be varied simultaneously to check if the controller can handle uncertainty in multiple parameters. Figures 4.30 to 4.35 show the influence of changing I_{yy} and \mathbf{X}_{CG} simultaneously in the system performance. Before detailing each of the results, it is interesting to note that, in all the figures, the influence of increasing both variables by the same amount, yields an almost invariant result. Examining the linear model presented in Eqs. (3.3) and (4.1), a term involving the ratio of both parameters, $\frac{l_{CG}}{I_{yy}} T \frac{\sqrt{2}}{2}$, is present. Recalling that $l_{CG} = \mathbf{X}_{CG} - \mathbf{X}_{PVP}$ and that X_{PVP} is small when compared with \mathbf{X}_{CG} , then the term $\frac{\mathbf{X}_{CG}}{I_{yy}}$ appears. If we change both terms by the same amount, the ratio between them will be constant, so the effect of changing both at the same time results in a constant effect.



(a) Overshoot for varying I_{yy} and x_{CG} simultaneously

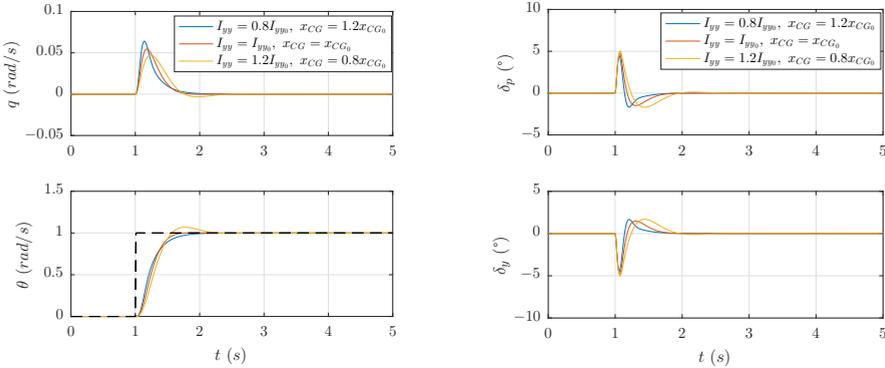
(b) Overshoot for varying I_{yy} and x_{CG} simultaneously, 3D graph

Figure 4.30: Overshoot to a step input, while simultaneously varying I_{yy} and x_{CG}

Figure 4.30 shows the effect of changing both parameters in the overshoot of the response to a step input in θ . From Figure 4.30a, it is clear that the effect of I_{yy} is predominant in the overshoot of the system: if this parameter increases the overshoot tends to increase. As seen before, increasing I_{yy} causes the system to become slower. Intuitively, since the controller was tuned to a faster system, when it is applied to a slower system, the control action will be larger, resulting in overshoot. This can also be seen in Figure 4.31, where the system's response to the extreme cases of parameter variation is shown.

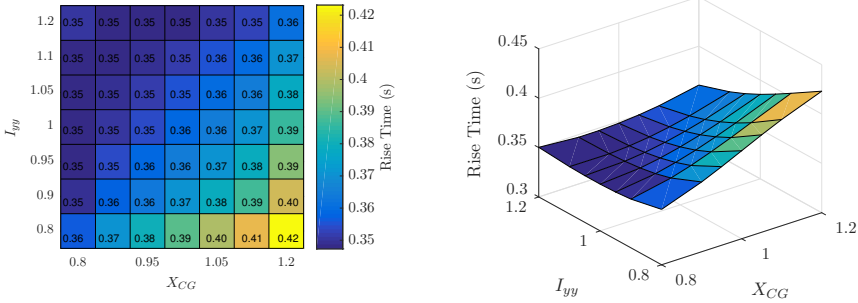
On the other hand, moving the position of the center of gravity towards positive x , means that it will move closer to the nose of the launcher, thus increasing the lever arm, l_{CG} , between the pivot point where the thrust force is applied and the center of gravity. If the lever arm increases, the force necessary to a constant rotational acceleration decreases. Hence, increasing \mathbf{X}_{CG} has the opposite effect of increasing I_{yy} : the system becomes faster. This reasoning is in line with Figure 4.30a: it is clear that, for a fixed I_{yy} ,

the overshoot increases if \mathbf{X}_{CG} decreases, because the system becomes faster. Joining the effect of varying both parameters simultaneously, the overshoot should be maximum if I_{yy} is large and \mathbf{X}_{CG} is small, which can also be seen in Figure 4.30a. Furthermore, one can see that the effect of changing the moment of inertia is predominant. Hence, the overshoot is more sensitive to changes in this parameter than to changes in the location of the center of mass.



(a) Angular velocity response to a step input, for varying I_{yy} and x_{CG} parameters (b) Control signal response to a step input, for varying I_{yy} and x_{CG} parameters

Figure 4.31: System response for a step input, with varying I_{yy} and x_{CG} parameters



(a) Rise Time for varying I_{yy} and x_{CG} simultaneously (b) Rise Time, 3D graph for varying I_{yy} and x_{CG} simultaneously

Figure 4.32: Rise Time to a step input, while simultaneously varying I_{yy} and x_{CG}

Figure 4.32 shows the variation of the rise time with a $\pm 20\%$ deviation of I_{yy} and \mathbf{X}_{CG} around their nominal values. One can see that the trend observed for the rise time is contrary to that observed with for the overshoot. This is in line with what was expected: if there is a large overshoot, then the control action is strong and the system tries to respond quickly, resulting in a smaller rise time and a larger overshoot. It should be noted that the maximum difference between the rise time of all responses tested is

0.07 s, which is small, when compared with the $\pm 20\%$ variation in the parameters.

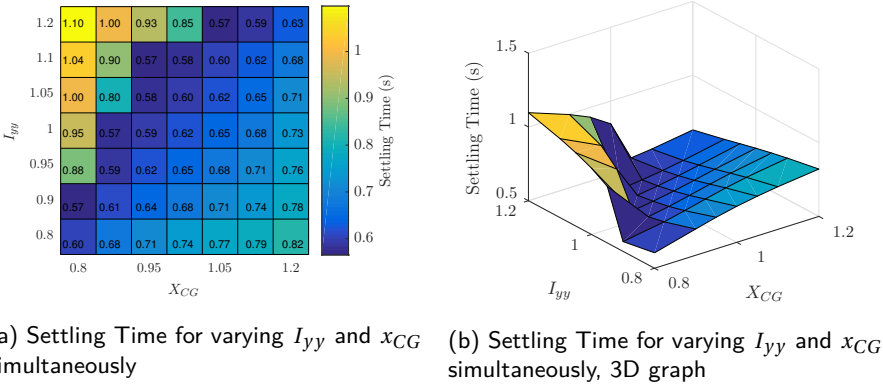


Figure 4.33: Settling Time to a step input, while simultaneously varying I_{yy} and x_{CG}

The settling time as a function of the varying parameters is shown in Figure 4.33. The general trend is in line with the evolution of the overshoot: if the overshoot increases, the settling time also increases, since the transient is longer. Nevertheless, it can be seen that, contrary to the overshoot, the settling time is sensitive to variations in both parameters, while the overshoot was predominantly sensitive to changes in I_{yy} . Furthermore, the effect observed for the independent variation of I_{yy} is also observed here: there is a threshold for which the settling time increases, which is related to the definition of the settling time within 2%, as seen before.

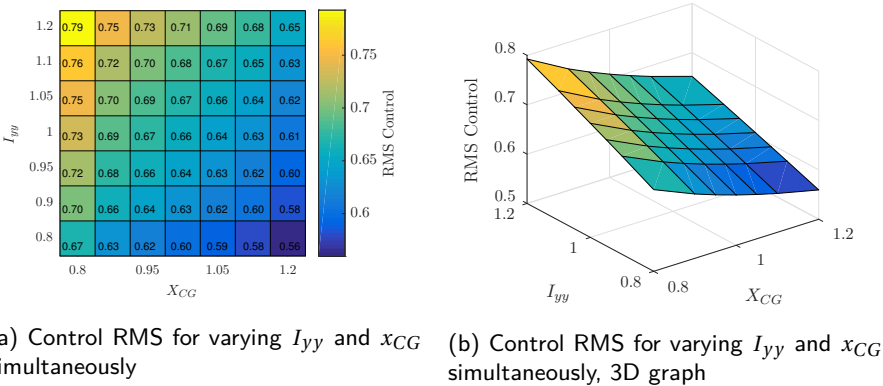
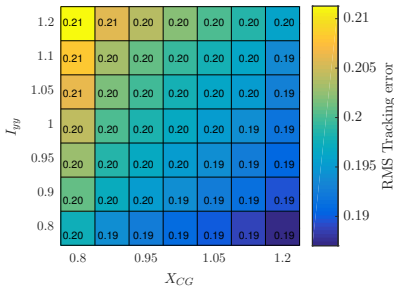
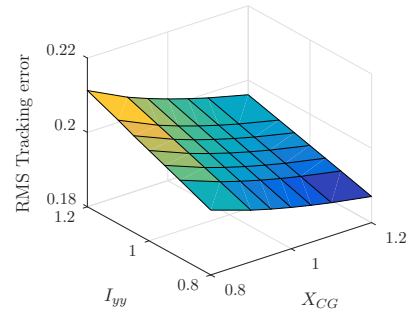


Figure 4.34: Control RMS to a step input, while simultaneously varying I_{yy} and x_{CG}

Figures and 4.34 and 4.35 show the variation of the RMS of the control signal and reference tracking with the variation of the parameters. Both cases follow the trend analysed in the overshoot case, which is in line with what was expected, since, for a larger overshoot, the tracking error and the control action increase and vice-versa. It is important to note that the variation of the tracking error RMS is small, indicating a



(a) Tracking error RMS for varying I_{yy} and x_{CG} simultaneously



(b) Tracking error RMS for varying I_{yy} and x_{CG} simultaneously, 3D graph

4

Figure 4.35: Tracking error RMS to a step input, while simultaneously varying I_{yy} and x_{CG}

good tracking of the reference signal irrespective of the variation of parameters.

It can be concluded that the controller is able to accommodate uncertainty in the system's parameters, both for a single parameter and multiple parameters varying at once, albeit with a degraded performance. Nevertheless, for all the considered cases the controller is able to stabilize the system and track the reference, without exceeding the limits of the actuators, which indicates that the controller is robust to the type of considered uncertainties.

5

NOMINAL NONLINEAR CONTROL DESIGN

In this chapter, the implementation of a nonlinear controller for the launch vehicle will be detailed. Backstepping control design is adopted, as described in the next section. This chapter starts with an introduction to this technique, after which it is applied to the nominal nonlinear system.

5.1. OVERVIEW OF NONLINEAR SYSTEMS THEORY

5.1.1. LYAPUNOV ANALYSIS

Backstepping control hinges on the seminal work of Lyapunov, who laid the foundations for the theory that carries his name. The basic idea of Lyapunov's stability theory is to evaluate the stability of equilibrium points. Consider the system $\dot{\mathbf{x}} = f(\mathbf{x})$. An equilibrium point, \mathbf{x}_{eq} , is a configuration of the state vector where the following condition is satisfied:

$$f(\mathbf{x}_{\text{eq}}) = 0 . \quad (5.1)$$

Equilibrium points can be classified in terms of stability [55]:

- **Stable:** an equilibrium point is stable if for every $\epsilon > 0$ exists a $\delta > 0$ such that:

$$\|\mathbf{x}_0 - \mathbf{x}_{\text{eq}}\| < \delta \Rightarrow \|\mathbf{x}(t, \mathbf{x}_0) - \mathbf{x}_{\text{eq}}\| < \epsilon, \quad \forall t \geq 0$$

- **Asymptotically stable:** an equilibrium point is asymptotically stable, if it is stable and exists $\delta_1 > 0$ such that:

$$\|\mathbf{x}_0 - \mathbf{x}_{\text{eq}}\| < \delta_1 \Rightarrow \lim_{t \rightarrow \infty} \|\mathbf{x}(t, \mathbf{x}_0) - \mathbf{x}_{\text{eq}}\| = 0$$

- **Unstable:** an equilibrium point is unstable if it is not stable.

An equilibrium point which is stable but not asymptotically stable is often called marginally stable.

The stability conditions for an equilibrium point are simple, but its mathematical proof is usually not. Hence, the study of stability of equilibrium points is often done by using Lyapunov Functions. Lyapunov functions are the mathematical representation of a fundamental physical observation: if the total energy of a physical system is continuously dissipated, then it must eventually settle to an equilibrium point. Therefore, by studying the variation of a single scalar quantity, it is possible to determine the stability of equilibrium points. Lyapunov's direct method uses generalized "energy-like" scalar functions, that depend on the system state. By examining the time variation of such functions, it is usually possible to gain insight on the stability of the system [55].

A Lyapunov function, $V(\mathbf{x})$, is defined as a function with the following properties:

- $V(\mathbf{x}) : D \subset \mathbb{R}^n \rightarrow \mathbb{R}$ is a continuous scalar function of the state;
- $V(0) = 0$;
- $V(\mathbf{x}) > 0, \forall \mathbf{x} \in D \setminus \{0\}$.

The last condition is that of a **positive-definite** function. If a function satisfies the weaker condition $V(\mathbf{x}) \geq 0$ for $\mathbf{x} \neq 0$, it is said to be positive semidefinite. A function is said to be negative or negative semidefinite if $-V(x)$ is positive definite or positive semidefinite, respectively [55].

Lyapunov functions can be used to prove stability using the Lyapunov stability theorem for Autonomous Systems:

Theorem (from [55]): Let $\bar{\mathbf{x}}$ be an equilibrium point of the autonomous system $\dot{\mathbf{x}} = f(\mathbf{x})$ and let $V(\mathbf{x}) : D \subset \mathbb{R}^n \rightarrow \mathbb{R}$ be a Lyapunov function on the domain D around the origin. Then, $\bar{\mathbf{x}} = 0$ is:

- Stable if $\dot{V}(\mathbf{x}) \leq 0$, except at $x = 0$;
- Asymptotically stable if $\dot{V}(\mathbf{x}) < 0$ along the trajectories of the system, except at $x = 0$.

The existence of a Lyapunov function is a **sufficient condition** to prove stability or asymptotic stability of an equilibrium point. However, if no Lyapunov function that verifies the conditions of the theorem is found, it does not imply that the equilibrium point is unstable. Using the terminology introduced earlier, Lyapunov's theorem can be stated as: the origin of an autonomous system is stable if there is a continuously differentiable positive definite function $V(\mathbf{x})$ so that $\dot{V}(\mathbf{x})$ is negative semidefinite, and it is asymptotically stable if $\dot{V}(\mathbf{x})$ is negative definite [55].

There are many different results derived from Lyapunov's theorem that permit to drop some of the restrictions of the original theorem. The literature in this topic is extensive and the reader is referred to [55] for an in-depth treatment of this topic. However, the concepts of boundedness, ultimate boundedness and input-to-state stability will be useful in the analysis of the designed nonlinear controller and thus are introduced here.

Consider a nonlinear system

$$\dot{\mathbf{x}} = f(t, \mathbf{x}), \quad (5.2)$$

where $f: [0, \infty) \times D \rightarrow \mathbb{R}^n$ is piecewise continuous in t and locally Lipschitz in \mathbf{x} on $[0, \infty)$, and $D \subset \mathbb{R}^n$ is a domain that contains the origin. The solutions of (5.2) are:

- uniformly bounded if there exists a positive constant c , independent of $t_0 > 0$, and for every $a \in (0, c)$, there is $\beta = \beta(a) > 0$, independent of t_0 , such that

$$\|\mathbf{x}(t_0)\| \leq a \Rightarrow \|\mathbf{x}(t)\| \leq \beta, \quad \forall t \geq t_0. \quad (5.3)$$

- globally uniformly bounded if (5.3) holds for arbitrarily large a
- uniformly ultimately bounded with ultimate bound b , if there exists positive constants b and c , independent of $t_0 \geq 0$, and for every $a \in (0, c)$, there is $T = T(a, b) \geq 0$, independent of t_0 , such that

$$\|\mathbf{x}(t_0)\| \leq a \Rightarrow \|\mathbf{x}(t)\| \leq b, \quad \forall t > t_0 + T. \quad (5.4)$$

- globally uniformly ultimately bounded if (5.4) holds for arbitrarily large a .

The nonlinear system in Eq. (5.2) is said to be input-to-state stable if there exists a class \mathcal{KL} function β and a class \mathcal{K} function γ such that for any initial state $\mathbf{x}(t_0)$ and any bounded input $\mathbf{u}(t)$, the solution $\mathbf{x}(t)$ exists for all $t > t_0$ and satisfies

$$\|\mathbf{x}(t)\| \leq \beta(\|\mathbf{x}(t_0)\|, t - t_0) + \gamma\left(\sup_{t_0 \leq \tau \leq t} \|\mathbf{u}(\tau)\|\right). \quad (5.5)$$

The previous inequality guarantees that for any bounded input $\mathbf{u}(t)$, the state $\mathbf{x}(t)$ will be bounded [55].

A sufficient condition for input-to-state stability is given by the following theorem:

Theorem (from [55]): Let $V: [0, \infty) \times \mathbb{R} \rightarrow \mathbb{R}$ be a continuously differentiable function such that

$$\begin{aligned} \alpha_1(\|\mathbf{x}\|) \leq V(t, \mathbf{x}) \leq \alpha_2(\|\mathbf{x}\|) \\ \frac{\partial V}{\partial t} + \frac{\partial V}{\partial \mathbf{x}} f(t, \mathbf{x}, \mathbf{u}) \leq -W_3(\mathbf{x}), \quad \forall \|\mathbf{x}\| \geq \rho(\|\mathbf{u}\|) > 0, \end{aligned} \quad (5.6)$$

$\forall (t, \mathbf{x}, \mathbf{u}) \in [0, \infty) \times \mathbb{R}^n \times \mathbb{R}^m$, where α_1, α_2 are class \mathcal{K}_∞ functions, ρ is a class \mathcal{K} function, and $W_3(\mathbf{x})$ is a continuous positive definite function on \mathbb{R}^n . Then, the system defined in Eq. (5.2) is input-to-state stable with $\gamma = \alpha_1^{-1} \circ \alpha_2 \circ \rho$.

5.1.2. NONLINEAR BACKSTEPPING

Nonlinear backstepping began to be used in the late 1980s. It is a recursive design technique developed for the stabilization of strict-feedback nonlinear systems. Adaptive backstepping allows to use some nonlinearities of the system (such as nonlinear damping) in the control design by recursively considering states of the system as virtual inputs for higher-order systems. Formally for a strict feedback system with M states [55]:

$$\begin{aligned}
\dot{\mathbf{x}} &= f_0(\mathbf{x}) + h_0(\mathbf{x})\eta_1 \\
\dot{\eta}_1 &= f_1(\mathbf{x}, \eta_1) + h_1(\mathbf{x}, \eta_1)\eta_2 \\
\dot{\eta}_2 &= f_2(\mathbf{x}, \eta_1, \eta_2) + h_2(\mathbf{x}, \eta_1, \eta_2)\eta_3 \\
&\vdots \\
\dot{\eta}_{M-1} &= f_{M-1}(\mathbf{x}, \eta_1, \dots, \eta_{M-1}) + h_{M-1}(\mathbf{x}, \eta_1, \dots, \eta_{M-1})\eta_M \\
\dot{\eta}_M &= f_M(\mathbf{x}, \eta_1, \dots, \eta_M) + h_M(\mathbf{x}, \eta_1, \dots, \eta_M)u,
\end{aligned} \tag{5.7}$$

where $\mathbf{x} \in \mathbb{R}^n$, η_1 to η_M are scalars and f_0 to f_M vanish at the origin. Systems like this one are referred to as strict-feedback systems because the nonlinearities f_i and h_i in the $\dot{\eta}_i$ equation ($i = 1, \dots, M$) depend only on $\mathbf{x}, \eta_1, \dots, \eta_M$; that is, only on the state variables that are fed back. To illustrate the backstepping procedure, let's examine the simplest instance of (5.7), for which $M=1$. It is given by [55]:

$$\begin{aligned}
\dot{\mathbf{x}} &= f_0(\mathbf{x}) + h_0(\mathbf{x})\eta_1 \\
\dot{\eta}_1 &= u,
\end{aligned} \tag{5.8}$$

where $u = \eta_2$, $f_1(\mathbf{x}, \eta_1) = 0$ and $h_1(\mathbf{x}, \eta_1) = 1$. Assume that there is a Lyapunov function $V_0(\mathbf{x})$, through which we prove that the control η_1 stabilizes the \mathbf{x} dynamics. Assume also that $f_0 \rightarrow 0$ as time goes to infinity. The goal is to stabilize \mathbf{x} using control u . However, this control is not directly available in the equation of \mathbf{x} . Nonetheless, the dynamics of η_1 can be controlled and with it is possible to control the dynamics of \mathbf{x} . Taking η_1 as the virtual control input (as seen from \mathbf{x}) it is possible to design a state feedback control law, $\eta_1 = \phi(\mathbf{x})$ with $\phi(0) = 0$ and a Lyapunov function $V_0(\mathbf{x})$ that stabilizes the system. This is the basic idea behind backstepping and the starting point for its application. To guarantee stability, $V_0(\mathbf{x})$ must verify

$$\dot{V}_0(\mathbf{x}) = \frac{\partial V_0}{\partial \mathbf{x}} [f_0(\mathbf{x}) + h_0(\mathbf{x})\phi(\mathbf{x})] \leq -W(\mathbf{x}), \tag{5.9}$$

over the domain of interest for some positive definite function $W(\mathbf{x})$. The first step of the backstepping procedure is to rearrange the system in terms of the error variable $z = \eta_1 - \phi$, which is the control error. To express (5.8) in terms of z , add and subtract $h_0(\mathbf{x})\phi$ from (5.8) and rearrange, obtaining:

$$\begin{aligned}
\dot{\mathbf{x}} &= f_0(\mathbf{x}) + h_0(\mathbf{x})\phi + h_0(\mathbf{x})z \\
\dot{z} &= \eta_1 - \dot{\phi} = u - \dot{\phi}.
\end{aligned} \tag{5.10}$$

Defining a new variable $v = u - \dot{\phi}$, then (5.10) can be written as:

$$\begin{aligned}
\dot{\mathbf{x}} &= f_0(\mathbf{x}) + h_0(\mathbf{x})\phi + h_0(\mathbf{x})z \\
\dot{z} &= v.
\end{aligned} \tag{5.11}$$

Now the new system defined in (5.10) defines the original system (5.8) in terms of the virtual control error z and control v . To find v , the initial Lyapunov function is extended as follows:

$$V_1(\mathbf{x}, z) = V_0(\mathbf{x}) + \frac{1}{2}z^2. \quad (5.12)$$

The new function is also a Lyapunov function because it is the sum of two positive semidefinite functions. Taking the time derivative of (5.12):

$$\dot{V}_1(\mathbf{x}, z) = \dot{V}_0(\mathbf{x}) + z\dot{z}. \quad (5.13)$$

Substituting $\eta_1 = z + \phi$ for any instances of η_1 that may appear in $\dot{V}_0(\mathbf{x})$ and v for \dot{z} yields:

$$\dot{V}_1(\mathbf{x}, z) = \dot{V}_0(\mathbf{x}) + zv \leq -W(\mathbf{x}) + z(h_0(\mathbf{x})\mathbf{x} + v). \quad (5.14)$$

Now the control v can be chosen to achieve negative definiteness in (5.14), thus achieving stability. If $M > 2$, the backstepping procedure is applied recursively culminating in the final control law that contains u .

Backstepping can be modified in order to achieve reference tracking, rewriting the dynamics of the system in terms of the reference tracking error, $\tilde{r} = r_d - r$, defined as the difference between the desired and actual position. In this case, the final control law is a function of the input and the $M-1$ derivatives of the reference signal: $v = f(\tilde{r}, \dot{\tilde{r}}, \dots, D_{M-1}(\tilde{r}), u)$, where $D_{M-1}(\tilde{r}) = \frac{d\tilde{r}}{dt}$. However this is usually not a problem, because the reference signal is known beforehand and its derivatives can be computed offline. Having defined the nonlinear backstepping design procedure, it can now be applied to the launcher.

5.2. APPLICATION OF NONLINEAR BACKSTEPPING TO THE LAUNCH VEHICLE

The control objective defined in Chapter 2 is to follow a reference trajectory expressed through Euler angles, hence to ensure that $\boldsymbol{\lambda} \rightarrow \boldsymbol{\lambda}_d$. Equivalently, this can be written in terms of the reference tracking error, $\tilde{\boldsymbol{\lambda}} = \boldsymbol{\lambda} - \boldsymbol{\lambda}_d$, with the objective $\tilde{\boldsymbol{\lambda}} \rightarrow 0$.

As seen before, there is no angular actuation along the launcher's x -axis, during the part of the trajectory considered. Hence, the roll angle cannot be controlled. Thus, the control objective can be defined as a function of the two controllable angles: the yaw and the pitch angles. Defining the controllable angles as $\boldsymbol{\lambda}_c = [\theta \ \psi]^T$, the control objective can be stated as $\tilde{\boldsymbol{\lambda}}_c \rightarrow 0$. Likewise, the desired angular velocity is defined as $\boldsymbol{\omega}_c = [q \ r]^T$.

From the structure of the Euler angles equations, Eq. (2.7), it can be seen that there is no explicit dependence on the input variables. The Euler angles depend on the angular velocity vector, which in turn contain a term that depends on the input. Noting that in the nominal system $\dot{p} = 0$, the cross-coupling terms from the cross product $\boldsymbol{\omega}_c \times I\boldsymbol{\omega}_c$ are zero. Hence, the system dynamics can be written as:

$$\begin{cases} \dot{\boldsymbol{\lambda}}_c &= f_0(\phi, \theta) \cdot \boldsymbol{\omega}_c \\ \dot{\boldsymbol{\omega}}_c &= I_c^{-1}(A + Bu). \end{cases} \quad (5.15)$$

Cases where $\dot{p} \neq 0$ will be considered as a perturbation to the nominal model and will be addressed in Chapter 6. The matrices A and B are derived from ΣM_{ext} in Eq. (2.21) using the fact that there is symmetry in the control input term, associated with the moment generated by the TVC system. Defining $c_1 = \frac{\sqrt{2}}{2} T l_{CG}$, $u_q = c \delta_y s \delta_p - s \delta_y$, $u_r = c \delta_y s \delta_p + s \delta_y$, $A_q = (Dc\beta s\alpha + Ls\beta s\alpha) l_{GA}$ and $A_r = (Lc\beta - Ds\beta) l_{GA}$:

$$\Sigma \mathbf{M}_{\text{ext}} = \begin{bmatrix} \frac{\sqrt{2}}{2} T l_{CG} (c \delta_y s \delta_p - s \delta_y) + (Dc\beta s\alpha + Ls\beta s\alpha) l_{GA} \\ -\frac{\sqrt{2}}{2} T l_{CG} (c \delta_y s \delta_p + s \delta_y) + (Lc\beta - Ds\beta) l_{GA} \end{bmatrix} = \begin{bmatrix} c_1 \cdot u_q + A_q \\ -c_1 \cdot u_r + A_r \end{bmatrix}. \quad (5.16)$$

Rewriting in matrix form:

$$\Sigma \mathbf{M}_{\text{ext}} = A + B\mathbf{u}, \text{ with } \mathbf{A} = \begin{bmatrix} A_q \\ A_r \end{bmatrix}, \mathbf{B} = \begin{bmatrix} c_1 & 0 \\ 0 & -c_1 \end{bmatrix}, \mathbf{u} = \begin{bmatrix} u_q \\ u_r \end{bmatrix}. \quad (5.17)$$

Before continuing, an explicit relation between \mathbf{u} and (δ_p, δ_y) must be found. From the definition of \mathbf{u} :

$$\begin{cases} u_q = \underbrace{c \delta_y s \delta_p}_{u_1} - \underbrace{s \delta_y}_{u_2} = u_1 - u_2 \\ u_r = \underbrace{c \delta_y s \delta_p}_{u_1} + \underbrace{s \delta_y}_{u_2} = u_1 + u_2. \end{cases} \quad (5.18)$$

Now, rewriting u_1 and u_2 in terms of u_q and u_r :

$$\begin{cases} u_1 = \frac{u_q + u_r}{2} \\ u_2 = \frac{u_r - u_q}{2}. \end{cases} \quad (5.19)$$

Finally, and using the relation between (u_1, u_2) and (δ_p, δ_y) :

$$\begin{cases} \delta_y = \arcsin(u_2) \\ \delta_p = \arcsin\left(\frac{u_1}{\cos \delta_y}\right). \end{cases} \quad (5.20)$$

Hence, using eqs. (5.19) and (5.20) the control inputs (u_q, u_r) can be transformed into the actual TVC deflections (δ_p, δ_y) . Obviously, Eq. (5.20) introduces constraints in the possible values of (δ_p, δ_y) due to the arcsin. However, the arcsin is defined in $[-\pi/2, \pi/2]$ and the actuator limits the maximum deflection of the TVC angles to $\pm 6.5^\circ$, which is more limiting to the performance of the system. When choosing the gains of the designed controller one must be careful not to exceed these limits.

The controlled Euler angles error dynamics is defined as

$$\dot{\tilde{\lambda}}_c = \dot{\lambda}_c - \dot{\lambda}_{c_d} = f_0(\phi, \theta) \omega_c - \dot{\lambda}_{c_d}. \quad (5.21)$$

Regarding the controlled angular velocity, ω_c as the control input for the $\dot{\tilde{\lambda}}_c$ system, the desired control can be defined as:

$$\omega_{c_d} = \alpha(\lambda_c, \lambda_{c_d}, \dot{\lambda}_{c_d}) . \quad (5.22)$$

It is possible to define a Lyapunov function using the Euler angles error to assess the stability of the system:

$$V_1(\tilde{\lambda}_c) = \frac{1}{2} \tilde{\lambda}_c^T \tilde{\lambda}_c . \quad (5.23)$$

To guarantee stability, the Lyapunov function must be positive definite and its derivative must be negative definite. Checking the requirement of positive-definiteness for V_1 :

- $V_1(\tilde{\lambda}_c = 0) = 0$;
- $V_1(\tilde{\lambda}_c) > 0 \forall \tilde{\lambda}_c \neq 0$, because V_1 is a quadratic function.

Hence the requirements for considering $V_1(\tilde{\lambda}_c)$ a Lyapunov function are fulfilled. The derivative of the Lyapunov function, Eq. (5.23) is

$$\dot{V}_1(\tilde{\lambda}_c) = \tilde{\lambda}_c^T \dot{\tilde{\lambda}}_c = \tilde{\lambda}_c^T [f_0(\phi, \theta) \omega_c - \dot{\lambda}_{c_d}] . \quad (5.24)$$

Now, substituting (5.22) to (5.24), yields:

$$\dot{V}_1(\tilde{\lambda}_c) = \tilde{\lambda}_c^T [f_0(\phi, \theta) \alpha(\lambda_c, \lambda_{c_d}, \dot{\lambda}_{c_d}) - \dot{\lambda}_{c_d}] \leq -W_1(\tilde{\lambda}_c) . \quad (5.25)$$

Choosing α such that $\dot{V}_1(\tilde{\lambda}_c) \leq -W_1(\tilde{\lambda}_c)$, where $W_1(\tilde{\lambda}_c)$ is a positive definite function of the reference tracking error, guarantees stability.

From (5.25), a suitable choice for α can be obtained, provided that $f_0(\phi, \theta)$ is invertible. Choosing $\alpha(\lambda_c, \lambda_{c_d}, \dot{\lambda}_{c_d}) = -f_0(\lambda_c)^{-1} (K_{\text{ang}} \tilde{\lambda}_c - \dot{\lambda}_{c_d})$, yields

$$\dot{V}_1(\tilde{\lambda}_c) = -\tilde{\lambda}_c^T K_{\text{ang}} \tilde{\lambda}_c < 0, \quad \forall K_{\text{ang}} > 0 , \quad (5.26)$$

where K_{ang} is a positive-definite diagonal gain matrix associated with the Euler angles that stabilizes the system.

The matrix $f_0(\phi, \theta)$ is well known in the aerospace community as it describes the Euler angles dynamics. This matrix is invertible and its inverse is readily available in the literature [41]. Given that only the pitch and heading angles can be controlled, the part related with the roll angle can be disregarded. Hence, $f_0(\phi, \theta)$ is defined as:

$$f_0(\phi, \theta) = \begin{bmatrix} \cos \phi & -\sin \phi \\ \sin \phi / \cos \theta & \cos \phi / \cos \theta \end{bmatrix}, \quad f_0(\phi, \theta)^{-1} = \begin{bmatrix} \cos \phi & \sin \phi \cos \theta \\ -\sin \phi & \cos \phi \cos \theta \end{bmatrix} \quad (5.27)$$

Now, defining the angular velocity error as $\tilde{\omega}_c = \omega_c - \omega_{c_d}$, where ω_{c_d} is the desired angular velocity, the original system can be rewritten in terms of the tracking and angular velocity errors:

$$\begin{cases} \dot{\tilde{\lambda}}_c = f_0(\phi, \theta) \tilde{\omega}_c + \alpha(\lambda_c, \lambda_{c_d}, \dot{\lambda}_{c_d}) - \dot{\lambda}_{c_d} \\ \dot{\tilde{\omega}}_c = \dot{\omega}_c - \dot{\omega}_{c_d} \end{cases} = \begin{cases} \dot{\tilde{\lambda}}_c = f_0(\phi, \theta) \tilde{\omega}_c - K_{\text{ang}} \tilde{\lambda}_c \\ \dot{\tilde{\omega}}_c = I_c^{-1} (A + Bu) - \dot{\alpha}(\lambda_c, \lambda_{c_d}, \dot{\lambda}_{c_d}) . \end{cases} \quad (5.28)$$

The derivative is defined as

$$\dot{\alpha}(\lambda_c, \lambda_{c_d}, \dot{\lambda}_{c_d}) = \dot{\omega}_{c_d} = \frac{d}{dt} f_0^{-1}(\phi(t), \theta(t)) \cdot (K_{\text{ang}} \tilde{\lambda}_c - \dot{\lambda}_{c_d}) - f_0^{-1}(\phi(t), \theta(t)) \cdot \frac{d}{dt} (K_{\text{ang}} \tilde{\lambda}_c - \dot{\lambda}_{c_d}) . \quad (5.29)$$

The first parcel can be written as a function of Euler angles and angular velocities:

$$\begin{aligned} \frac{d}{dt} f_0^{-1}(\phi(t), \theta(t)) &= \begin{bmatrix} \frac{\partial c\phi}{\partial \phi} \dot{\phi} & \frac{\partial s\phi c\theta}{\partial \phi} \dot{\phi} + \frac{\partial s\phi c\theta}{\partial \theta} \dot{\theta} \\ -\frac{\partial s\phi}{\partial \phi} \dot{\phi} & \frac{\partial c\phi c\theta}{\partial \phi} \dot{\phi} + \frac{\partial c\phi c\theta}{\partial \theta} \dot{\theta} \end{bmatrix} \\ &= \begin{bmatrix} -s\phi & c\phi c\theta \\ -c\phi & -s\phi c\theta \end{bmatrix} \dot{\phi} + \begin{bmatrix} 0 & -s\phi s\theta \\ 0 & -c\phi s\theta \end{bmatrix} \dot{\theta} = F(\phi, \theta, \dot{\phi}, \dot{\theta}) . \end{aligned} \quad (5.30)$$

Substituting the expression of $\dot{\phi}$ and $\dot{\theta}$ (Eq. (2.6)) in the previous equation, it is possible to write this parcel exclusively as function of the state variables (ϕ, θ, q, r) , yielding:

5

$$F(\phi, \theta, q, r) = \begin{bmatrix} -s^2\phi t\theta & 0 \\ -c\phi s\phi t\theta & -s\theta \end{bmatrix} q + \begin{bmatrix} -s\phi c\phi t\theta & s\theta \\ -c^2\phi t\theta & 0 \end{bmatrix} r . \quad (5.31)$$

The second parcel of eq. (5.29) yields:

$$-f_0^{-1}(\phi(t), \theta(t)) \cdot \frac{d}{dt} (K_{\text{ang}} \tilde{\lambda}_c - \dot{\lambda}_{c_d}) = f_0(\lambda)^{-1} (\ddot{\lambda}_{c_d} - K_{\text{ang}} \dot{\lambda}_{c_d}) . \quad (5.32)$$

Hence,

$$\dot{\omega}_{c_d} = F(\phi, \theta, q, r) (K_{\text{ang}} \tilde{\lambda}_c - \dot{\lambda}_{c_d}) + f_0^{-1} (\ddot{\lambda}_{c_d} - K_{\text{ang}} \dot{\lambda}_{c_d}) . \quad (5.33)$$

Now, a composite Lyapunov function for the whole system can be defined as:

$$V_2(\tilde{\lambda}_c, \tilde{\omega}_c) = V_1(\tilde{\lambda}_c) + \frac{1}{2} \tilde{\omega}_c^T \tilde{\omega}_c . \quad (5.34)$$

This new function also satisfies the conditions for being considered a Lyapunov function and its time-derivative is given by

$$\begin{aligned} \dot{V}_2(\tilde{\lambda}_c, \tilde{\omega}_c) &= \tilde{\lambda}_c^T \dot{\tilde{\lambda}}_c + \tilde{\omega}_c^T \dot{\tilde{\omega}}_c \\ &= \tilde{\lambda}_c^T [f_0(\phi, \theta) \tilde{\omega}_c - K_{\text{ang}} \tilde{\lambda}_c] + \tilde{\omega}_c^T I_c^{-1} [A + BU - I_c \dot{\omega}_{c_d}] \\ &= -\tilde{\lambda}_c^T K_{\text{ang}} \tilde{\lambda}_c + \tilde{\omega}_c^T I_c^{-1} [I_c f_0(\phi, \theta)^T \tilde{\lambda}_c + A + Bu - I_c \dot{\omega}_{c_d}] . \end{aligned} \quad (5.35)$$

Finally, choosing u such that the derivative of the Lyapunov function, $\dot{V}_2(\tilde{\lambda}, \tilde{\omega})$, is negative definite, stability for the whole system is guaranteed. Choosing

$$u = -B^{-1} (I_c f_0(\phi, \theta)^T \tilde{\lambda}_c + A + I_c (K_{\omega} \tilde{\omega}_c - \dot{\omega}_{c_d})) , \quad (5.36)$$

then the derivative of the Lyapunov function becomes

$$\dot{V}_2(\tilde{\lambda}_c, \tilde{\omega}_c) = -\tilde{\lambda}_c^T K_{\text{ang}} \tilde{\lambda}_c - \tilde{\omega}_c^T K_w \tilde{\omega}_c < 0, \quad \forall K_{\text{ang}} > 0, K_w > 0. \quad (5.37)$$

There are two gain matrices, K_{ang} and K_w that can be adjusted to tune the controller response. Furthermore, for the nominal system, it arises from the Lyapunov stability analysis that the only requirement to ensure stability is that both gain matrices are positive-definite. Matrix B is invertible because it is a real diagonal matrix and its inverse is given by

$$B^{-1} = \begin{bmatrix} 1/c_1 & 0 \\ 0 & -1/c_1 \end{bmatrix}. \quad (5.38)$$

The control law described by Eq. (5.36) stabilizes the system in nominal conditions. Finally, the closed-loop state equation can be written, using the definition $\tilde{\mathbf{x}} = [\tilde{\lambda}_c \ \tilde{\omega}_c]^T$:

$$\dot{\tilde{\mathbf{x}}} = \begin{bmatrix} \dot{\tilde{\lambda}}_c \\ \dot{\tilde{\omega}}_c \end{bmatrix} = - \begin{bmatrix} K_{\text{ang}} & 0 \\ 0 & K_w \end{bmatrix} \tilde{\mathbf{x}} + \begin{bmatrix} 0 & f_0(\phi, \theta) \\ -f_0(\phi, \theta) & 0 \end{bmatrix} \tilde{\mathbf{x}}, \quad (5.39)$$

where it is clear that, regarding the second state as the control input for the first state, the nonlinear part associated with the Euler angles is cancelled and the dynamics of the system is then similar to first order integrators.

Next, procedures for tuning the gains and relations between different parameter uncertainty and the region of convergence of the solution will be studied.

6

ROBUSTNESS ANALYSIS OF THE NONLINEAR CONTROLLER

In the previous chapter, a control law for trajectory tracking using nonlinear backstepping control was developed. The dynamics of the system were written in terms of the error variables $\tilde{\lambda}_c$ and $\tilde{\omega}_c$ and a controller to minimize the reference tracking error was derived.

Building upon previous results, this chapter is devoted to establishing relations between the parameters of the controller and its ability to reject different types of disturbances that can affect the system. The analysis will be carried on by modelling a particular disturbance and by using a Lyapunov function to derive the tradeoffs between gains, magnitude of the errors, and parameters of the system. In order to follow a general approach that can be applied to a wide range of launch vehicles, an effort is made to obtain relations that are independent of the rocket's trajectory.

In the following subsections, the impact of different types of disturbances on the system will be examined individually, starting with bounded roll-rate disturbances.

6.1. ROBUSTNESS TO BOUNDED ROLL-RATE DISTURBANCES

In chapter 2, it was seen that no commanded forces generate roll moments, at least nominally. Furthermore, given that $I_{yy} = I_{zz}$, the dynamics of the roll-rate were established as $\dot{p} = 0$. The nominal backstepping controller derived in the previous chapter, considered that the roll-rate is null. However, unmodelled aerodynamic forces and cross winds can generate forces along the x-axis, inducing a roll moment. Henceforth, the influence of a bounded roll rate in the stability of the system is studied. As discussed earlier, at this stage of the mission, the roll-rate of the rocket is not actively controlled. However, there is a roll-rate limiter that actuates if $|p| > 45 \text{ } \ddot{z}^\circ/\text{s}$. [32, 35, 56]. Therefore, the system must be stable for perturbations up to this value. If $|p| > 45 \text{ } ^\circ/\text{s}$, it is assumed that the RACS will fire auxiliary thrusters and reduce the roll-rate.

To analyse this disturbance, consider p as a perturbation to the state vector. Using the notation introduced in the previous chapter, the dynamics of the controlled angular

velocity, in the presence of a bounded roll-rate, is given by:

$$\begin{cases} \dot{q} = \frac{1}{I_{yy}} (A_q + c_1 u_q - (I_{xx} - I_{zz}) p r) \\ \dot{r} = \frac{1}{I_{zz}} (A_r - c_1 u_q - (I_{xx} - I_{yy}) p q) . \end{cases} \quad (6.1)$$

Rewriting the error dynamics of the controlled angular velocity in matrix form:

$$\dot{\omega}_c = I_c^{-1} (A + B u + P \omega_c) - \dot{\omega}_{c_d}, \quad (6.2)$$

where A and B have the same definition as in the previous chapter, (Eq. (5.17)), and P is the disturbance to the state introduced by the non-null roll-rate:

$$P = \begin{bmatrix} 0 & (I_{zz} - I_{xx}) p \\ (I_{yy} - I_{xx}) p & 0 \end{bmatrix},$$

Now using Eq. (6.2) and the nominal backstepping controller, the derivative of the Lyapunov function can be reformulated. Building on the previous results and using the relation $\omega_c = \tilde{\omega}_c + \omega_{c_d}$:

$$\dot{V}_2(\tilde{\lambda}_c, \tilde{\omega}_c) = -\tilde{\lambda}_c^T K_{\text{ang}} \tilde{\lambda}_c - \tilde{\omega}_c^T I_c^{-1} [I_c f_0(\phi, \theta) + A + B u - I_c \dot{\omega}_{c_d} + P \tilde{\omega}_c + P \omega_{c_d}] . \quad (6.3)$$

Substituting the nominal control, $u = -B^{-1} (I_c f_0(\phi, \theta) + A + I_c (K_w \tilde{\omega}_c - \dot{\omega}_{c_d}))$:

$$\begin{aligned} \dot{V}_2(\tilde{\lambda}_c, \tilde{\omega}_c) &= -\tilde{\lambda}_c^T K_{\text{ang}} \tilde{\lambda}_c - \tilde{\omega}_c^T I_c^{-1} [-I_c (K_w + I_c^{-1} P) \tilde{\omega}_c + P \omega_{c_d}] \\ &= -\tilde{\lambda}_c^T K_{\text{ang}} \tilde{\lambda}_c - \tilde{\omega}_c^T (K_w + I_c^{-1} P) \tilde{\omega}_c + \tilde{\omega}_c^T I_c^{-1} P \omega_{c_d} . \end{aligned} \quad (6.4)$$

By using $\omega_{c_d} = -f_0^{-1} (K_{\text{ang}} \tilde{\lambda}_c - \dot{\lambda}_{c_d})$, it follows that:

$$\dot{V}_2(\tilde{\lambda}_c, \tilde{\omega}_c) = -\tilde{\lambda}_c^T K_{\text{ang}} \tilde{\lambda}_c - \tilde{\omega}_c^T (K_w - I_c^{-1} P) \tilde{\omega}_c - \tilde{\omega}_c^T I_c^{-1} P f_0^{-1} K_{\text{ang}} \tilde{\lambda}_c + \tilde{\omega}_c^T I_c^{-1} P f_0^{-1} \dot{\lambda}_{c_d} . \quad (6.5)$$

The first term is negative definite by construction, because $K_{\text{ang}} > 0$. The second term is negative definite if $K_w - I_c^{-1} P > 0$. The third term is a cross term between $\tilde{\lambda}_c$ and $\tilde{\omega}_c$, so using Young's inequality ($\mathbf{x}^T \mathbf{y} < \frac{1}{2} \mathbf{x}^T \mathbf{x} + \frac{1}{2} \mathbf{y}^T \mathbf{y}$) it can be written as:

$$\begin{aligned} \underbrace{\tilde{\omega}_c^T I_c^{-1} P f_0^{-1} K_{\text{ang}}}_{\mathbf{x}^T} \underbrace{\tilde{\lambda}_c}_{\mathbf{y}} &< \frac{1}{2} \left(\tilde{\omega}_c^T I_c^{-1} P f_0^{-1} K_{\text{ang}} (\tilde{\omega}_c^T I_c^{-1} P f_0^{-1} K_{\text{ang}})^T + \tilde{\lambda}_c^T \tilde{\lambda}_c \right) \\ &= \frac{1}{2} \left(\tilde{\omega}_c^T I_c^{-1} P f_0^{-1} K_{\text{ang}} \underbrace{K_{\text{ang}}^T f_0^{-T} (I_c^{-1} P)^T}_T \tilde{\omega}_c + \tilde{\lambda}_c^T \tilde{\lambda}_c \right) \\ \Rightarrow \tilde{\omega}_c^T I_c^{-1} P f_0^{-1} K_{\text{ang}} \tilde{\lambda}_c &< \frac{1}{2} \tilde{\omega}_c^T T \tilde{\omega}_c + \frac{1}{2} \tilde{\lambda}_c^T \tilde{\lambda}_c . \end{aligned} \quad (6.6)$$

Substituting the previous result in Eq. (6.5) and collecting terms:

$$\dot{V}_2(\tilde{\lambda}_c, \tilde{\omega}_c) < -\tilde{\lambda}_c^T \left(K_{\text{ang}} - \frac{1}{2}I \right) \tilde{\lambda}_c - \tilde{\omega}_c^T \left(K_w - P - \frac{1}{2}T \right) \tilde{\lambda}_c + \tilde{\omega}_c^T I_c^{-1} P f_0^{-1} \dot{\lambda}_{c_d} \quad (6.7)$$

The previous equation can be written in a more condensed form, using the definition $\tilde{\mathbf{x}} = [\tilde{\lambda}_c \ \tilde{\omega}_c]^T$:

$$\dot{V}_2(\tilde{\mathbf{x}}) < -\tilde{\mathbf{x}}^T M \tilde{\mathbf{x}} + \tilde{\mathbf{x}}^T N \dot{\lambda}_{c_d}, \quad (6.8)$$

$$\text{where } M = \begin{bmatrix} K_{\text{ang}} - \frac{1}{2}I & \mathbf{0} \\ \mathbf{0} & K_w - I_c^{-1}P - \frac{1}{2}T \end{bmatrix}, \quad N = \begin{bmatrix} \mathbf{0} \\ I_c^{-1}P \end{bmatrix}.$$

From Eq. (6.8), it can be concluded that the system is input-to-state stable, meaning that for any bounded input (in this case $\dot{\lambda}_{c_d}$), the norm of $\tilde{\mathbf{x}}$ will be bounded. The system is input-to-state stable because it verifies the conditions of Theorem 5.6. To show that this is the case, the conditions for having $\dot{V}_2 < 0$ must be determined. Hence,

$$\begin{aligned} -\tilde{\mathbf{x}}^T M \tilde{\mathbf{x}} + \tilde{\mathbf{x}}^T N \dot{\lambda}_{c_d} &< 0 \\ \tilde{\mathbf{x}}^T M \tilde{\mathbf{x}} &> \tilde{\mathbf{x}}^T N \dot{\lambda}_{c_d} \end{aligned} \quad (6.9)$$

For a positive-definite matrix M , the Rayleigh-Ritz inequality [57] for a symmetric matrix guarantees that $\lambda_{\min}(M) \leq \mathbf{x}^T M \mathbf{x} \leq \lambda_{\max}(M) \mathbf{x}^T \mathbf{x}$, which is a useful relation to establish the absolute bounds on the state for guaranteed stability. To apply this, M must be positive-definite. Assuming that M is indeed positive-definite to proceed with this reasoning, using the Rayleigh-Ritz inequality:

$$\begin{aligned} \tilde{\mathbf{x}}^T M \tilde{\mathbf{x}} &\geq \lambda_{\min}(M) \tilde{\mathbf{x}}^T \tilde{\mathbf{x}} > \|\tilde{\mathbf{x}}\| \lambda_{\max}(I_c^{-1}P) \|\dot{\lambda}_{c_d}\| \\ \Rightarrow \lambda_{\min}(M) \|\tilde{\mathbf{x}}\|^2 &> \|\tilde{\mathbf{x}}\| \cdot \lambda_{\max}(I_c^{-1}P) \cdot \|\dot{\lambda}_{c_d}\| \\ \Rightarrow \|\tilde{\mathbf{x}}\| &> \frac{\lambda_{\max}(I_c^{-1}P)}{\lambda_{\min}(M)} \|\dot{\lambda}_{c_d}\|. \end{aligned} \quad (6.10)$$

It follows that if the norm of $\dot{\lambda}_{c_d}$ is bounded, then the norm of $\|\tilde{\mathbf{x}}\|$ remains bounded and the system is input-to-state stable. Essentially, if the modulus of the error variables is greater than a given bound, the derivative of the Lyapunov function is negative and V_2 is decreasing. If the error is smaller than this bound, there is no guarantee on the sign of $\dot{V}_2(\tilde{\mathbf{x}})$, but it is guaranteed that the error remains inside the level set $\|\tilde{\mathbf{x}}\| < \frac{\lambda_{\max}(I_c^{-1}P)}{\lambda_{\min}(M)} \|\dot{\lambda}_{c_d}\|$. This is related to ultimate boundedness, as explained in Section 5.1.

M is positive definite if all its eigenvalues are real and positive. Given that M is a block diagonal matrix, with zeros in the off-diagonal terms, using Schur's complement condition for positive definiteness, M is positive definite if and only if $K_{\text{ang}} - \frac{1}{2}I > 0$ and $K_w - I_c^{-1}P - \frac{1}{2}T > 0$. The first condition is met if

$$\begin{cases} K_\theta > 0.5 \\ K_\psi > 0.5 \end{cases} \quad (6.11)$$

The second condition can be written as $K_w > \underbrace{I_c^{-1}P + \frac{1}{2}T}_Q$. Assuming that $K_\theta = K_\psi$, then $K_{\text{ang}} = K_\theta I$ and $T = K_\theta^2 I_c^{-1} P f_0^{-1} I f_0^{-T} (I_c^{-1} P)^T$. Therefore,

$$f_0^{-1} f_0^{-T} = \begin{bmatrix} c^2 \phi + s^2 \phi c^2 \theta & -s^2 \theta c \phi s \phi \\ -s^2 \theta c \phi s \phi & s^2 \phi + c^2 \phi c^2 \theta \end{bmatrix} = \begin{bmatrix} a & -c \\ -c & b \end{bmatrix}, \quad (6.12)$$

and

$$I_c^{-1} P = \begin{bmatrix} 0 & \frac{I_{zz} - I_{xx}}{I_{yy}} p \\ \frac{I_{yy} - I_{xx}}{I_{zz}} p & \end{bmatrix} = K_I \begin{bmatrix} 0 & 1 \\ 1 & 0 \end{bmatrix}. \quad (6.13)$$

By construction, $K_I > 0$, because $I_{yy} > I_{xx}$. Thus, the eigenvalues of $I_c^{-1} P$ are always real and positive. Using the two previous definitions:

$$\begin{aligned} T &= K_\theta^2 K_I^2 \begin{bmatrix} b & -c \\ -c & a \end{bmatrix} \\ \Rightarrow Q &= \begin{bmatrix} \frac{1}{2} K_\theta^2 K_I^2 b & K_I - \frac{1}{2} K_\theta^2 K_I^2 c \\ K_I - \frac{1}{2} K_\theta^2 K_I^2 c & \frac{1}{2} K_\theta^2 K_I^2 a \end{bmatrix}. \end{aligned} \quad (6.14)$$

The objective is to cover the worst case scenario, i.e. maximize the effect of the disturbance. Hence, using the Rayleigh-Ritz inequality for an arbitrary $n \times 1$ real vector, \mathbf{x} :

$$\begin{cases} \lambda_{\min}(K_w) \mathbf{x}^T \mathbf{x} \leq \mathbf{x}^T K_w \mathbf{x} \leq \lambda_{\max}(K_w) \mathbf{x}^T \mathbf{x} \\ \lambda_{\min}(Q) \mathbf{x}^T \mathbf{x} \leq \mathbf{x}^T Q \mathbf{x} \leq \lambda_{\max}(Q) \mathbf{x}^T \mathbf{x}. \end{cases} \quad (6.15)$$

Combining this, $K_w - I_c^{-1} P - \frac{1}{2} T > 0$ if:

$$\begin{aligned} \lambda_{\min}(K_w) \mathbf{x}^T \mathbf{x} &> \lambda_{\max}(Q) \mathbf{x}^T \mathbf{x} \\ \Rightarrow \lambda_{\min}(K_w) \|\mathbf{x}\|^2 &> \lambda_{\max}(Q) \|\mathbf{x}\|^2 \\ \Rightarrow \lambda_{\min}(K_w) &> \lambda_{\max}(Q) \end{aligned} \quad (6.16)$$

Since $Q \geq 0$, $\|Q\| = \lambda_{\max}(Q)$. The matrix trace is bounded by $\|Q\| \leq \text{tr}(Q) \leq n\|Q\|$, hence $\lambda_{\max}(Q) \leq \text{tr}(Q)$. Therefore to guarantee that M is positive-definite, $\lambda_{\min}(K_w) > \text{tr}(Q)$. From 6.14:

$$\begin{aligned} \text{tr}(Q) &= \frac{1}{2} K_\theta^2 K_I^2 (a + b) \\ &= \frac{1}{2} K_\theta^2 K_I^2 (c^2 \phi + s^2 \phi c^2 \theta + s^2 \phi + c^2 \phi c^2 \theta) \\ &= \frac{1}{2} K_\theta^2 K_I^2 (1 + \underbrace{c^2 \theta}_{0 \leq c^2 \theta \leq 1}) \leq K_\theta^2 K_I^2 \end{aligned} \quad (6.17)$$

Finally, to guarantee positive definiteness of M , it is required that $\lambda_{\min}(K_w) > K_\theta^2 K_I^2$. This relation is shown in Figure 6.1. In order to guarantee positive-definiteness of M , the minimum value of K_w must be above the blue line, as shown. It must be noted

that these are conservative values for the choice of gains, as they were obtained for the worst case scenario. It is guaranteed that if K_w is chosen with this criteria, the system is input-to-state stable. Smaller values for these gains may also ensure stability, although no theoretical guarantee is given, with the selected Lyapunov function. Figure 6.1 does not show the maximum error, as it only relates the minimum gain of K_w for each value of K_θ that guarantees positive-definiteness of M .

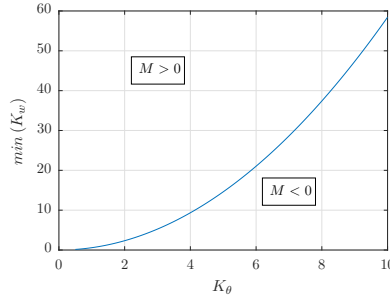
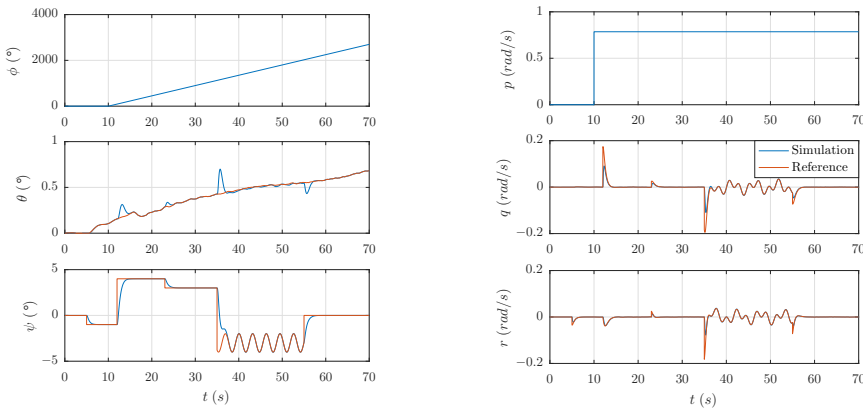


Figure 6.1: Minimum value of K_w as a function of the gain K_θ , for $p = 45^\circ/\text{s}$

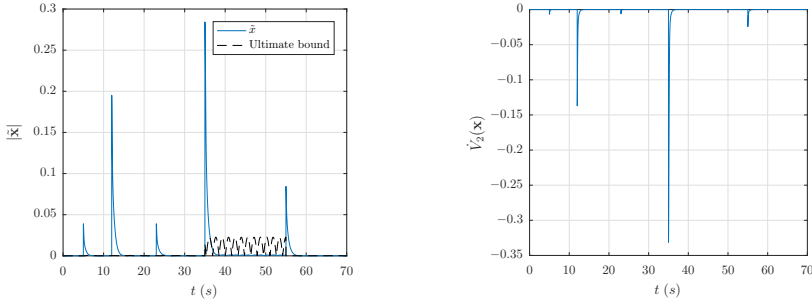


(a) Simulated Euler angles and reference

(b) Simulated angular velocity and reference

Figure 6.2: Simulation for a reference trajectory, with $K_w = 5 \cdot I$ and $K_{\text{ang}} = 2 \cdot I$ for $p = 45^\circ/\text{s}$

The condition on the maximum error is given by Eq. (6.10). This condition depends on the trajectory of the system because T depends on the Euler angles. Figure 6.2a shows a simulation of the system affected by a roll-rate perturbation of $45^\circ/\text{s}$. Figures 6.2a and 6.2b show respectively the Euler angles and the angular velocities: reference in orange and simulated variables in blue. From these figures, one can see that the disturbance starts acting at $t=10$ s and keeps active until the end of the simulation. In the presence of a non-null roll-rate, there is a coupling between the motion in the y and z axes, which is clear for example around $t=15$ s (see figure 6.2a). The abrupt change in the reference for ψ causes the tracking of θ to be degraded.



(a) Absolute state error, $|\tilde{\mathbf{x}}|$ vs. ultimate bound (b) Lyapunov function derivative, $\dot{V}_2(\mathbf{x})$

Figure 6.3: Lyapunov function and its derivative, with $K_w = 5 \cdot I$ and $K_{\text{ang}} = 2 \cdot I$ for $p = 45^\circ/\text{s}$

Figures 6.3a and 6.3b show respectively the error norm $\|\tilde{\mathbf{x}}\|$ and the Lyapunov function derivative, \dot{V}_2 . Comparing both figures, one can see that the behaviour of the system is in line with the conclusions of eq. (6.11): if the error is above the threshold (black dashed line in figure 6.3a) the Lyapunov function derivative is negative and if the error is below the threshold (as it is the case between $t=35$ s and $t=55$ s), then the error is bounded. Furthermore, one can see in Figure 6.3b that $\dot{V}_2 \leq 0$, which could not be concluded solely based on Eq. (6.11) but is observed in simulation.

6.2. ROBUSTNESS TO BOUNDED DISTURBANCES IN THE AERODYNAMIC TORQUE

Consider that the aerodynamic torque is now the sum of its nominal value and an unknown bounded disturbance: $A = A_n + \delta A$, $\|\delta A\| < a$. The derivative of the Lyapunov function is now given by

$$\dot{V}_2(\tilde{\lambda}_c, \tilde{\omega}_c) = -\tilde{\lambda}_c^T K_{\text{ang}} \tilde{\lambda}_c - \tilde{\omega}_c I_c^{-1} [I_c f_0(\phi, \theta) + A + \delta A_n + B u - I_c \dot{\omega}_{cd}] . \quad (6.18)$$

Substituting the nominal control and collecting the terms,

$$\dot{V}_2(\tilde{\lambda}_c, \tilde{\omega}_c) = -\tilde{\lambda}_c^T K_{\text{ang}} \tilde{\lambda}_c - \tilde{\omega}_c I_c^{-1} K_w \tilde{\omega} + \tilde{\omega}_c I_c^{-1} \delta A . \quad (6.19)$$

There is a new term due to the bounded disturbance. Defining $\tilde{\mathbf{x}} = [\tilde{\lambda}_c^T \tilde{\omega}_c^T]^T$ as the state, one can rewrite the previous equation as

$$\dot{V}_2(\tilde{\mathbf{x}}) = -\tilde{\mathbf{x}}^T M \tilde{\mathbf{x}} + \tilde{\mathbf{x}}^T N \delta A, \quad (6.20)$$

where

$$M = \begin{bmatrix} K_{\text{ang}} & 0 \\ 0 & K_w \end{bmatrix}, \quad N = \begin{bmatrix} 0 & 0 \\ 0 & I_c^{-1} \end{bmatrix} .$$

Combining the Rayleigh-Ritz inequality and Eq. (6.20) yields:

$$\|\tilde{\mathbf{x}}\| > \frac{\lambda_{\max}(N)}{\lambda_{\min}(M)} \|\delta A\|. \quad (6.21)$$

To assess the worst case scenario consider the maximum value of N which is the largest eigenvalue of I_c^{-1} at $t=0$. Hence $N_{\max} = 1.2753e-5$. Considering the operation region of the launch vehicle, it is reasonable to assume that the maximum value of the aerodynamic torque disturbance is of the magnitude of the other torques acting on the system. Hence, $\delta A \approx 10^5$ N.m. Considering this value, Figure 6.4 shows that with gains in the order of 10, the maximum error is of magnitude 0.1. The relation expressed in Eq. (6.21) is independent of the trajectory and does not impose any further restrictions on the controller gains to guarantee input-to-state stability. Thus, the condition for input-to-state stability is that all gains must be positive. However, Eq. (6.21) establishes a relation between the magnitude of the error and the magnitude of the disturbance. This relation is in accordance with the empirical rule that increasing the controller gains, the error decreases. Obviously there are limits to the reasonable maximum perturbation in the aerodynamic torque, as well as the maximum allowable gains, as high gains can amplify measurement errors. However, these upper limits do not stem from this analysis. This limitation will also be evident in other cases and will be further discussed in the sequel.

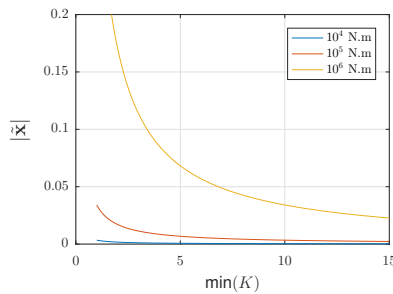


Figure 6.4: Absolute control variable error as a function of the minimum gains

6.3. ROBUSTNESS TO DISTURBANCES ON ANGULAR VELOCITY MEASUREMENT

Disturbances on the measurement of control variables arise from the sensors. Consider that the measurement is affected by a bias (b) and Gaussian white noise (n). Furthermore, assume that the maximum absolute value of the measurement error is bounded, $\|\delta\omega_c\| < a$, where $\delta\omega_c = b + n$.

The sensor gets a corrupted measurement, $\omega_{c_m} = \omega_{c_N} + \delta\omega_c$, that will be used to compute the control signal. The reference tracking error is given by $\tilde{\omega}_c = \omega_{c_N} + \delta\omega_c - \omega_{c_d} = \tilde{\omega}_{c_N} + \delta\omega_c$. This perturbation enters the system via the control signal. From the nominal control signal $u_N = -B^{-1} [A + I_c f_0^T \lambda_c + I_c (K_w \tilde{\omega}_c - \dot{\omega}_{c_d})]$. The measurement will be used directly in $\tilde{\omega}_c$, but it is also used in $\dot{\omega}_{c_d} = F(\phi, \theta, q, r) (K_{\text{ang}} \hat{\lambda}_c - \hat{\lambda}_{c_d}) +$

$f_0^{-1}(\ddot{\lambda}_{c_d} - K_{\text{ang}}\dot{\lambda}_{c_d})$. The expression $F(\phi, \theta, q, r)$ can be written as a function of the error variable $\tilde{\omega}_c$, so it is necessary to express the dependence on the error in $F(\phi, \theta, q, r)$, as well as in $\dot{\lambda}_c = f_0(\lambda)\tilde{\omega}_c - K_{\text{ang}}\tilde{\lambda}_c$ in the second term. Thus, the analytical expression of the dependence on the measurement error becomes cumbersome. To address this problem, more powerful mathematical tools are required to find a closed form solution for this equation, which is beyond the scope of this work.

For the sake of simplicity, the following assumptions are proposed:

- $\tilde{\theta}_c = \tilde{q}_c = 0$ (planar motion only around the z-axis);
- $\lambda_d = 0$ (rectilinear trajectory);
- $K_w = k_1 I$, $K_{\text{ang}} = k_2 I$ (controller gains are constant and fixed);
- The only disturbance acting on the system is $\delta\omega_c$.

With these assumptions, it is possible to simplify the expression for $\dot{\omega}_{c_d}$. Given $\lambda_d = 0 \wedge \tilde{\lambda} = 0 \Rightarrow \theta = 0$. Substituting this in the expression for $F(\phi, \theta, q, r)$ yields $F(\phi, \theta, q, r) = 0$. Furthermore, if $\lambda_d = 0 \Rightarrow \dot{\lambda}_d = \ddot{\lambda}_d = 0$, it can be concluded that $\dot{\omega}_{c_d} = f_0^{-1}K_{\text{ang}}f_0\tilde{\omega}_c - K_{\text{ang}}\tilde{\lambda}_c$. Substituting the corrupted measurement in this expression yields: $\dot{\omega}_{c_d} = \underbrace{f_0^{-1}K_{\text{ang}}f_0\tilde{\omega}_c - K_{\text{ang}}\tilde{\lambda}_c}_{\dot{\omega}_{c_dN}} + f_0^{-1}K_{\text{ang}}f_0\delta\omega_c$.

Now, substituting the corrupted control signal in the Lyapunov function derivative and collecting the terms yields:

$$\begin{aligned} \dot{V}_2 &= -\tilde{\lambda}_c^T K_{\text{ang}}\tilde{\lambda}_c + \tilde{\omega}_c^T I_c^{-1} \left[I_c f_0 \tilde{\lambda}_c + A - BB^1 \left(I_c f_0 \tilde{\lambda}_c + A + I_c (K_w \omega_{c_N} - \dot{\omega}_{c_dN} - f_0^{-1} K_{\text{ang}} f_0 \delta\omega_c) \right) - I_c \dot{\omega}_{c_dN} \right] \\ &= -\tilde{\lambda}_c^T K_{\text{ang}}\tilde{\lambda}_c - \tilde{\omega}_c^T K_w \tilde{\omega}_c - \tilde{\omega}_c (K_w - K_\theta) \delta\omega_c . \end{aligned} \quad (6.22)$$

Using the previous definition of $\tilde{\mathbf{x}}$, one can rewrite \dot{V}_2 as:

$$\dot{V}_2 = -\tilde{\mathbf{x}}^T M \tilde{\mathbf{x}} + \tilde{\mathbf{x}}^T \delta\omega_c , \quad (6.23)$$

where $M = \begin{bmatrix} K_{\text{ang}} & 0 \\ 0 & K_w \end{bmatrix}$ and $P = \begin{bmatrix} 0 \\ -(K_w - K_\theta) \end{bmatrix}$. By using the Rayleigh-Ritz inequality as before, the following condition for input-to-state stability is obtained:

$$\|\tilde{\mathbf{x}}\| > \frac{|K_w - K_\theta|}{\min(K_w, K_\theta)} \|\delta\omega_c\| . \quad (6.24)$$

Figure 6.5 shows a graphical representation of condition expressed in Eq. (6.24). As expected, the absolute value of the error grows with the measurement error. Furthermore, if the gain of the inner loop is set much larger than the gain of the outer loop, performance is also degraded, as the error increases.

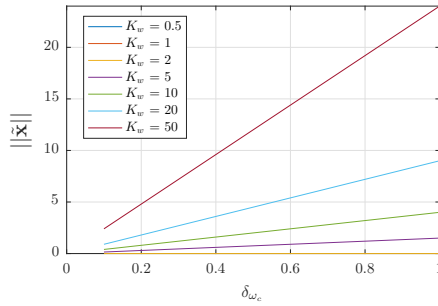


Figure 6.5: State error for varying K_w and $K_\theta = 2$

6.4. ROBUSTNESS TO DISTURBANCES ON EULER ANGLE MEASUREMENT

The case of disturbances on the Euler angles measurement is similar to the previous case of disturbances on the angular velocity measurement, albeit more complex. In this case, consider also that the measurement is affected by a bias (b) and Gaussian white noise (n).

As before, the maximum absolute value of the measurement error is bounded, $\|\delta\lambda_c\| < a$, where $\delta\lambda_c = b + n$. The sensor gets the corrupted measurement: $\lambda_{c_m} = \lambda_{c_N} + \delta\lambda_c$, that will be used to compute the control signal. Similarly to the previous case, the tracking error is given by $\tilde{\lambda}_c = \lambda_{c_N} + \delta\lambda_c - \lambda_{c_d} = \tilde{\lambda}_{c_N} + \delta\lambda$. This perturbation enters the system via the control signal but also through the system dynamics. Since the expressions for f_0 and f_0^{-1} are a function of the Euler angles, the corrupted measurement must be replaced in every occurrence of these functions, as well as in the derivatives $\dot{\tilde{\lambda}}_c$ and $\dot{\omega}_{c_d}$, which renders the analytical manipulation of this expression much more complex than in the previous case. However, given that the process is the same as before, it is omitted.

6.5. ROBUSTNESS TO DISTURBANCES IN THE INERTIA MATRIX

Inaccuracies in the model of the inertia matrix can be treated using similar arguments as before, however the resulting expressions are considerably more complex. Thus, the analysis will be divided in two subcases: first, addressing the situation where only the diagonal terms of the inertia matrix are perturbed and secondly the case where there are off-diagonal perturbations. The second case completely changes the dynamics of the system, because the presence of cross-terms induces dynamics on the roll rate, making the analysis substantially harder.

6.5.1. DISTURBANCES IN THE DIAGONAL TERMS OF THE INERTIA MATRIX

Disturbances in the inertia matrix result from small mass distribution anomalies that arise from the production process, causing an uncertainty around the nominal projected value of the inertia coefficients. Consider the deviation as a percentage of the nominal value at any given time: $dI_{yy}(t) = I_{yy,bias} \cdot I_{yy}(t)$, $I_{yy,bias} \in [-0.5, 0.5]$. For this problem, a deviation

of $\pm 50\%$ around the nominal value is not realistic and well beyond operation region of the launcher. However, the mathematical analysis will be carried on, as the results will clearly illustrate the impact of those terms. Furthermore, disturbances associated with I_{xx} are not considered, given that there is no actuation in this axis and this variable is not used in the controller synthesis. Hence, the disturbance in the model has the following description:

$$\delta I_c = \begin{bmatrix} \delta I_{yy} & 0 \\ 0 & \delta I_{zz} \end{bmatrix}.$$

The model of the perturbed system is given in Eq. 6.25:

$$\begin{cases} \dot{\tilde{\lambda}}_c = f_0 \tilde{\omega}_c - K_{\text{ang}} \tilde{\lambda}_c \\ \dot{\tilde{\omega}}_c = (I_{c_n} + \delta I)^{-1} (A + Bu) - \dot{\omega}_{c_d} \end{cases} \quad (6.25)$$

The derivative of the Lyapunov function for this model is:

$$\dot{V}_2 = -\tilde{\lambda}_c^T K_{\text{ang}} \tilde{\lambda}_c + \tilde{\omega}_c^T (I_{c_n} + \delta I)^{-1} [(I_{c_n} + \delta I) f_0 \tilde{\lambda}_c + A + Bu - (I_{c_n} + \delta I) \dot{\omega}_{c_d}] \quad (6.26)$$

In Eq. (6.26) the perturbation term, δI , multiplies the derivative $\dot{\omega}_{c_d}$, which was not the case in the previous considered perturbations. Therefore, the nominal control will not cancel out the term $\dot{\omega}_{c_d}$ as before. Thus, the expression of $\dot{\omega}_{c_d}$ (see Eq. (5.33)) introduces a much more complex problem, since it is a function of state and desired variables and its analytical expression (needed to proceed with the Lyapunov analysis). Therefore, it is difficult to derive. Nonetheless, the analytical procedure will be carried on as before, developing the expression for the Lyapunov function derivative as much as possible. Substituting the nominal control and the expression for $\dot{\omega}_{c_d}$ in Eq. (6.26) and collecting the terms:

$$\begin{aligned} \dot{V}_2 = & \tilde{\lambda}_c^T \dot{\tilde{\lambda}}_c - \tilde{\omega}_c^T (I_{c_n} + \delta I)^{-1} (I_{c_n} K_w - \delta I f_0^{-1} K_{\text{ang}} f_0) \tilde{\omega}_c \\ & + \underbrace{\tilde{\omega}_c^T (I_{c_n} + \delta I)^{-1} \delta I (f_0 - f_0^{-1} K_{\text{ang}}^2 + F(\phi, \theta, q, r) K_{\text{ang}})}_{\mathbf{x}^T} \underbrace{\tilde{\lambda}_c}_{\mathbf{y}} \\ & - \tilde{\omega}_c^T (I_{c_n} + \delta I)^{-1} \delta I f_0^{-1} \dot{\tilde{\lambda}}_{c_d} - \tilde{\omega}_c^T (I_{c_n} + \delta I)^{-1} \delta I F(\phi, \theta, q, r) \dot{\lambda}_{c_d} \end{aligned} \quad (6.27)$$

Using Young's inequality for the cross-term in the previous equation:

$$\begin{aligned} \dot{V}_2 \leq & -\tilde{\lambda}_c^T \left(K_{\text{ang}} - \frac{1}{2} I \right) \tilde{\lambda}_c - \tilde{\omega}_c^T \left[(I_{c_n} + \delta I)^{-1} (I_{c_n} K_w - \delta I f_0^{-1} K_{\text{ang}} f_0) - \frac{1}{2} T \right] \\ & - \tilde{\omega}_c^T (I_{c_n} + \delta I)^{-1} \delta I f_0^{-1} \dot{\tilde{\lambda}}_{c_d} - \tilde{\omega}_c^T (I_{c_n} + \delta I)^{-1} \delta I F(\phi, \theta, q, r) \dot{\lambda}_{c_d} \end{aligned} \quad (6.28)$$

where

$$\begin{aligned} T = & (I_{c_n} + \delta I)^{-1} \delta I (f_0 - f_0^{-1} K_{\text{ang}}^2 \\ & + F(\phi, \theta, q, r) K_{\text{ang}}) (f_0 - f_0^{-1} K_{\text{ang}}^2 + F(\phi, \theta, q, r) K_{\text{ang}})^T \delta I^T ((I_{c_n} + \delta I)^{-1})^T \end{aligned} \quad (6.29)$$

Making the same assumptions as in the previous sections, a relation between the modulus of the state error and the modulus of the perturbation would be obtained (similar to the one in Eq. (6.24)). However, as it is similar to the previous cases, it will not be further developed. Next, the case of disturbances in the off-diagonal terms of the inertial matrix is addressed.

6.5.2. DISTURBANCES IN THE NON-DIAGONAL TERMS OF THE INERTIA MATRIX

This case is different from the previous one, as the dynamics of the system changes considerably in the presence of the off-diagonal terms. Given the geometry of the system, the inertia matrix must be symmetrical. Since there is no control over the x -axis, consider a cross terms only in the part of the inertia matrix that is used for control, with $I_{yz} = I_{zy}$ and $\delta I_{yz} = \delta I_{zy}$. The inertia matrix becomes:

$$\begin{bmatrix} I_{xx} & 0 & 0 \\ 0 & I_{yy} & I_{yz} \\ 0 & I_{zy} & I_{zz} \end{bmatrix}. \quad (6.30)$$

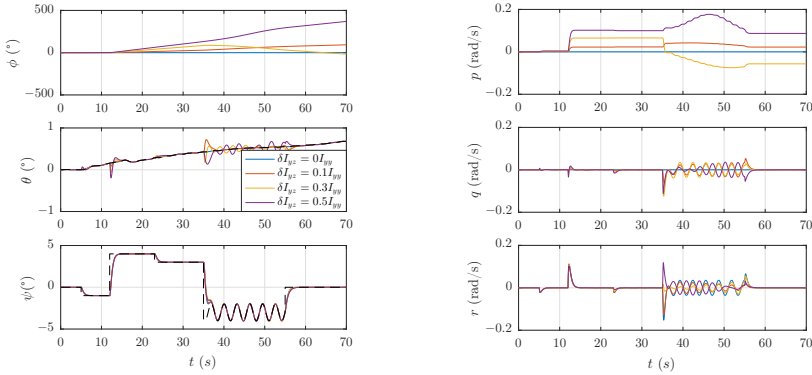
Developing Euler's equation for rotational motion with the new inertia matrix:

$$\begin{cases} \dot{p} = \frac{I_{yz}}{I_{xx}} (r^2 - q^2) \\ \dot{q} = \frac{1}{I_{yy}} (M_y - (I_{xx} - I_{zz})pq + I_{yz}(pq - \dot{r})) \\ \dot{r} = \frac{1}{I_{zz}} (M_z - (I_{xx} - I_{yy})pq - I_{yz}(pr - \dot{q})) \end{cases}. \quad (6.31)$$

From Eq. (6.31) one can see that \dot{p} now has non-trivial dynamics, changing the overall system dynamics. Therefore, the expression found for the Lyapunov function derivative in the previous case is not applicable, as the effect of \dot{p} must be considered. Due to the new terms in the dynamics of the controlled part of the system, one can see that more terms will appear in the Lyapunov function. Nevertheless, the process for obtaining a mathematical condition for a constraint for the gains is the same as in those cases, albeit more complicated. As seen in the previous section, the expression for the Lyapunov function derivative is complex and for this case more complexity arises from the extra terms on the dynamics of the system. However, an intuitive reasoning about the stability of the system with this type of perturbations is given next.

The inertial model of rocket launchers is well known, as it is tested and validated exhaustively prior to launch. Therefore, unmodelled dynamics that originate this kind of cross terms are expected to be very small when compared with the principal (well-known) moments of inertia. If $I_{yz} \ll I_{yy}$, then the extra terms in the equations of \dot{q} and \dot{r} will also be small. If these terms are small, then the system can follow the computed angular velocity reference, although with a possibly larger error. If it is possible to track the reference, then the dynamics of \dot{p} are bounded. Hence, for small deviations this case can be approximated by the bounded roll-rate disturbance case studied in this section, which is input-to-state stable. To support this reasoning, simulations for different values of the off-diagonal inertia matrix perturbation are provided. The disturbance is modelled as a percentage of the principal moment of inertia, i.e., $\delta I_{yz} = a\delta I_{yy}$, $a \in [0, 1]$.

Figures 6.6 and 6.7 show the results of simulations with different values for δI_{yz} and with all the other parameters fixed. The nominal case is given by $\delta I_{yz} = 0$ and is shown here for comparison purposes. Figures 6.6a and 6.6b show that the tracking of the Euler angle and angular velocity reference is degraded as the uncertainty in δI_{yz} increases. Furthermore, as the uncertainty in this parameter increases, the magnitude of p also increases, which in turn causes the coupling between the responses in the other two axis to become stronger. Nonetheless for this case, the system is input-to-state stable, as the Lyapunov function is always positive (Figure 6.7b) and its derivative always negative (Figure 6.7b).



(a) Simulated Euler angles and reference

(b) Simulated angular velocity and reference

Figure 6.6: Simulation of Euler angles and angular velocity, with different values of the perturbation δI_{yz}

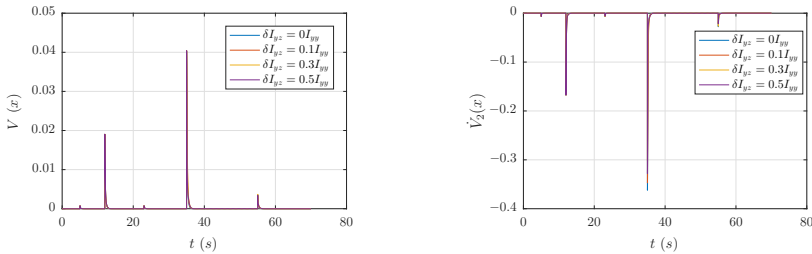
(a) Lyapunov function, for varying δI_{yz} (b) Lyapunov function derivative, for varying δI_{yz}

Figure 6.7: Simulation of state variables and absolute error, with different values of the perturbation δI_{yz}

6.6. EFFECT OF FLEXIBLE MODES

The controller was developed without considering the flexible modes in its design. It is well known that the flexible modes can be excited by the controller, and if the control action is ill dimensioned, it can interfere with natural frequencies of the modes and amplify them, ultimately leading to instability.

Recalling Section 2.4, the flexible modes are modelled as poorly damped second order systems, excited by the thrust force along the y_B axis, inducing an extra force in the y_B axis that generates a moment in the z_B axis.

Several simulations were run, considering different trajectories and it was found that the effect of the flexible modes in the overall system performance is negligible, for this particular launch vehicle.

Nonetheless, the impact of flexible modes must be assessed so that the design procedures described here can be extended to other launch vehicles for which the effect of the flexible modes may be important. Therefore, an artificial gain in the force and moment induced by the flexible modes¹ is introduced. This gain is increased to a point where the flexible modes clearly influence the system's behaviour. One must be careful when selecting this gain because, if it is set too high, the dynamics of the system can be dominated by the dynamics of the flexible modes. If this happens, one can no longer assess the choice of the controller parameters and its relation with the flexible modes.

It was concluded that a gain $K_{flex} = 600$ generates flexible moments of the order of magnitude of the other forces at game in the system. Furthermore, it is important to note that the trajectory of the system also determines the way the flexible modes affect the system: since the flexible moment (in the z-axis) depends on the thrust along the y_B -axis, trajectories with a demanding reference signal in the z_B -axis require a greater torque along the y_B component, which in turn induces stronger moments caused by the flexible modes. For this reason, a new test trajectory is introduced, as illustrated in Figure 6.8. This trajectory is designed to ask a demanding signal in the z_B -axis, where it was seen that the influence of the flexible modes is greater.

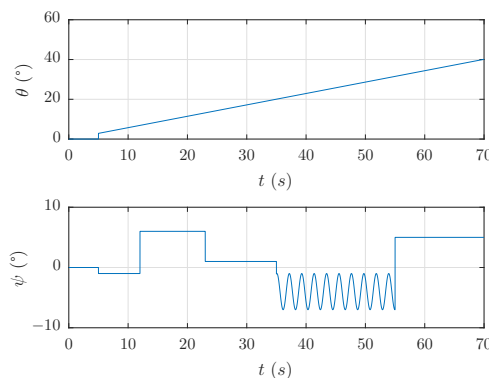


Figure 6.8: Test trajectory for the effects of the flexible modes

¹ $F_{flex_{new}} = K_{flex} F_{flex}$ and $M_{flex_{new}} = K_{flex} M_{flex}$

To evaluate the effect of the flexible modes on the stability of the system, the Lyapunov function is augmented with the flexible modes states. Once more, the goal is to check positive-definiteness if the Lyapunov function that its derivative is negative semi-definite.

Each individual flexible mode can be written using the canonical form:

$$\begin{bmatrix} \dot{q}_1 \\ \ddot{q}_1 \end{bmatrix} = \begin{bmatrix} 0 & 1 \\ -\omega_1^2 & -2\xi\omega_1 \end{bmatrix} \begin{bmatrix} q_1 \\ \dot{q}_1 \end{bmatrix} + \begin{bmatrix} 0 \\ T_y t_{p1} \end{bmatrix} \quad (6.32)$$

The new Lyapunov function depends on the augmented state $\mathbf{x} = [\tilde{\lambda}_c \ \tilde{\omega}_c \ q_i \ \dot{q}_i]^T$:

$$V_2(\mathbf{x}) = \frac{1}{2} \mathbf{x}^T \mathbf{x} = [\tilde{\lambda}_c \ \tilde{\omega}_c \ q_i \ \dot{q}_i]^T \begin{bmatrix} f_0(\tilde{\lambda}_c)\omega_c - K_{\text{ang}}\tilde{\lambda}_c \\ I_c^{-1}(A + Bu + M_{\text{flex}}) - \dot{\omega}_{cd} \\ \dot{q}_i \\ -\omega_i q_i - 2\xi\omega_i - c_1 u_q t_{pi} \end{bmatrix} \quad (6.33)$$

Taking the time derivative of Eq. (6.33) and collecting terms yields

$$\dot{V}_2(\mathbf{x}) = -\tilde{\lambda}_c^T K_{\text{ang}} \lambda_c - \tilde{\omega}_c^T K_w \tilde{\omega}_c + \omega_c^T I_c^{-1} M_{\text{flex}} + q_i \dot{q}_i + \dot{q}_i \ddot{q}_i \quad (6.34)$$

Recalling that $M_{\text{flex}} = \begin{bmatrix} 0 \\ 0 \\ c_1 u_q (r_{p1} I_{GA} + t_{p1}) q_i \end{bmatrix}$ it is clear that a component of the control vector u_q appears in the derivative of the Lyapunov function. For this reason, developing Eq. (6.34) analytically is extremely difficult. It is assumed that:

- $\theta_c = 0$;
- $K_w = K_q I$;
- $K_{\text{ang}} = K_\theta I$;
- There is only one flexible mode

After some lengthy algebraic manipulations, the following expression for the derivative of the proposed Lyapunov function is obtained:

$$\begin{aligned} \dot{V}_2(\mathbf{x}) = & -K_\theta \tilde{\theta}_c^2 - K_\theta \tilde{\psi}_c^2 - K_q (\tilde{q}_c^2 + \tilde{r}_c^2) - 2\xi\omega_1 \dot{q}_1^2 - A_q (r_{p1} I_{GA} + t_{p1}) \tilde{r}_c q_1 \\ & + ((K_q + K_\theta) \tilde{r}_c + (1 - K_\theta^2) c \phi \tilde{\theta}_c \tilde{r}_c - (1 + K_\theta^2) s \phi \tilde{\psi}_c \tilde{r}_c) (r_{p1} I_{GA} + t_{p1}) q_1 \\ & + (1 - \omega_1^2) q_1 \dot{q}_1 + A_q t_{p1} \dot{q}_1 + I_{yy} ((K_q + K_\theta) \tilde{q}_c + (1 - K_\theta^2) c \phi \tilde{\omega}_c - (1 - K_\theta^2) s \phi \tilde{\psi}_c) t_{p1} \dot{q}_1 \end{aligned} \quad (6.35)$$

Equation (6.35) considers only one flexible mode and some assumptions were made in its development. From this, it is clear that the effect of the flexible modes in the system is complex and difficult to assess. Nonetheless, some general considerations can be drawn from Eq. (6.35). The first four terms are quadratic and have a negative sign. Hence, they are always negative and contribute to the stability of the system. The remaining terms are cross terms between the flexible modes states and the other system's states and it is not possible to assess its sign or magnitude without further assumptions. However, these possibly unstable terms depend on the controller gains. Hence, increasing the gains also increases their importance in the derivative of the Lyapunov function, which can lead to instability. This is in line with what was found for

the inclusion of the flexible modes in the linear system, in Chapter 4. Introducing more flexible modes (the considered launch vehicle only has two), the number of possible unstable terms in Eq. (6.35) increases, so it is expected that including more flexible modes in the system contributes to the loss of stability of the system. To check if this is true, the effect of flexible modes in the system will be studied through simulations of the nonlinear system. In previous sections, it was seen that the inner loop gains (K_w), associated with the angular velocity error, have greater influence in the performance of the system. Hence, to evaluate the reasoning developed from Eq. (6.35), these gains will be changed, keeping all other parameters of the system constant. The results of the simulations can be seen in Figure 6.9.

For the nominal system (blue line), increasing the gain of the inner loop, decreases the error in the reference tracking of angular velocities and Euler angles, in general. Adding flexible modes to the system, this trend is also verified, but input-to-state stability is lost for lower gains. This can be observed in Figure 6.9. The Euler angles reference tracking is usually better than the tracking of the angular velocities, as can be seen comparing the magnitude of the scales of the Euler angles and angular velocities in Figure 6.9. Due to the extra integrator in the dynamics of the Euler angles, the errors associated with the Euler angles are smaller. Furthermore, the trajectory for which these simulation was run, is more demanding in ψ . Hence, it is expected that the magnitude of the tracking errors along the z_B -axis is larger than the magnitude of the tracking errors along the y_B -axis. This can be verified by comparing the magnitude of the errors of Figure 6.9a with Figure 6.9c and Figure 6.9b with 6.9d.

Combining the two previous remarks, the effect of the gain of the inner loop with the inclusion of flexible modes is more noticeable in Figure 6.9a, which shows the yaw rate tracking error. Adding flexible modes, leads to the loss of stability at lower gains: for the nominal case it is possible to increase the gain until $K_w = 12I$ without losing input-to-state stability, but adding only the low frequency flexible mode, input-to-state stability is lost around $K_w = 10I$ and with both flexible modes around $K_w = 6I$.

Furthermore, in all the Figures, the magnitude of the error increases before losing input-to-state stability (it is more evident in Figure 6.9a), suggesting an asymptotic behaviour when getting close to instability. In order to get the best performance, one could choose the gain that leads to the minimum tracking error, but from this analysis the minimum error occurs very close to the unstable region. Hence, choosing a gain in this region is not safe because a small deviation from the designed point can lead to instability very quickly.

Therefore, to ensure proper functioning of the system, one must choose a lower gain and tolerate a higher tracking error. Figure 6.9a also suggests that, for a fixed gain, the tracking error increases with the inclusion of the flexible modes in the model. It is also interesting to note that the results presented in Figure 6.9 are in line with the results of the analysis of the derivative of the Lyapunov function: in the nominal case, one can increase the gain and the system will always be stable (see Eq. (5.37)). With the flexible modes, it was seen in equation (6.35) that the inclusion of flexible modes limits the performance, since increasing controller gains leads to destabilizing terms in the Lyapunov function derivative.

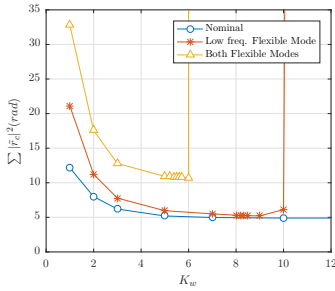
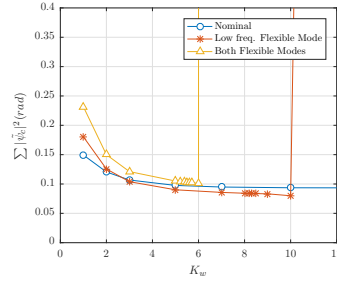
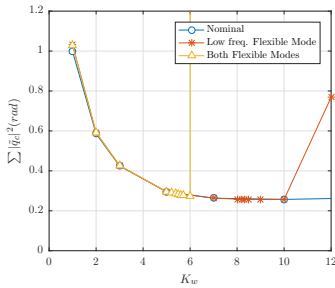
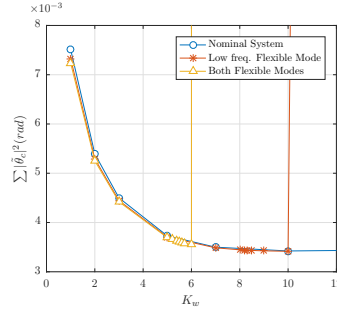
(a) Yaw rate error as a function of K_w (b) Yaw angle error as a function of K_w (c) Pitch rate error as a function of K_w (d) Pitch angle error as a function of K_w

Figure 6.9: Simulation for reference trajectory and errors as a function of the inner loop gain, for the nominal system and for the system with flexible modes

6

6.7. ROBUSTNESS TO PERTURBATIONS ON THE POSITION OF THE CENTER OF MASS, \mathbf{P}_{CG}

Forcing \mathbf{P}_{CG} to be outside the x_B -axis generates moments in the other body axis that are not accounted for in the controller. Thus, even in the nominal case, the error increases with the uncertainty in the position of the center of mass. The effect is different if one changes the position to the y or z axes. The moment equations will be developed taking this into account. Having uncertainty in the position along x_B does not have a significant impact on the system. It is also important to note that the effect of the uncertainty of the position of the center of mass varies with the considered trajectory. The effect of the position of the center of mass for the nominal trajectory will be analysed. In this trajectory, the reference signal in ψ is more demanding than in θ . Consequently, the thrust force along y needs to be larger to generate the necessary moment. Hence, misalignments along the y or z axes have different effects. This will become clearer in the following sections, where the effect of uncertainty in the position of the center of gravity along each of the three body axes is analysed.

6.7.1. VARIATION OF \mathbf{P}_{CG} ALONG THE x_B -AXIS

In section 2.2.3, the forces that generate moments around the center of mass were identified as the aerodynamic and thrust forces. Considering a misalignment between the true position of the center of gravity and the modelled position of the center of gravity along the x-axis: $\mathbf{P}_{CG} = \mathbf{P}_{CG_N} + [\delta_{CG_x} \ 0 \ 0]$. This generates moments in y_B and z_B . For a generic force, with components along the three body axis, the generated moment is given by:

$$\begin{bmatrix} l_{GA_x} + \delta_{CG_x} \\ 0 \\ 0 \end{bmatrix} \times \begin{bmatrix} F_x \\ F_y \\ F_z \end{bmatrix} = \begin{bmatrix} 0 \\ -F_z(l_{GA_x} + \delta_{CG_x}) \\ F_y(l_{GA_x} + \delta_{CG_x}) \end{bmatrix} \quad (6.36)$$

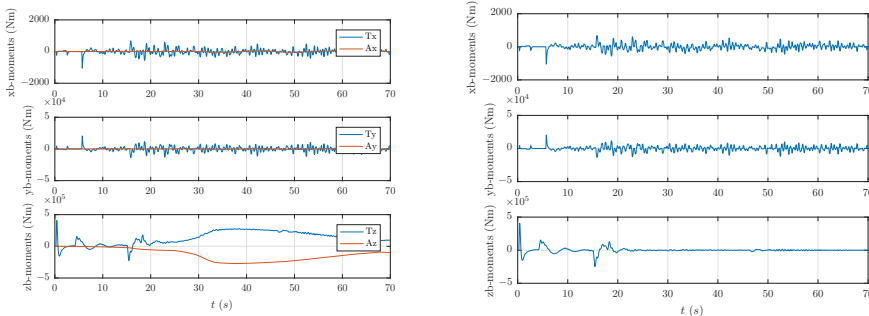
The magnitudes of the forces at play along y_B and z_B are much larger than the maximum value of δ_{CG_x} . Hence, the effect of uncertainty in this axis will be small. Appendix F contains a simulation with uncertainty in the position of the center of gravity along the x_B -axis.

6.7.2. VARIATION OF \mathbf{P}_{CG} ALONG THE y_B -AXIS

Considering a misalignment between the true position of the center of gravity and the modelled position of the center of gravity along the y-axis: $\mathbf{P}_{CG} = \mathbf{P}_{CG_N} + [0 \ \delta_{CG_y} \ 0]$. This will generate moments in all axes. For a generic force, with components along the three body axis, the generated moment is given by:

$$\begin{bmatrix} l_{GA_x} \\ \delta_{CG_y} \\ 0 \end{bmatrix} \times \begin{bmatrix} F_x \\ F_y \\ F_z \end{bmatrix} = \begin{bmatrix} F_z \delta_{CG_y} \\ -F_z l_{GA_x} \\ F_y l_{GA_x} - F_x \delta_{CG_y} \end{bmatrix} \quad (6.37)$$

From the previous equation, it is clear that a moment along the x-axis is induced, which is not counteracted by the controller, as there is no actuation along this axis. Furthermore, there is another induced component in the z_B -axis, multiplying the component of the force along x_B . For the thrust force, the x_B -component is large, so this will have an impact in the overall performance of the system.



(a) External moments for $\delta_{CG_y} = +0.4$ m (b) Total moments for $\delta_{CG_y} = +0.4$ m

Figure 6.10: Moments along the body axis for $\delta_{CG_y} = +0.4$ m

Figure 6.10 shows the aerodynamic and propulsion moments (left), and the total moment along the body axis (right). In this case, there is a moment along the x-axis that is not be controlled and that can lead to instability if the roll moment it generates exceeds the $45^\circ/\text{s}$ threshold defined in the previous chapter. Figure 6.11 shows the response of the nominal system to an uncertainty of $+0.4\text{ m}$ in the location of the center of gravity along the y_B -axis. Although the system is still stable, the controller cannot perfectly track the reference in r and ψ . Looking at Figures 6.11a and 6.11b, a static error between the reference and the actual state can be observed. This difference occurs because the controller is using incomplete information to compute the control signal.

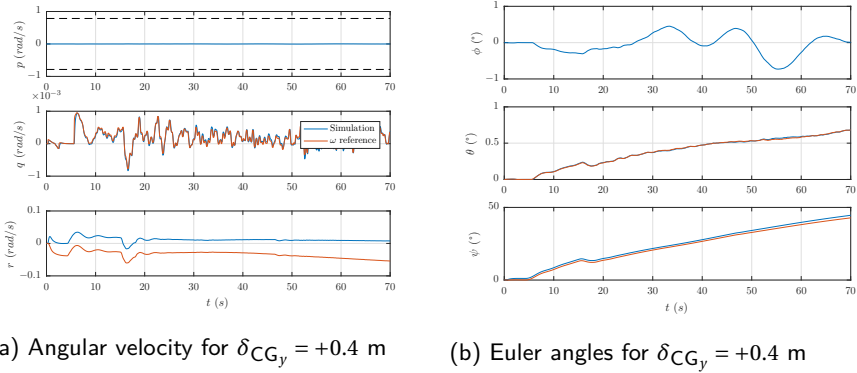


Figure 6.11: Simulation for $\delta_{CG_y} = +0.4\text{ m}$

6.7.3. VARIATION OF \mathbf{P}_{CG} ALONG THE z_B -AXIS

Finally, consider a misalignment between the true position of the center of gravity and the modelled position of the center of gravity along the z-axis, $\mathbf{P}_{CG} = \mathbf{P}_{CG_N} + [0\ 0\ \delta_{CG_z}]$. This generates moments in all axes. For a generic force, with components along the three body axis, the generated moment is:

$$\begin{bmatrix} l_{GA_x} \\ 0 \\ \delta_{CG_z} \end{bmatrix} \times \begin{bmatrix} F_x \\ F_y \\ F_z \end{bmatrix} = \begin{bmatrix} -F_y \delta_{CG_z} \\ F_x \delta_{CG_z} - F_z l_{GA_x} \\ F_y l_{GA_x} \end{bmatrix} \quad (6.38)$$

The component of F_x appears in the y-axis, so the effect of the thrust along this axis will degrade performance. In this case there is also an induced moment in the x-axis. The results are similar to those presented in the previous Section. Hence they are omitted.

6.8. ADAPTIVE BACKSTEPPING CONTROL

In the previous section, it was seen that a misalignment of the position of the center of mass along y or z causes a static error in reference tracking and can lead to instability.

One approach to mitigate this effect is to estimate the true position of the center of mass and use this estimate in the control design.

The goal of this section is to design an estimation law for the position of the center of mass and integrate it with the previously designed controller. Consider that there is a misalignment along the y -axis to proceed with the analysis. If the misalignment had occurred along the z -axis, the procedure described here would be the same. Assume that the aerodynamic moments are known, hence the uncertainty will only affect the moment generated by the thrust force. In this case, the moment induced by the thrust is given by:

$$\begin{bmatrix} l_{GA_x} \\ \delta_{CG_y} \\ 0 \end{bmatrix} \times \begin{bmatrix} T_x \\ T_y \\ T_z \end{bmatrix} = \begin{bmatrix} T_z \delta_{CG_y} \\ -T_z l_{GA_x} \\ T_y l_{GA_x} - T_x \delta_{CG_y} \end{bmatrix} \quad (6.39)$$

Recalling from Chapter 2 that $T_x = Tc\delta_y\delta_p$, the perturbation introduced by the misalignment in the y -axis is a function of the input, thrust and the uncertainty itself. For the nominal trajectory, the control action is smooth and the control angles are limited by the actuators to $\pm 6.5^\circ$. Thus, the small angle approach is valid and $T_x \approx T$. Hence, the moment induced by the perturbation is simply $T\delta_{CG_y}$. Introducing this in the dynamics of the angular velocity error, leads to:

$$\dot{\tilde{\omega}}_c = I_c^{-1} \left(A + Bu - I_c \dot{\omega}_{cd} + \begin{bmatrix} 0 \\ T\delta_{CG_y} \end{bmatrix} \right) \quad (6.40)$$

The perturbation δ_{CG_y} is not known. Hence, its estimate, $\hat{\delta}_{CG_y}$, must be used. Defining the estimation error as $\tilde{\delta}_{CG_y} = \delta_{CG_y} - \hat{\delta}_{CG_y}$, the estimate can replace the perturbation in Eq. (6.40), yielding

$$\dot{\tilde{\omega}}_c = I_c^{-1} \left(A + Bu - I_c \dot{\omega}_{cd} + T\hat{\delta}_{CG_y} \begin{bmatrix} 0 \\ 1 \end{bmatrix} + T\tilde{\delta}_{CG_y} \begin{bmatrix} 0 \\ 1 \end{bmatrix} \right) \quad (6.41)$$

In Chapter 5, the control law u was chosen such that all nonlinear terms are cancelled out and a definite negative term in the Lyapunov function derivative is introduced. The same is done here, but also cancelling the term that depends on the estimated position of the center of mass. Then, the proposed Lyapunov function is used to determine a dynamic update law for $\hat{\delta}_{CG_y}$ that guarantees stability. The new control law is given by:

$$u = -B^{-1} \left(\underbrace{I_c f_o(\phi, \theta)^T \tilde{\lambda}_c + A + I_c (K_w \tilde{\omega}_c - \dot{\omega}_{cd})}_{u_N} - T\hat{\delta}_{CG_y} \begin{bmatrix} 0 \\ 1 \end{bmatrix} \right) \quad (6.42)$$

Augmenting the control Lyapunov function to include the estimation error leads to:

$$V(\tilde{\lambda}_c, \tilde{\omega}_c, \tilde{\delta}_{CG_y}) = \frac{1}{2} \tilde{\lambda}_c^T \tilde{\lambda}_c + \frac{1}{2} \tilde{\omega}_c^T \tilde{\omega}_c + \frac{1}{2} \frac{1}{K_3} \tilde{\delta}_{CG_y}^2 \quad (6.43)$$

In Eq. (6.43), K_3 is a gain to control the convergence of the dynamics of $\tilde{\delta}_{CG_y}$. The derivative of $\tilde{\delta}_{CG_y}$ is given by:

$$\dot{\delta}_{CG_y} = \underbrace{\dot{\delta}_{CG_y}}_{=0} - \dot{\delta}_{CG_y} \Rightarrow \dot{\delta}_{CG_y} = -\dot{\delta}_{CG_y} \quad (6.44)$$

Using Eq. (6.44), the derivative of the new Lyapunov function can be written as:

$$\begin{aligned} \dot{V}(\tilde{\lambda}_c, \tilde{\omega}_c, \tilde{\delta}_{CG_y}) &= \dot{V}_2 + T\tilde{\delta}_{CG_y}\tilde{\omega}_c^T I_c^{-1} \begin{bmatrix} 0 \\ 1 \end{bmatrix} - \frac{1}{K_3}\tilde{\delta}_{CG_y}\dot{\delta}_{CG_y} \\ &= \dot{V}_{2_N} + \underbrace{\tilde{\delta}_{CG_y} \left(T\tilde{\omega}_c^T I_c^{-1} \begin{bmatrix} 0 \\ 1 \end{bmatrix} - \frac{1}{K_3}\dot{\delta}_{CG_y} \right)}_{=0} \end{aligned} \quad (6.45)$$

Using Eq. (6.45), the dynamics of $\dot{\delta}_{CG_y}$ can be chosen such that the term multiplying $\tilde{\delta}_{CG_y}$ is zero.

Choosing $\dot{\delta}_{CG_y} = K_3 T\tilde{\omega}_c^T I_c^{-1} \begin{bmatrix} 0 \\ 1 \end{bmatrix}$, the derivative of the new Lyapunov function is $\dot{V}(\tilde{\lambda}_c, \tilde{\omega}_c, \tilde{\delta}_{CG_y}) \leq 0$. Since \dot{V} is only negative semi-definite and the system is nonautonomous, neither Lyapunov's second method nor LaSalle's Invariance Principle can be applied. However, Barbalat's Lemma can be applied, which ensures that \dot{V} converges to zero, since V converges to a bounded limit and \dot{V} is uniformly continuous. It follows that $\tilde{\lambda}_c$ and $\tilde{\omega}_c$ are guaranteed to converge to zero. Now the backstepping controller incorporates a parameter estimation update law that stabilizes the system. Furthermore, gain K_3 allows controlling the rate of the convergence of the estimate. It is important to note that, given the implementation of the parameter estimation law using the Lyapunov function, the estimation error, $\tilde{\delta}_{CG_y}$ converges to a constant. However, it is not guaranteed that the estimate converges to the true value of the position of the center of mass. In summary, the control law and the parameter estimator are:

$$\begin{cases} u &= -B^{-1} \left(I_c f_o(\phi, \theta)^T \tilde{\lambda}_c + A + I_c(K_w \tilde{\omega}_c - \dot{\omega}_{cd}) - T\dot{\delta}_{CG_y} \begin{bmatrix} 0 \\ 1 \end{bmatrix} \right) \\ \dot{\delta}_{CG_y} &= K_3 T\tilde{\omega}_c^T I_c^{-1} \begin{bmatrix} 0 \\ 1 \end{bmatrix} \end{cases} \quad (6.46)$$

Figures 6.12 through 6.12c show the comparison of the nominal control and the adaptive control (with parameter estimation), for a misalignment of 0.7 m along the y-axis.

In Figure 6.12a, without the adaptive law, it is not possible to track the computed reference, because an unknown torque is acting upon the system, which is not taken into account when computing the control signal. In Figure 6.12b, with adaptive control, the controller is now able to track the angular velocity reference. From Figure 6.13a, without adaptive control, there is a static error in the reference tracking of ψ , which vanishes when using adaptive control. Figure 6.13b shows the control signals for both controllers. The magnitude of the control signal using the adaptive controller is of the same order as that of the nominal controller. Nevertheless, the improvements in terms of reference tracking performance and stability are considerable.

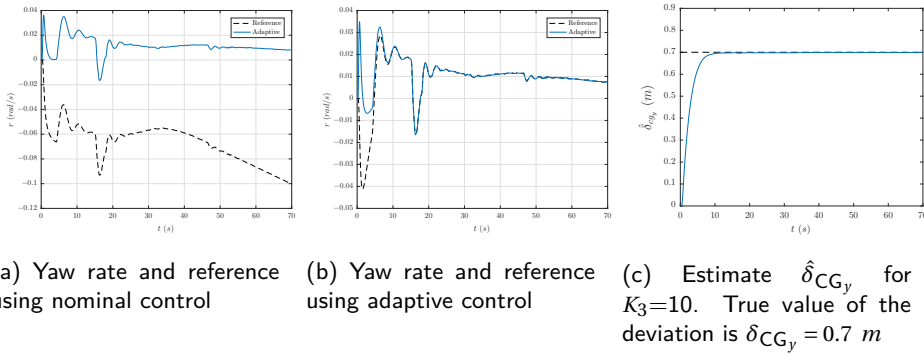


Figure 6.12: Comparison of nominal and adaptive control for $\delta_{CG_y} = +0.7 \text{ m}$

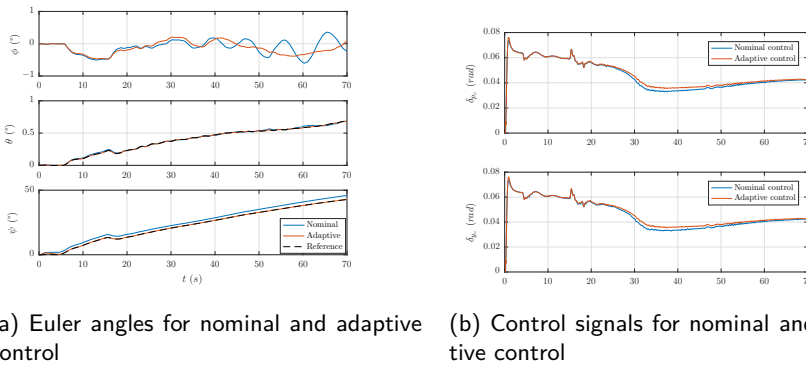


Figure 6.13: Euler angles and control signal for $\delta_{CG_y} = +0.7 \text{ m}$

Figure 6.12c shows the evolution of the estimate $\hat{\delta}_{CG_y}$ with $K_3 = 10$. Approximately after 10 s of simulation, the estimate converges to the real value of the deviation and the TVC system is able to counteract the extra moment induced by this model mismatch.

7

COMPARISON OF THE LINEAR AND NONLINEAR CONTROLLERS

It is one of the goals of this work to compare performance, advantages and drawbacks of using linear or nonlinear methods to control the atmospheric ascent of launch vehicles. In Section 4.3.2 it was seen that the LQR controller was much more robust than the PID controllers and thus it was considered the baseline linear controller. The same holds here and only the performance of the LQR controller will be analysed, in addition to the nonlinear controller.

By using nonlinear techniques, two controllers were developed, a nominal (fixed) backstepping controller and an adaptive backstepping controller with an adaptive control law to estimate the position of the center of mass. The benefits of the adaptive controller were provided in Section 6.8 and relate to the specific case of uncertainty in the center of mass along the y_B -axis. Henceforth, to get a more general overview of linear vs. nonlinear control techniques applied to launchers, the adaptive backstepping controller is omitted from this comparison, although the conclusions can be extended for that case.

The performance of the LQR and backstepping controller applied to the nonlinear model, for two different trajectories, both for nominal conditions and with flexible modes will be considered. In Chapter 6, several disturbances to the system were identified and their impact on the associated responses was studied. However, the effect of flexible modes is the most relevant for launch vehicles, so this will be the disturbance to the nominal system considered in the present evaluation. The two trajectories used in the simulations are the reference trajectory, defined in Section 2.1, and the trajectory designed to assess the flexible modes, introduced in Section 6.6. Results are presented in Tables 7.1 and 7.2, respectively for the nominal trajectory and flexible modes trajectory.

Considering first Table 7.1, it can be seen that the backstepping controller presents smaller reference tracking errors, but the control action RMS is slightly larger. The overall results with both controllers for this trajectory are similar. As seen before, the nominal trajectory is smooth and slowly varying and, as such, the flexible modes do not have a significant impact on the system. In these conditions, the LQR controller

achieves good performance and even though is it designed for the linearized model at $t = 10$ s, it is able to stabilize the nonlinear system also for the remaining operation points.

From Table 7.2, it is clear that the performance of the LQR controller is degraded with the inclusion of the flexible modes. With both flexible modes, this controller cannot stabilize the system, which is depicted by the exponential growth of the reference tracking error from nominal conditions to the inclusion of the flexible modes. On the other hand, the backstepping controller is able to stabilize the system with the flexible modes, having performance levels similar to the nominal case. Comparing the results of both trajectories, the performance of backstepping degrades with respect to the nominal trajectory, but the controller is able to track the reference for all cases (with and without flexible modes). The LQR controller, however, behaves very poorly in the second considered trajectory with the flexible modes, as it cannot stabilize the system. Therefore, the backstepping controller is more robust and yields better results compared to the LQR controller. Backstepping control is robust to changes in several parameters and uncertainties and can even be augmented with parameter estimation techniques in special circumstances. Figure 7.1 shows a simulation run with both flexible modes for both controllers (corresponding with the data from the last column of Table 7.2).

		Nominal	1 flex	2 flex
LQR	$\sum \hat{\theta}^2$	7.92E-5	7.92E-5	7.92E-5
	$\sum \hat{\psi}^2$	0.1569	0.1569	0.1569
Backstepping	$\sum \hat{\theta}^2$	1.90E-6	1.90E-6	1.90E-6
	$\sum \hat{\psi}^2$	8.26E-5	8.26E-5	8.26E-5
LQR	δ_{PRMS}	0.00088	0.00089	0.00089
	δ_{YRMS}	0.00093	0.00094	0.00094
Backstepping	δ_{PRMS}	0.00099	0.00099	0.00100
	δ_{YRMS}	0.00104	0.00104	0.00105

Table 7.1: Comparison of the LQR and backstepping controllers, for the nominal trajectory

		Nominal	1 flex	2 flex
LQR	$\sum \hat{\theta}^2$	0.2225	0.3743	21.1321
	$\sum \hat{\psi}^2$	6.8671	19.3424	561.6633
Backstepping	$\sum \hat{\theta}^2$	0.2133	0.2124	0.2121
	$\sum \hat{\psi}^2$	5.5623	5.0921	5.1652
LQR	δ_{PRMS}	0.0841	0.2188	1.3707
	δ_{YRMS}	0.0812	0.1887	0.9515
Backstepping	δ_{PRMS}	0.0261	0.0265	0.0279
	δ_{YRMS}	0.0242	0.0249	0.0265

Table 7.2: Comparison of the LQR and backstepping controllers, for the flexible modes trajectory

In Figures 7.1a and 7.1b it is clear that the performance of the backstepping controller is better than the LQR controller. Backstepping is able to follow the reference trajectory during the full simulation, while LQR controller cannot follow the trajectory after $t = 50$ s. When a sharp transition in the reference signal occurs (at $t = 10$ s and $t = 55$ s), the LQR control action is saturated (see Figure 7.1d) and performance is degraded. Furthermore, Figure 7.1c, shows that the LQR controller is not able to asymptotically track the sinusoidal reference in the presence of the flexible modes, as there is a delay in the response. However, the backstepping controller can track this sinusoidal reference without delay.

Given the results obtained with the LQR controller, one could think of designing a center of mass estimator, as developed for the backstepping controller. However, this is not straightforward due to several reasons. Firstly, this is a time-varying system and, as such, if using linear control, there are several controllers for each different part of the

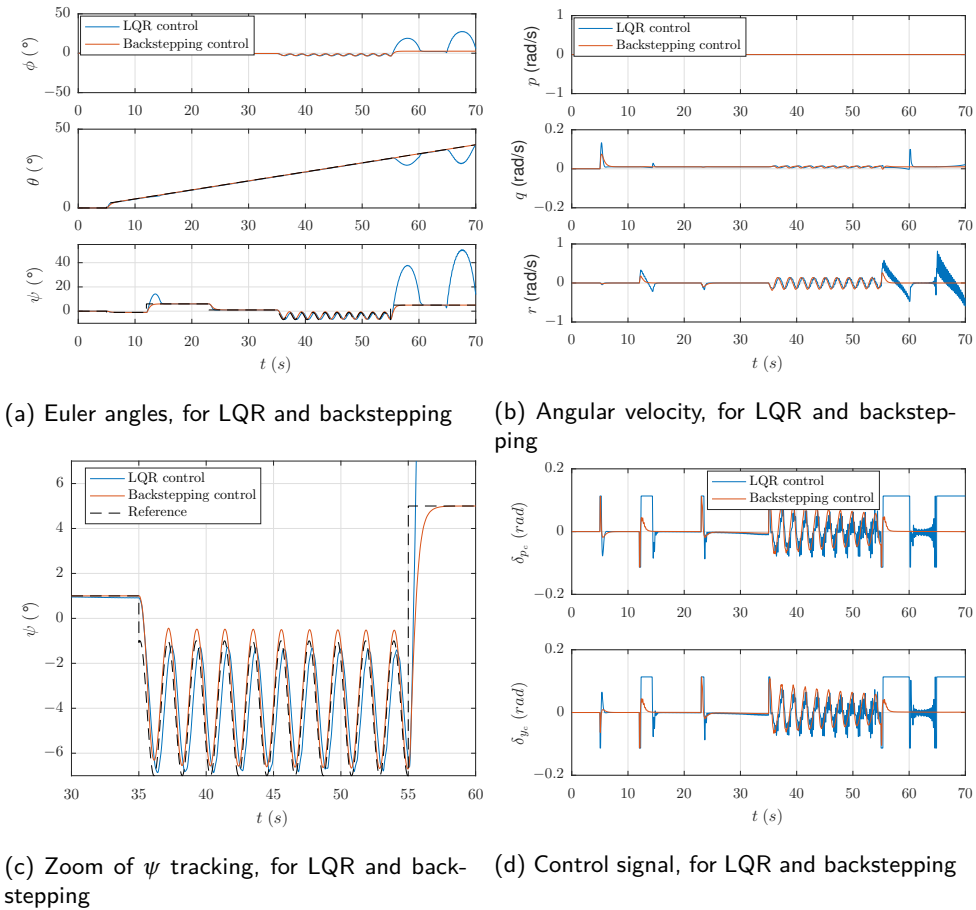


Figure 7.1: Nonlinear model simulations, with flexible modes, for LQR and backstepping control

trajectory, with the switching done by a gain-scheduling algorithm. Hence, it is necessary to design several estimators (for the different parts of the trajectory). Furthermore, guaranteeing overall stability for a gain-scheduled system is difficult, especially close to the transitions [58]. Designing a controller and an estimator and connecting them is not the same as designing the controller and estimator at once, which introduces more complexity in the linear case. Hence, it is difficult to guarantee proper stability margins for the connected system (even with LQG design the stability margins are poor). For backstepping control design this is not a problem, as the estimator dynamics are derived from the Lyapunov function and, therefore, are global (provided that global stability can be proven with the selected Lyapunov function).

The linear control techniques used heavily rely on the trim points (and therefore on the trajectory). If a controller is tuned for a particular trajectory, there is no guarantee that it will work properly for a different trajectory. For this reason, it is difficult to adapt the designed linear controllers to other launch systems. Linearization around trim

points also depends on system parameters, so if considering a different launch vehicle, the linearized systems for which the controllers are developed can be substantially different, even if the same trajectory is used.

It is easier to adapt the backstepping controller to another launch vehicle, as the evaluation is based on Lyapunov stability analysis, which will be the same independently of the system's parameters. What changes are the actual limits for the gains that ensure stability for the several considered perturbations, as these are dependent on the trajectory and system parameters. Nevertheless, analytical expressions for these limits were derived in the previous chapter and can be extended to other launch vehicles. A downside of using nonlinear techniques is that the mathematics involved in the stability analysis are complex and in some cases (for example in the effect of flexible modes) very difficult to obtain. Furthermore, the bounds for the gains established in Chapter 6 are very conservative, as the worst-case scenario was always considered in the analysis. Hence, the controllers obtained may not be optimal.

In terms of robustness to disturbances and adaptability to other systems, backstepping control is superior to LQR control, as illustrated in Figure 7.2. While in the backstepping design process robustness analysis needs to be performed once and can then be extended to other launchers, adapting the system parameters and the controller gains (see Figure 7.2a), for linear control design there are three decision points (see Figure 7.2b) that can involve iterations. Firstly, trim points depend not only on the launcher parameters, but also on the trajectory itself. Then, local stability of the designed LTI controller needs to be assessed for every trim point and lastly the global stability of the controller is evaluated, usually through exhaustive statistical testing like Monte Carlo simulations. It is important to note that in this work a single linear controller was designed for the whole trajectory, but in the industry the process involves designing multiple linear controllers for adjacent models [22] [23].

To summarize this discussion, Figure 7.3 shows a graphical comparison between the LQR and backstepping controllers, taking into account three key parameters:

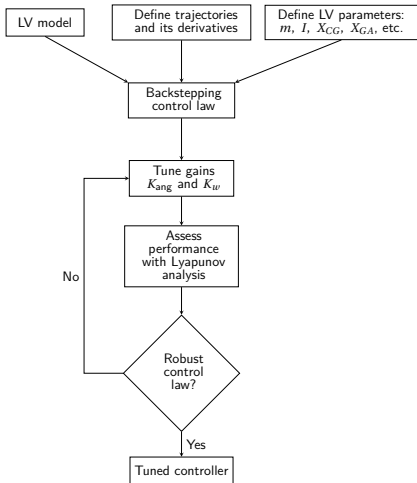
- Robustness - measures the controller's ability to reject exogenous disturbances, measurement noise & model uncertainty;
- Performance - measures the controller's ability to follow the desired trajectory;
- (Easiness of) Tuning - measures the effort to tune the controller and adaptability to other launchers.

In terms of tuning, the backstepping controller is superior, as it only involves setting two matrix gains K_{ang} and K_w , while for the LQR controller it is necessary to tune the control effort and performance weight filters, in addition to solving the Riccati equation to obtain the controller gains. Furthermore, the adaptability of the LQR to other launch systems is not straightforward.

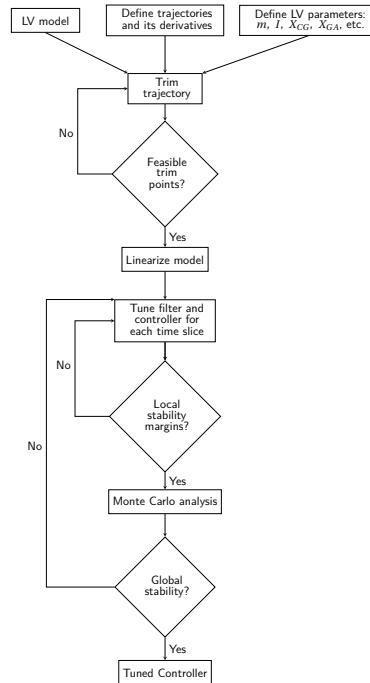
Regarding performance in the nominal condition, the LQR behaves similarly to the backstepping controller, albeit performance degrades for demanding trajectories.

As for robustness, it was seen that the backstepping controller is able to reject disturbances more satisfactorily, when compared to the LQR controller.

Nevertheless, like in all other optimization processes, there is a trade-off between adaptability to other systems and mathematical complexity of the proposed control solution.



(a) Nonlinear controller synthesis scheme



(b) LQR controller synthesis scheme

Figure 7.2: Comparison of the control synthesis schemes, for LQR and backstepping control

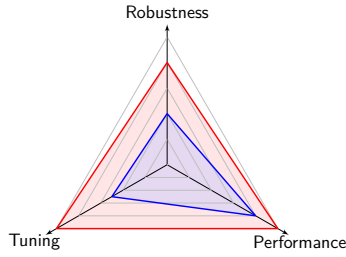
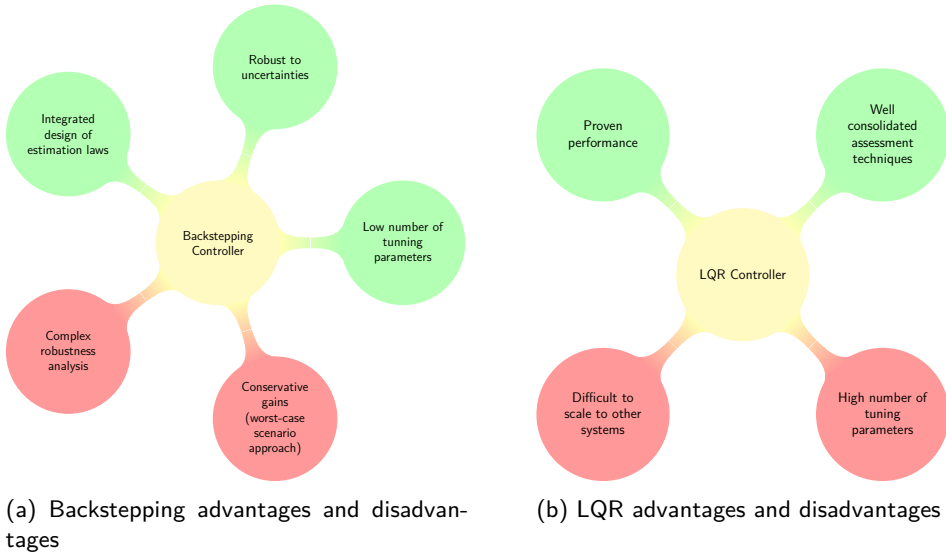


Figure 7.3: Comparison of the LQR controller (blue), with the backstepping controller (red)

Finally, Figure 7.4 provides a visual representation of the principle points discussed in this chapter, regarding the advantages and disadvantages of the considered control methods.



(a) Backstepping advantages and disadvantages

(b) LQR advantages and disadvantages

Figure 7.4: Comparison of the advantages and disadvantages of the selected control techniques

8

CONCLUSIONS AND FUTURE WORK

Motivated by recent trends in the satellite market, an investigation of control techniques to be employed in small launch vehicles was conducted. Control systems are essential in these systems as launch vehicles are inherently unstable. One of the key goals of this work is to develop advanced controller synthesis methods that can be applied to a large class of launchers, with limited control authority. This dissertation addressed linear and nonlinear control algorithms that can be used to control the trajectory of launch vehicles and its main contributions can be summarized as follows:

- A generic model of a small symmetric rocket launcher with limited roll motion was developed. This model provides a tool for flight control systems design and can be adapted to a wide range of rocket launchers, provided that their characteristics are known. The impact of flexible modes on the system were also modelled. This model was implemented with modular Simulink blocks, that allow setting multiple disturbances to the nominal system;
- Two linear controllers were designed. Both stabilize the linearized and the full nonlinear systems, but LQR control proves to have a superior performance when compared to the PID controller;
- The robustness of the LQR controller to parameter uncertainty was assessed, as well as the effects of the flexible modes in the linear system;
- A nonlinear backstepping controller was synthesised and its robustness to the inclusion of flexible modes and parameter variation was evaluated using Lyapunov analysis;
- Through robustness analysis of the nonlinear controller, bounds were derived for the parameters of the nonlinear controller. These parameters are the tuning knobs of the controller.
- In the sequence of the robustness analysis of the nonlinear controller, an adaptive backstepping controller with parameter estimation for the position of the center

of mass was developed and tested in simulation, proving the applicability of such techniques in controller synthesis;

- A comparison between the effort of developing linear and nonlinear controllers was provided and the possibility of adapting these designs to other launch vehicles discussed.

Choosing a nonlinear control technique over linear control or vice-versa is not a trivial choice and several parameters influence this decision. Regarding adaptability to other launchers, nonlinear control has clear advantages, since there are less variables to tune than for linear control. In addition, Lyapunov analyses can be easily extended if the parameters of the system change. Major changes on the system's parameters imply that the linearized models for which the linear controllers are developed are no longer valid. On the other hand, linear control design is simpler, as Lyapunov analysis can be hindered by the selection of the appropriate functions.

There is a lot of effort involved in the design of a nonlinear controller, but this process is done once for a wide class of launchers. As such, there is an extensive work to be done but the effort is minimal if the parameters change. Furthermore, analytical stability guarantees can be derived. For linear control, the V & V campaign involves multiple simulations and the process needs to be repeated for every change in the project.

Nonetheless, all proposed objectives were achieved and the work developed provides insights on the control of launch vehicles as well as the trade-off between using linear or nonlinear control for such purpose.

8.1. DIRECTIONS FOR FUTURE WORK

Several issues related with modelling, linear control, and nonlinear control can be further analysed. The model presented in Chapter 2 can still be refined to include a plethora of nonlinear phenomena that affect launch vehicles. The most important are fuel sloshing and aerodynamic flutter. Furthermore, a more accurate model of the aerodynamic coefficients can be developed, though this is difficult because the aerodynamic description of launch vehicles is usually classified.

Regarding linear control, a gain scheduling algorithm could be adopted and multiple linear controllers for the different parts of the atmospheric trajectory may be developed.

With respect to nonlinear control, it is important to have a reliable model, as a large class of nonlinearities can be incorporated in the control design. A major improvement would be the introduction of the structural flexible modes in the backstepping design. In addition, further work can be done in the robustness analysis of the backstepping controller can be performed especially with regard to of measurement errors and uncertainty in the inertia matrix in the derivative of the Lyapunov function. Furthermore, the inclusion of actuator bounds in control design can also be considered when designing the nonlinear controller. This is expected to yield upper limits to the acceptable nonlinear controller gains, ultimately allowing the definition of a closed set of gain for which the stability of the system is guaranteed.

In this work, continuous-time models were considered, but in reality control systems for launch vehicles are implemented as discrete-time algorithms, which have a series of associated issues. Both linear and nonlinear control techniques can be extended to discrete-time.

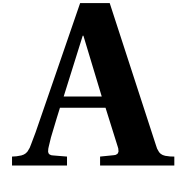
REFERENCES

- [1] Serdata, "World launcher review 2015-16," tech. rep., Commercial Space Technologies Limited, Serdata Limited, 2015.
- [2] Federal Aviation Administration, "2015 Commercial Space Transportation Forecasts," Tech. Rep. April, FAA Commercial Space Transportation (AST), 2015.
- [3] D. Dumitriu, S. Marques, P. U. Lima, and B. Udrea, "Decentralized, low-communication state estimation and optimal guidance of formation flying spacecraft," in *16th AAS/AIAA Space Flight Mechanics Meetings*, 2006.
- [4] A. Lele and T. Shrivastav, "Rocket Launchers for Small Satellites," tech. rep., Institute for Defence Studies and Analyses, 2016.
- [5] R. Sandau, "Status and trends of small satellite missions for Earth observation," *Acta Astronautica*, vol. 66, no. 1-2, pp. 1–12, 2010.
- [6] D. Dumitriu, P. U. Lima, and B. Udrea, "Optimal trajectory planning of formation flying spacecraft," *IFAC Proceedings Volumes*, vol. 38, no. 1, pp. 313–318, 2005.
- [7] K. Woellert, P. Ehrenfreund, A. J. Ricco, and H. Hertzfeld, "Cubesats: Cost-effective science and technology platforms for emerging and developing nations," *Advances in Space Research*, vol. 47, pp. 663–684, 2011.
- [8] A. K. Nervold, J. Berk, J. Straub, and D. Whalen, "A Pathway to Small Satellite Market Growth," no. June, pp. 14–20, 2016.
- [9] R. Barbera and S. Bianchi, "Vega: The European small-launcher programme," *ESA bulletin*, no. february 2002, pp. 64–70, 2002.
- [10] P. Fortescue, G. Swinerd, and J. Stark, *Spacecraft Systems Engineering*. Wiley, 2011.
- [11] P. K. McConnaughey, M. G. Femminineo, S. J. Koelfgen, R. a. Lepsch, R. M. Ryan, and S. a. Taylor, "Launch Propulsion Systems Technology Roadmap," 2010.
- [12] M. Sweeting, "Why satellites are scaling down," *Space Technology International*, pp. 55–59, 1991.
- [13] C. R. Roux and I. Cruciani, "Scheduling Schemes And Control Law Robustness In Atmospheric Flight of the Vega Launcher," *Proceedings of the 7th ESA GNC Conference*, 2009.
- [14] J. Hanson, M. Shrader, and C. Cruzen, "Ascent guidance comparisons," *The Journal of the Astronautical Sciences*, vol. 43, pp. 307–326, 1995.

- [15] W. Schleich, "The space shuttle ascent guidance and control," in *Guidance and Control Conference*, p. 1497, 1982.
- [16] J. S. Orr, J. H. Wall, and C. E. Hall, "Space Launch System Ascent Flight Control Design," in *2014 American Astronautical Society (AAS) Guidance, Navigation, and Control Conference*, 2014.
- [17] C. Bahm, E. Baumann, J. Martin, D. Bose, R. Beck, and B. Strovers, "The x-43a hyper-x mach 7 flight 2 guidance, navigation, and control overview and flight test results," in *AIAA/CIRA 13th International space planes and hypersonics systems and technologies conference*, p. 3275, 2005.
- [18] P. Lu, H. Sun, and B. Tsai, "Closed-loop endoatmospheric ascent guidance," *Journal of Guidance, Control, and Dynamics*, vol. 26, no. 2, pp. 283–294, 2003.
- [19] B. Wie, W. Du, M. Whorton, N. Marshall, and S. Flight, "Analysis and Design of Launch Vehicle Flight Control Systems," no. 515, pp. 1–11, 2008.
- [20] J.-w. Jang, A. Alaniz, R. Hall, N. Bedrossian, C. Hall, and M. Jackson, "Design of Launch Vehicle Flight Control Systems Using Ascent Vehicle Stability Analysis Tool," in *AIAA Guidance, Navigation, and Control Conference*, pp. 1–16, 2011.
- [21] W. Du, "*Dynamic modeling and ascent flight control of Ares-I Crew Launch Vehicle*". PhD thesis, Iowa State University, 2010.
- [22] M. Rotunno, T. Fiorenzani, P. Petritoli, and S. Bennani, "Modern analysis techniques for gain scheduled thrust vector controllers of launchers," in *Computer Aided Control System Design, 2006 IEEE International Conference on Control Applications, 2006 IEEE International Symposium on Intelligent Control, 2006 IEEE*, pp. 2896–2901, IEEE, 2006.
- [23] A. Marcos, C. Roux, M. Rotunno, H.-D. Joos, S. Bennani, L. F. Penin, and A. Caramagno, "The v&v problematic for launchers: current practice and potential advantages on the application of modern analysis techniques," in *ESA Guidance, Navigation and Control Conference, Karlovy Vary, Czech Republic*, 2011.
- [24] C. Roux, V. Mantini, A. Marcos, L. F. Peñín, and S. Bennani, "Robust flight control system design verification & validation for launchers," *AIAA Guidance, Navigation, and Control Conference 2012*, pp. 1–9, 2012.
- [25] A. Marcos, P. Rosa, C. Roux, M. Bartolini, and S. Bennani, "An overview of the RFCS project V&V framework: optimization-based and linear tools for worst-case search," *CEAS Space Journal*, vol. 7, no. 2, pp. 303–318, 2015.
- [26] A. Marcos, V. Mantini, C. Roux, S. Bennani, and M. Carlo, "Bridging the gap between linear and nonlinear worst-case analysis : an application case to the atmospheric phase of the VEGA launcher," *19th IFAC Symposium on Automatic Control in Aerospace*, 2013.

- [27] S. Ding and W. X. Zheng, "Nonsmooth attitude stabilization of a flexible spacecraft," *IEEE Transactions on Aerospace and Electronic Systems*, vol. 50, no. 2, pp. 1163–1181, 2014.
- [28] B. Costic, D. Dawson, M. De Queiroz, and V. Kapila, "Quaternion-based adaptive attitude tracking controller without velocity measurements," *Journal of Guidance, Control, and Dynamics*, vol. 24, no. 6, pp. 1214–1222, 2001.
- [29] S. Di Gennaro, "Output feedback stabilization of flexible spacecraft," in *Decision and Control, 1996., Proceedings of the 35th IEEE Conference on*, vol. 1, pp. 497–502, IEEE, 1996.
- [30] E. N. Johnson and A. J. Calise, "Limited Authority Adaptive Flight Control for Reusable Launch Vehicles," *Journal of Guidance, Control, and Dynamics*, vol. 26, no. 6, 2003.
- [31] A. Ngo and D. Doman, "Dynamic inversion-based adaptive/reconfigurable control of the X-33 on ascent," *Journal of Guidance, Control, and Dynamics*, vol. 25, no. 2, pp. 275–284, 2002.
- [32] Arianespace, *Vega User's Manual*. 2014.
- [33] C. R. Roux and I. Cruciani, "Roll coupling effects on the stability margins for vega launcher," *AIAA Structures, Structural Dynamics, and Materials Conference*, pp. 1–18, 2007.
- [34] "Vega Launch System," 2011.
- [35] "Vega launcher characteristics," tech. rep., TU Delft.
- [36] A. Marcon, L. Mangiacasale, and P. D. Resta, "Simulation model for VEGA control system design," *European Space Agency, (Special Publication)*, no. 606, pp. 137–142, 2006.
- [37] G. Baldesi and M. Toso, "ESA Launcher Flight Dynamics Simulator Used for System and Subsystem Level Analyses," *Advances in Aerospace Guidance, Navigation and Control: Selected Papers*, no. 1, pp. 434–437, 2011.
- [38] F. Amato, E. Filippone, R. Iervolino, C. Italiano, and R. Aerospaziali, "Modelling and Guidance of a Small Conventional Launcher: The translational motion,"
- [39] N. Zosimovych, "Selecting Design Objectives for an Integrated Guidance System of a Commercial Launch Vehicle with Application of GPS Technologies," *The Open Aerospace Engineering Journal*, pp. 6–19, 2013.
- [40] R. Lafranconi and M. Lopez, "VEGA: the European Small Launcher," 2007.
- [41] J. Mulder, W. van Staveren, J. van der Vaart, and E. Al, "*Flight Dynamics*". 2013.
- [42] J. Diebel, "Representing attitude: Euler angles, unit quaternions, and rotation vectors," tech. rep., Stanford University, 2006.

- [43] R. M. Murray, L. Zexiang, and S. S. Sastry, "A *Mathematical Introduction to Robotic Manipulation*". 1994.
- [44] M. S. Whorton, C. E. Hall, and S. A. Cook, "Ascent Flight Control and Structural Interaction for the Ares-I Crew Launch Vehicle," *AIAA Structures, Structural Dynamics, and Materials Conference*, pp. 1–13, 2007.
- [45] E. Mooij, "The motion of a vehicle in a planetary atmosphere," 1994.
- [46] B. Wie, "*Space vehicle dynamics and control*". American Institute of Aeronautics and Astronautics, 1998.
- [47] B. N. Pamadi, P. V. Tartabini, B. R. Starr, V. A. Branch, A. S. Concepts, and A. Competency, "Ascent , stage separation and glideback performance of a partially reusable small launch vehicle," pp. 1–16.
- [48] Mathworks, "Mathworks - trimming and linearization." Available at <http://www.mathworks.com/help/simulink/slref/trim.html> (28/06/2015).
- [49] E. T. Falangas, *Performance Evaluation and Design of Flight Vehicle Control Systems*. John Wiley & Sons, 2015.
- [50] K. Ogata, "*Modern Control Engineering*". 2012.
- [51] G. Olsder, J. van der Woude, J. G. Maks, and D. Jeltsema, "*Mathematical Systems Theory*". Delft: VSSD, 4th ed., 2011.
- [52] S. Skogestad and I. Postlethwaite, "*Multivariable feedback control: analysis and design*". 2001.
- [53] S. Bennani, A. Marcos, X. Lefort, and P. Simplício, "Structured Singular Value Analysis of the VEGA Launcher in Atmospheric Flight," *Journal of Guidance, Control, and Dynamics*, vol. 39, no. 6, pp. 1342–1355, 2016.
- [54] T. Pulecchi, A. Marcos, C. Roux, V. Mantini, and S. Bennani, "Thrust Vector Control Robustness of axial-symmetric Launch Vehicles with Fuel Slosh," *AIAA Guidance, Navigation, and Control Conference*, pp. 1–10, 2012.
- [55] H. K. H. Khalil, *Nonlinear Systems*. 1996.
- [56] N. Paulino, G. Cuciniello, I. Cruciani, F. Corrado, D. Spallotta, and F. Nebula, "Vega Roll And Attitude Control System Algorithms Trade-off study," *Progress in Flight Dynamics, GNC, and Avionics*, vol. 6, pp. 209–228, 2013.
- [57] W. J. Rugh, *Linear System Theory (2Nd Ed.)*. Upper Saddle River, NJ, USA: Prentice-Hall, Inc., 1996.
- [58] W. J. Rugh and J. S. Shamma, "Research on gain scheduling," *Automatica*, vol. 36, no. 10, pp. 1401–1425, 2000.



VEGA LAUNCHER CHARACTERISTICS

Overall Vehicle [32]:

- Overall length: 30.2 m
- Maximum diameter: 3 m
- Lift-off mass: 137820 kg

Stage	1	2	3	4
Designation	P80	Zefiro 23	Zefiro 9	AVUM
Length (m)	11.2	8.39	4.12	2.04
Diameter (m)	3	1.9	1.9	2.18
Gross mass (kg)	96243	26300	12000	688
Propellant				
Type	P80FW SRM	Z23FW SRM	Z9FW SRM	4 titanium propellant tanks
Fuel	HTPB 1912 Solid	HTPB 1912 Solid	HTPB 1912 Solid	MEA Liquid
Mass	87 710	23814	10567	4180
Burn time (s)	109.9	77.1	295.9	up to 612.5
Thrust (kN)				
Sea Level	2621	-	-	-
Vacuum	3015	1120	317	2.45
Restart Capability (No times)	N/A	N/A	N/A	5
Attitude Control				
Pitch and Yaw	TVC Electro-actuator nozzle gimbaling	TVC Electro-actuator nozzle gimbaling	TVC Electro-actuator nozzle gimbaling	TVC Electro-actuator nozzle gimbaling
Roll	Roll rate limited by 4 of the 6 RACS thrusters	Roll rate limited by 4 of the 6 RACS thrusters	Roll rate and attitude controlled by 4 of the 6 RACS thrusters	6 RACS thrusters
TVC Max deflection:	±6.5°	±7°	±6°	±10°

Table A.1: Summary of VEGA's main characteristics

B

ROTATION MATRICES

B.1. FROM ECI TO LAUNCH POINT REFERENCE FRAME

To go from the ECI reference frame to the Launch point reference frame, three rotations need to be performed. The sequence of rotations is:

1. Rotate τ around the Z_{ECI} -axis (longitude);
2. Rotate δ around the intermediate Y -axis (latitude);
3. Rotate 90° around the X_L -axis, to bring the Y_L and Z_L into its desired position;

The final rotation around the X_L -axis only serves the purpose of placing the Z_L -axis pointing westward and the Y_L -axis pointing towards the North.

The longitude (τ) is positive if the vehicle is east of the Greenwich meridian and negative when west. Latitude is positive on the northern hemisphere. The ranges for both angles are, respectively [41] :

$$-\pi \leq \tau < \pi, \quad -\frac{\pi}{2} \leq \delta < \frac{\pi}{2}$$

The corresponding rotation matrix is given by the product

$${}^I_L \mathbf{R} = \begin{bmatrix} 1 & 0 & 0 \\ 0 & 0 & 1 \\ 0 & -1 & 0 \end{bmatrix} \cdot \begin{bmatrix} c\delta & 0 & s\delta \\ 0 & 1 & 0 \\ -s\delta & 0 & c\delta \end{bmatrix} \cdot \begin{bmatrix} c\tau & s\tau & 0 \\ -s\tau & c\tau & 0 \\ 0 & 0 & 1 \end{bmatrix} = \begin{bmatrix} c\delta c\tau & c\delta s\tau & s\delta \\ -s\delta c\tau & -s\delta s\tau & c\delta \\ s\tau & c\tau & 0 \end{bmatrix} \quad (\text{B.1})$$

C

IMPLEMENTATION OF THE MODEL

Having obtained the nonlinear equations of motion expressed in Eq. (2.25), and the contribution of the flexible modes in Eq. (2.27), two nonlinear models were implemented in Matlab: one as an s-function and another using Simulink blocks. In the Simulink-based version, the data is organized into simulation buses that contain states and other important variables for simulation. Both models allow for the simulation of a rigid body model and a model with flexible modes. The flexible modes can be activated or deactivated by a simulation flag. Joining all the information from the previous sections, the state equations are:

$$f(\mathbf{x}, \mathbf{u}, t) = \begin{cases} {}^B \dot{\mathbf{v}}_B = \frac{1}{m} \cdot \Sigma \mathbf{F}_{\text{ext}} - \mathbf{S} ({}^B \boldsymbol{\omega}_B)^B \mathbf{v}_B \\ {}^B \dot{\boldsymbol{\omega}}_B = \mathbf{I}^{-1} (\Sigma \mathbf{M}_{\text{ext}} - {}^B \boldsymbol{\omega}_B \times \mathbf{I} \cdot {}^B \boldsymbol{\omega}_B) \\ \dot{\boldsymbol{\lambda}}_B = f_0(\boldsymbol{\lambda}) \cdot {}^B \boldsymbol{\omega}_B \\ \dot{m} = -900 \text{ kg/s} \\ \ddot{q}_i = -\omega_i^2 q_i - 2\xi \omega_i \dot{q}_i - T_y t_{pi}, \quad i = 1, 2 \\ {}^L \dot{\mathbf{p}}_B = {}^L \mathbf{R}^B \mathbf{v}_B \end{cases} \quad (\text{C.1})$$

Schematically, the simulation model can be represented as in Figure C.1. The mathematical modelling and the Simulink implementation of the nonlinear model described in this chapter, serve as a starting point for the controller design approaches provided throughout the dissertation.

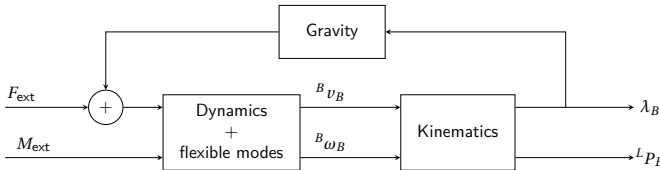


Figure C.1: Diagram of the simulation

The Simulink model that implements the model described in Eq. (C.1) is shown in Figure C.2. The main point in this simulation structure is its modularity: the forces and moments are generated in separate blocks and then integrated in the block '6 DoF EoM Integration'. Environment variables, localization, propulsion, and mass models are all implemented separately, making it extremely simple to update and run simulations for several different vehicles. The data is organized into seven buses, that are logged to the workspace and defined as follows:

C

$$\begin{array}{l}
 \text{EoMBus } [12 \times 1] \left\{ \begin{array}{l} \text{dynamicsBus } [9 \times 1] \\ \text{kinematicsBus } [3 \times 1] \end{array} \right. \left\{ \begin{array}{l} v_b [3 \times 1] \\ \omega_b [3 \times 1] \\ V [1 \times 1] \rightarrow \text{airspeed} \\ \alpha_A [1 \times 1] \\ \beta_A [1 \times 1] \\ \phi [1 \times 1] \\ \theta [1 \times 1] \\ \psi [1 \times 1] \end{array} \right. \left\{ \begin{array}{l} \text{atmosBus } [4 \times 1] \\ \text{ControlBus } [4 \times 1] \\ \text{TransfBus} [6 \times 3] \\ \text{AeroBus} [12 \times 1] \end{array} \right. \left\{ \begin{array}{l} \text{gravityBus } [3 \times 1] \{ g_b [3 \times 1] \\ \text{Temperature } [1 \times 1] \\ \text{SpeedOfSound } [1 \times 1] \\ \text{Pressure } [1 \times 1] \\ \text{Air density } [1 \times 1] \\ \delta_p [1 \times 1] \\ \delta_y [1 \times 1] \\ \text{Thrust } [3 \times 1] \\ \text{B2A} [3 \times 3] \\ \text{L2B} [3 \times 3] \\ {}^A F_A [3 \times 1] \\ {}^A M_{CoG_A} [3 \times 1] \\ {}^B F_A [3 \times 1] \\ {}^B M_{CoG_A} [3 \times 1] \\ \text{Thrust } [3 \times 1] \\ {}^B F_T [3 \times 1] \\ {}^B M_{CoG_T} [3 \times 1] \\ \text{propellantMass } [1 \times 1] \\ \text{consumedMass } [1 \times 1] \end{array} \right. \\
 \\
 \text{MCIBus } [19 \times 1] \left\{ \begin{array}{l} \text{Mass} [1 \times 1] \\ \text{CoGs} [3 \times 1] \\ I [3 \times 3] \\ l_{GA} [3 \times 1] \\ l_{CG} [3 \times 1] \end{array} \right. \\
 \\
 \text{airdataBus } [2 \times 1] \left\{ \begin{array}{l} q_{dyn} [1 \times 1] \\ \text{Mach } [1 \times 1] \end{array} \right. \\
 \\
 \text{flexBus } [6 \times 1] \left\{ \begin{array}{l} {}^B M_{flex} [3 \times 1] \\ {}^B F_{flex} [3 \times 1] \end{array} \right. \\
 \\
 \text{locBus } [6 \times 1] \left\{ \begin{array}{l} {}^L P_B [3 \times 1] \\ ECI P_B [3 \times 1] \end{array} \right.
 \end{array}$$

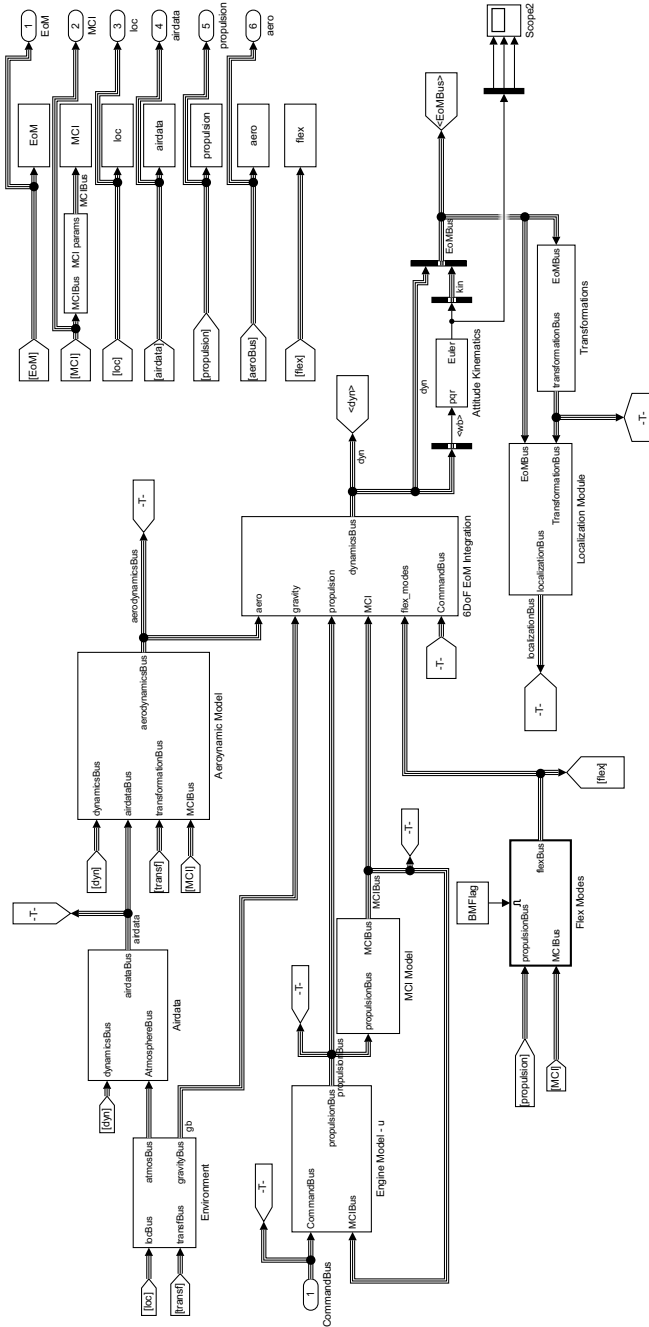
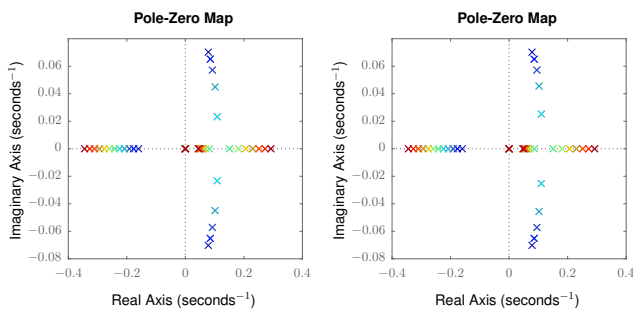


Figure C.2: Simulink diagram of the nonlinear model

D

EVOLUTION OF THE LINEARIZED SYSTEM'S POLES WITH TIME

D.1. FROM $T=10$ S TO $T=20$ S

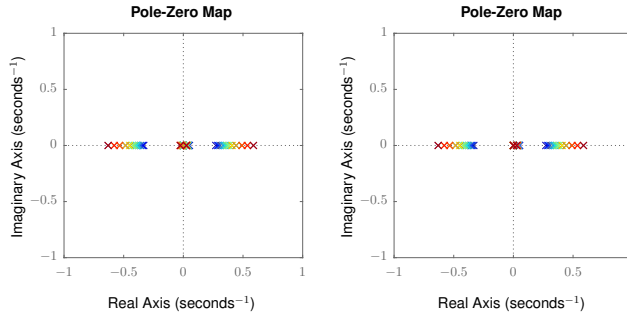


(a) Longitudinal poles

(b) Lateral poles

Figure D.1: Poles of the linearized longitudinal and lateral systems for $t= 10$ s to $t= 20$ s

D.2. FROM $T=20$ S TO $T=30$ S



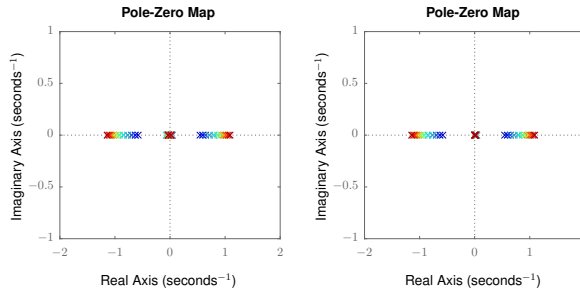
(a) Longitudinal poles

(b) Lateral

Figure D.2: Poles of the linearized longitudinal and lateral systems for $t = 20$ s to $t = 30$ s

D

D.3. FROM T=30 S TO T=40 S

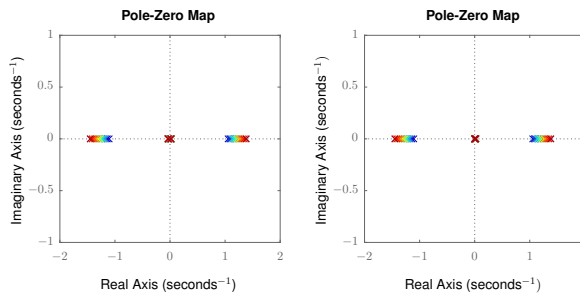


(a) Longitudinal poles

(b) Lateral poles

Figure D.3: Poles of the linearized longitudinal and lateral systems for $t = 30$ s to $t = 40$ s

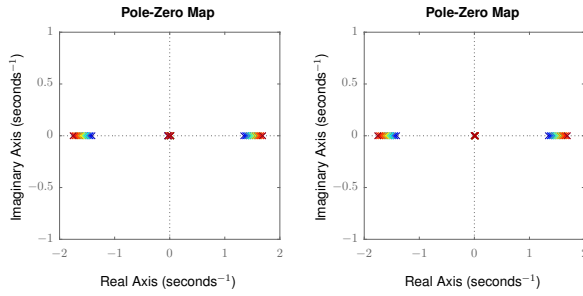
D.4. FROM T=40 S TO T=50 S



(a) Longitudinal poles

(b) Lateral poles

Figure D.4: Poles of the linearized longitudinal and lateral systems for $t = 40$ s to $t = 50$ s

D.5. FROM T=50 S TO T=60 S

(a) Longitudinal poles

(b) Lateral poles

Figure D.5: Poles of the linearized longitudinal and lateral systems for $t=50$ s to $t=60$ s

E

EFFECT OF VARYING PARAMETERS IN LQR CONTROLLER ROBUSTNESS

E.1. MASS

	$0.8m_0$	$0.9m_0$	$0.95m_0$	m_0	$1.05m_0$	$1.1m_0$	$1.2m_0$
Rise Time	0.36	0.36	0.36	0.36	0.36	0.36	0.36
Settling Time	0.62	0.62	0.62	0.62	0.62	0.62	0.62
Overshoot	0.22	0.22	0.22	0.22	0.22	0.22	0.22
$\delta_{p_{RMS}}$	0.66	0.66	0.66	0.66	0.66	0.66	0.66
$(\theta_{ref} - \theta)_{RMS}$	0.20	0.20	0.20	0.20	0.20	0.20	0.20

Table E.1: Summary of the effect of varying m in the system's response to a step in θ

E.2. I_{xx}

	$0.8I_{xx}$	$0.9I_{xx}$	$0.95I_{xx}$	I_{xx}	$1.05I_{xx}$	$1.1I_{xx}$	$1.2I_{xx}$
Rise Time	0.36	0.36	0.36	0.36	0.36	0.36	0.36
Settling Time	0.62	0.62	0.62	0.62	0.62	0.62	0.62
Overshoot	0.22	0.22	0.22	0.22	0.22	0.22	0.22
$\delta_{p_{RMS}}$	0.66	0.66	0.66	0.66	0.66	0.66	0.66
$(\theta_{ref} - \theta)_{RMS}$	0.20	0.20	0.20	0.20	0.20	0.20	0.20

Table E.2: Summary of the effect of varying I_{xx} in the system's response to a step in θ

E.3. x_{CG}

	$0.8x_{CG}$	$0.9x_{CG}$	$0.95x_{CG}$	$0.8x_{CG}$	$1.05x_{CG}$	$1.1x_{CG}$	$1.2x_{CG}$
Rise Time	0.35	0.35	0.35	0.36	0.36	0.37	0.39
Settling Time	0.95	0.57	0.59	0.62	0.65	0.68	0.73
Overshoot	3.43	1.36	0.67	0.22	0.03	0.00	0.00
$\delta_{p_{RMS}}$	0.73	0.69	0.67	0.66	0.64	0.63	0.61
$(\theta_{ref} - \theta)_{RMS}$	0.20	0.20	0.20	0.20	0.20	0.19	0.19

Table E.3: Summary of the effect of varying x_{CG} in the system's response to a step in θ

E.4. x_{CP}

	$0.8x_{CP}$	$0.9x_{CP}$	$0.95x_{CP}$	x_{CP}	$1.05x_{CP}$	$1.1x_{CP}$	$1.2x_{CP}$
Rise Time	0.36	0.36	0.36	0.36	0.36	0.36	0.36
Settling Time	0.62	0.62	0.62	0.62	0.62	0.62	0.62
Overshoot	0.22	0.22	0.22	0.22	0.22	0.22	0.22
$\delta_{p_{RMS}}$	0.66	0.66	0.66	0.66	0.66	0.66	0.66
$(\theta_{ref} - \theta)_{RMS}$	0.20	0.20	0.20	0.20	0.20	0.20	0.20

Table E.4: Summary of the effect of varying x_{CP} in the system's response to a step in θ

E.5. C_a

	$0.8C_a$	$0.9C_a$	$0.95C_a$	C_a	$1.05C_a$	$1.1C_a$	$1.2C_a$
Rise Time	0.36	0.36	0.36	0.36	0.36	0.36	0.36
Settling Time	0.62	0.62	0.62	0.62	0.62	0.62	0.62
Overshoot	0.22	0.22	0.22	0.22	0.22	0.22	0.22
$\delta_{p_{RMS}}$	0.66	0.66	0.66	0.66	0.66	0.66	0.66
$(\theta_{ref} - \theta)_{RMS}$	0.20	0.20	0.20	0.20	0.20	0.20	0.20

Table E.5: Summary of the effect of varying C_a in the system's response to a step in θ

E.6. C_n

	$0.8C_n$	$0.9C_n$	$0.95C_n$	C_n	$1.05C_n$	$1.1C_n$	$1.2C_n$
Rise Time	0.36	0.36	0.36	0.36	0.36	0.36	0.36
Settling Time	0.62	0.62	0.62	0.62	0.62	0.62	0.62
Overshoot	0.22	0.22	0.22	0.22	0.22	0.22	0.22
$\delta_{p_{RMS}}$	0.66	0.66	0.66	0.66	0.66	0.66	0.66
$(\theta_{ref} - \theta)_{RMS}$	0.20	0.20	0.20	0.20	0.20	0.20	0.20

Table E.6: Summary of the effect of varying C_n in the system's response to a step in θ

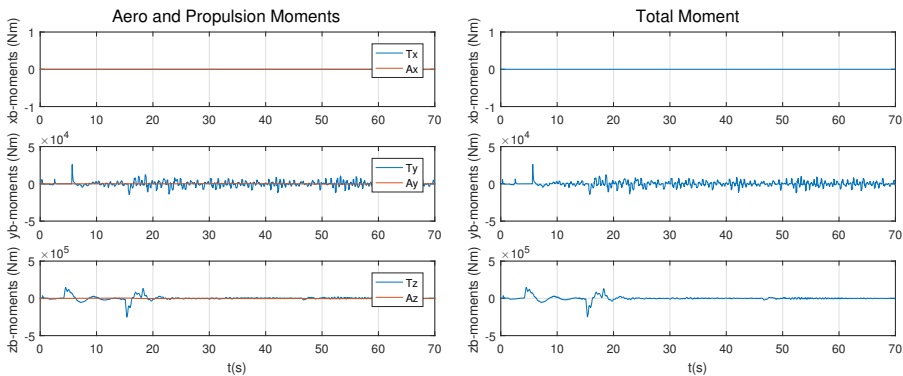
E.7. S

	$0.8S$	$0.9S$	$0.95S$	S	$1.05S$	$1.1S$	$1.2S$
Rise Time	0.36	0.36	0.36	0.36	0.36	0.36	0.36
Settling Time	0.62	0.62	0.62	0.62	0.62	0.62	0.62
Overshoot	0.22	0.22	0.22	0.22	0.22	0.22	0.22
$\delta_{p_{RMS}}$	0.66	0.66	0.66	0.66	0.66	0.66	0.66
$(\theta_{ref} - \theta)_{RMS}$	0.20	0.20	0.20	0.20	0.20	0.20	0.20

Table E.7: Summary of the effect of varying S in the system's response to a step in θ

F

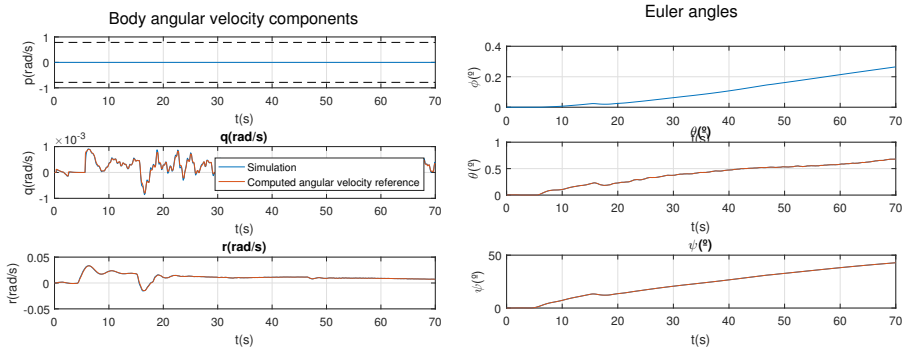
MOMENTS ACTING ON THE BODY FOR A PERTURBATION OF P_{CG} ALONG THE x_B -AXIS



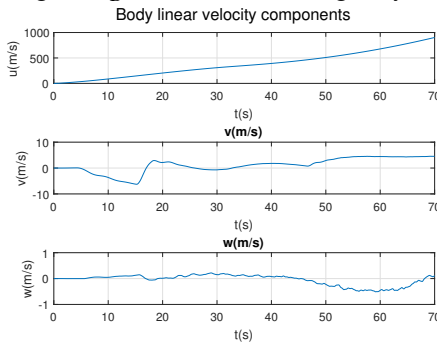
(a) Aerodynamic and propulsion moments, for a perturbation in the center of gravity along the x_B -axis

(b) Total moments, for a perturbation in the center of gravity along the x_B -axis

Figure F.1: Moments along the body axis for a perturbation of $5m$ in the position of the center of gravity along the x_B -axis



(a) Angular velocity, for a perturbation in the center of gravity along the x_B -axis (b) Euler angles, for a perturbation in the center of gravity along the x_B -axis



(c) Linear velocity, for a perturbation in the center of gravity along the x_B -axis

Figure F.2: Selected system variables for a perturbation of $+5m$ in the position of the center of gravity along the x_B -axis